

Development of Aqueous Ion-intercalation Battery Systems for High Power and Bulk Energy Storage

Thesis by
Julian DV Key



A thesis submitted in partial fulfilment of the requirements
for the degree of Doctor of Philosophy, in the Department of Chemistry,
University of the Western Cape.

Supervisor: Dr. Ji Shan

November 2013

Key words

Alkali metal ion

Activated carbon

Aqueous Li-ion batteries

Grid energy storage

Hybrid electric vehicle

Ion-intercalation

LiMn_2O_4

Low cost

PbSO_4

Supercapacitor



Acknowledgements

Dr Ji Shan
(SAIAMC/HySA Systems, UWC)

Prof. Vladimir M Linkov
(SAIAMC, UWC)

Prof. Yong-yao Xia
(Fudan University, Shanghai)

Prof. Yong-gang Wang
(Fudan University, Shanghai)

Prof. Bruno Pollet
(HySA systems, UWC)

Prof. David Key
(Petro SA, UWC)

Prof. Jennifer Key
(Math dept. UWC)

Andeleen Hess
(NPA Cape Town)



Abstract

Aqueous ion-intercalation batteries (AIB's) have the potential to provide both high power for hybrid-electric transport, and low cost bulk energy storage for electric grid supply. However, a major setback to AIB development is the instability of suitable ion-intercalation anode material in aqueous electrolyte. To counter this problem, the use of activated carbon (AC) (a supercapacitor anode) paired against the low cost ion-intercalation cathode spinel LiMn_2O_4 (LMO) provides a stable alternative. This thesis comprises two novel areas of investigation concerning: (1) the development of the AC/LMO cell for high power applications, and (2) the introduction of PbSO_4 as a high capacity alternative anode material paired against LMO for low cost bulk energy storage.

The study on AC/LMO explores the electrode combination's practical specific energy and power capability at high P/E (power to energy ratio) of 50:1 suitable for hybrid electric vehicle batteries. To study the relationship between electrode material loading density, active material performance, and current collector mass contribution, a specially designed cell was constructed for galvanic cycling of different thicknesses of electrode. Between a loading density range of 25 – 100 mg, ~50 mg of total active material between two 1 cm^2 current collectors produced the highest 50:1 P/E ratio values of 4 Wh/kg and 200 W/kg, constituting a 4-fold reduction of the active material values of thin films at 50:1 P/E. The cycling potentials of the individual electrodes revealed that doublings of electrode film loading density increased the LMO electrode's polarization and voltage drop to similar levels as doublings in applied current density. However, by increasing the charging voltage from 1.8 V to 2.2 V, 6 Wh/kg and 300 W/kg was obtainable with minimal loss of energy efficiency. Finally a large-format cell of a calculated 3 Ah capacity at 50:1 P/E was constructed and tested. The cell produced ~60% of the anticipated capacity due to a suspected high level of resistance in the electrode contact points. The overall conclusion to the study was that AC/LMO holds promise for high power applications, and that future use of higher rate capability forms of LMO offers a promising avenue for further research.

The second part of this thesis presents the development of a novel cell chemistry, PbSO₄/LMO, that has yet to be reported elsewhere in existing literature. The cell uses aqueous pH 7, 1 M, Li₂SO₄ electrolyte, and forms an electrode coupling where the PbSO₄ anode charge/discharge is analogous to that in Pb-acid batteries. The average discharge voltage of the cell was 1.4 V and formed a flat charge/discharge plateau. The use of a low cost carbon coating method to encapsulate PbSO₄ microparticles had a marked improvement on cell performance, and compared to uncoated PbSO₄ improved both rate capability and specific capacity of the material. The active materials of the carbon-coated PbSO₄/LMO cell produced a specific energy 51.1 Wh/kg, which, if a 65% yield is possible for a practical cell format, equals 38.4 Wh/kg, which is 15 Wh/kg higher than AC/LMO bulk storage cells at 23 Wh/kg, but lower than Pb-acid batteries at ~25-50 Wh/kg. Interestingly, the specific capacity of PbSO₄ was 76 mAh/g compared to 100 mAh/g in Pb-acid cells. The predicted cost of the cell, providing a 65% value of the active material specific energy for a practical cell can be realized, is on par with Pb-acid battery technology and, importantly, uses $2.3 \times$ less Pb/kWh. The cycling stability achieved thus far is promising, but will require testing over comparable cycle life periods to commercial batteries, which could be anywhere between 5 – 15 years.

UNIVERSITY of the
WESTERN CAPE

Declaration

“I declare that Development is my own work and that all the sources I have used or quoted have been indicated and acknowledged as complete references.”

Julian DV Key



Signed:

Date: November 2013

Contents

Key words.....	ii
Acknowledgements	iii
Abstract.....	iv
Declaration	vi
Contents	vii
List of Tables	ix
List of Figures.....	x
Introduction	14
1.1 Background and motivation of the thesis	14
1.2 Research focus	15
1.2.1 AC/LMO as a high power cell.....	15
1.2.2 A PbSO ₄ /LMO cell for low bulk energy storage.....	16
Literature Review	17
2.1 Aqueous ion-intercalation batteries (AIBs).....	17
2.1.1 Background and basic principles	17
2.1.2 The effect of aqueous electrolyte on cell performance.....	20
2.1.3 Li-ion intercalation materials for ARLBs.....	22
2.1.4 Challenges facing ARLB development	24
2.1.5 Methods for stabilizing intercalation anodes.....	25
2.2 Alternative anode material	25
2.2.1 Zn-LMO	27
2.2.2 Metal-organic framework compound: MIL-53(Fe)·H ₂ O	28
2.2.3 Sulphur: core-shell/polypyrrole.....	29
2.3 AC/LMO: a hybrid supercapacitor/battery system.....	30
2.3.1 Possible applications for AC/LMO cells	32
2.4 AC/LMO at low power: Aquion®.....	34
2.5 AC/LMO at high power.....	36
2.5.1 A battery for long-range FCEVs	36
2.5.2 Considerations for a high power practical AC/LMO cell.....	39
2.6 A Pb anode for low cost/kWh.....	42
2.6.1 Pb/PbSO ₄ : electrochemical behaviour.....	42
2.6.2 A theoretical PbSO ₄ /LMO cell.....	44
2.6.3 Estimated cost/kWh of a PbSO ₄ /LMO cell	44
2.6.4 Possible advantages of a PbSO ₄ /LMO cell	46
Methodology.....	47
3.1 Experimental techniques and instrumentation.....	47
3.1.1 Material preparation and characterization	47
3.1.2 Electrochemical characterization.....	48
3.1.3 Galvanic cycling	49
High power AC/LMO cell development	50
4.1 Introduction	50

4.2 Basic properties & cycling performance of AC & LMO	51
4.2.1 Experimental.....	52
4.2.2 Cyclic voltammetry on LMO and AC electrodes.....	54
4.2.3 Galvanic cycling of thin-film AC and LMO electrodes	56
4.3 A study on AC/LMO electrode material loading density	68
4.3.1 Experimental.....	69
4.3.2 Results and discussion	72
4.3.3 Conclusions	79
4.4 Up-scaling to a 3 Ah high power cell.....	80
4.4.1 Testing large-format electrodes	81
4.4.2 Construction and cycling of a 3 Ah cell	86
4.5 Conclusions	95
Development of a PbSO₄/LMO cell.....	96
5.1 Introduction	96
5.2 Synthesis and characterization of PbSO ₄ micro-particles	97
5.2.1 Introduction	97
5.2.2 Experimental.....	98
5.2.3 Results and discussion	98
5.2.4 Conclusions	100
5.3 Electrochemical characterisation of PbSO ₄ electrode film.....	101
5.3.1 Experimental.....	101
5.3.2 Results and discussion.....	102
5.3.3 Conclusions	108
5.4 Carbon-coated PbSO ₄ (ccPbSO ₄)	108
5.4.1 Experimental.....	108
5.4.2 Results and discussion	109
5.4.3 Conclusions	115
5.5 PbSO ₄ -doped activated carbon (AC).....	116
5.5.1 Introduction	116
5.5.2 Experimental.....	117
5.5.3 Results and discussion	117
5.6 Predictions on cost/kWh and Pb usage.....	119
5.6.1 Cost/kWh of a PbSO ₄ /LMO practical cell.....	119
5.7 Conclusions	120
Conclusions & Future work	122
6.1 Conclusions on high power AC/LMO cells	122
6.2 Future work on high power AC/LMO cells	123
6.3 Conclusions on PbSO ₄ /LMO cells	123
6.4 Future work on PbSO ₄ /LMO cells	124
References	125

List of Tables

2.1	ARLBs compared to other battery technologies	21
2.2	Timeline of various studies on ARLB cells	24
2.3	Battery power and energy requirements for FCEV 4-seat (40 kW) car, adapted from [8]	37
2.4	Considering mass contributions of cell components on thin film electrodes. Above: components of electrode film, and below, the thin film cell tested by Wang et al., 2005.....	40
2.5	Cost calculations for a 40% active material mass cell at P/E 2:1 and P/E 50:1	41
2.6	Cost/kWh prediction for a 65% active material mass PbSO ₄ /LMO cell at P/E 1:5 (i.e. at maximum specific energy).....	45
4.1	Setting and targets for establishing a comparison of active materials	58
4.2	Electrode thicknesses and the corresponding masses of electrode material	70
4.3	Comparison of specific energy and specific power of active material (AM) and cell total, using 25, 50 and 100 mg of active materials.....	75
4.4	Cells charged to 2.2 V. Comparison of specific energy and specific power of active material (AM) and cell total, using 25, 50 and 100 mg of active materials.....	78
4.5	Effect of cell voltage on material quantities for a 3 Ah high power cell at 50:1 P/E. .82	
4.6	Total mass and component masses of the 3 Ah cell on final assembly	90
5.1	Cost/kWh prediction for a 65% active material mass PbSO ₄ /LMO cell at P/E 1:5 (i.e. at maximum specific energy).....	119

List of Figures

2.1	Schematic of ARLB charge/discharge process, showing Li-ion movement on discharge above, adapted from [2], and below: VO ₂ /LMO crystal space-filled models adapted from [12] and www.cmich.edu/petko1vg/nano.htm	18
2.2	ARLB electrode materials, showing their Li-ion intercalation voltage ranges (right panel) against the pH-dependent electrochemical window of water (left panel). Cathode materials (dark blue) and anodes (light blue).	19
2.3	Alternative anodes for LiMn ₂ O ₄	26
2.4	Schematic of the Zn-LMO cell showing the charge/discharge process	27
2.5	Voltage profile for a Li/ MIL-53(Fe)·H ₂ O half-cell cycled between 1.5 and 3.5 V at a C/40 rate, showing an ideal flat voltage plateau range for an AIB anode [42].	28
2.6	Sulphur/polypyrrole as an anode in L ₂ SO ₄ (aq) electrolyte. Above: charging schematic, below: (left) appropriate AIB anode voltage and (right) 100 stable cycles [43].	29
2.7	Schematic of the AC/LMO hybrid supercapacitor/battery (left), and (right) voltage cycling profile showing the cell voltage and respective voltages of the individual electrodes during charge/discharge [6].	30
2.8	Cycling stability AC/LMO (left) and Ragone plot (right) of AC/LMO compared to an AC/AC cell over increasing current density [6].	32
2.9	Ragone plot of various battery technologies showing the position of AC/LMO and three different ARLB cells after considering a 40% reduction for practical cell values, compiled from [6, 44-48].	33
2.10	First commercial application of an AIB system by Aquion® [4].	35
2.11	Example of the 1.4:1 fuel cell/battery power ratio, and 50:1 battery P/E ratio, for a long-range drive-cycle FCEV	37
2.12	Ragone plot of AC/LMO cell with 40% practical cell reduction, showing 50:1 P/E ratio, adapted from [6].	37
2.13	Ragone plot of battery technologies intersecting the 50:1 P/E ratio line, showing the possible position of a practical AC/LMO cell adapted from [6, 44-48]	38
2.14	Cost of Li-ion battery at 50:1 W/Wh ratio. Graph shows extrapolation to 50:1 ratio, adapted from [51]	38
2.15	Cyclic voltammetry of Pb metal in H ₂ SO ₄ (top left) [52] and Na ₂ SO ₄ (aq) (top right) [40] show corresponding cathodic peaks relating to Pb/PbO ₄ conversion (-0.35 V vs. SHE). Below: Pourbaix diagram of Pb (left) and schematic of Pb charge/discharge (right) [53].	43
3.1	Schematic of three-channel cycle testing. Channel 1 measures the voltage of the anode v SCE reference electrode; channel 2 cycles the cell and measures cell voltage; and channel 3 measures the cathode voltage v SCE.	49
4.1	Photograph of the three-electrode cell (top) showing 1 cm ² area of working electrode on the left side of vial, SCE reference electrode in the middle and large auxiliary electrode on right side of the vial. Below are SEM images of commercial	

LMO (left) and AC (right) used in this study, showing wide particle size range between ~0.1 to 10 μm .	53
4.2 Cyclic voltammetry of a 1 cm^2 10 mg LMO film electrode at a scan rate 5 mV/sec. In anodic scan (analogous to charging) the double peaks of Li^+ intercalation at +1.0 and +1.2 V vs. SHE occur prior to onset of oxygen evolution at +1.35 V.	54
4.3 Cyclic voltammetry of a 1 cm^2 10 mg AC film electrode at a scan rate 5 mV/sec. The plot has the characteristic shape of EDLC with onset of hydrogen evolution occurring at ~ -0.75 V vs. SHE in the cathodic scan direction.	55
4.4 Schematic showing derivation of the 32 Wh/kg from AC/LMO active materials, adapted from [6] to show specific capacity.	57
4.5 Charging thin-film AC electrode at 300 mA/g to a series of lower potentials from -0.6 to -0.9 V vs. SHE (above). Effect on coulombic efficiency (below), where cycle numbers 1 to 7 represent -0.6 to -0.9 V vs. SHE.	60
4.6 Charging thin-film LMO electrode at 600 mA/g to a series of higher potentials from +1.2 to +1.5 V vs. SHE (above). Effect on coulombic efficiency (below), where cycle numbers 1 to 7 represent +1.2 to +1.5 V vs. SHE.	61
4.7 Charging AC/LMO (2:1) at 200 mA/g up to 2.2 V, approaching the onset of hydrogen evolution on AC.	62
4.8 Full charge holding for 30 min at 1.8 and 2.2 V on AC/LMO (2:1).	63
4.9 Three voltage/time plots of AC/LMO (2:1) charged 1.8 V over 400 – 25 mA/g showing: cell voltage (top); LMO potential (middle), and; AC potential (bottom).	65
4.10 Three voltage/specific capacity plots of AC/LMO (2:1) charged to 1.8 V at 400 – 25 mA/g showing: cell voltage (top); LMO potential (middle), and; AC potential (bottom).	66
4.11 Ragone plot and energy efficiency of AC:LMO (2:1) charged to 1.8 V 400 – 25 mA/g. Showing maximum energy efficiency at 50 mA/g.	67
4.12 SEM of the 304 stainless steel 80-mesh current collector at $169 \times \text{mag}$ (top left). Photograph of disc electrodes (top right) with loading densities of 10 – 320 mg/cm^2 of LMO electrode dough (left of picture), and 10 – 640 mg/cm^2 of AC electrode dough (right of picture). Photographs of the adjustable test cell (below) with close-up of electrode assembly showing electrodes and cotton cloth separator.	71
4.13 Effect of current density on three loading densities of active material at 2:1 mass ratio: 25 mg (top), 50 mg (middle) and 100 mg (bottom) charged to 1.8 V.	73
4.14 Ragone plot of cells charged to 1.8 V, showing cell total specific energy, specific power and energy efficiency using 25, 50 and 100 mg loading densities of active materials (each cycled at 600, 800, 1000, 1200 and 1400 mA/g).	75
4.15 Effect of current density on three loading densities of active material at 2:1 mass ratio: 25 mg (top), 50 mg (middle) and 100 mg (bottom) charged to 2.2 V.	77
4.16 Ragone plot of cells charged to 2.2 V, showing cell total specific energy, specific power and energy efficiency using 25, 50 and 100 mg loading densities of active materials (each cycled at 600, 800, 1000, 1200 and 1400 mA/g).	78
4.17 Large-format (100 mg loading density) electrodes tested for the 3 Ah (50:1 P/E) power cell, showing paper sleeve separators and tab connection points for the bolted bus bar.	83
4.18 Large-format (100 mg loading density) AC/LMO electrodes cycled at 600 – 1400 mA/g to 1.8 V charge (above), and 2.2 V charge (below).	85

4.19 Total cell specific energy and specific power of large-format AC/LMO electrodes with 100 mg loading density cycled at 600 – 1400 mA/g to 1.8 V charge and 2.2 V charge.	86
4.20 Electrode assembly of the 3 Ah cell, showing bolt bus bar and paper sleeve separators (above), and final 60-electrode assembly wrapped in PTFE tape (below)...	88
4.21 Final assembly of the 3 Ah cell in casing (above), and connection to the battery cycling machine (below). The cell measured ~10×10×5 cm (500 ml) and had a total mass of ~747 g.	89
4.22 Galvanic cycling of the of the 3 Ah cell at 3 A showing the less than 4.6 Ah anticipated capacity of 2.6 Ah.	92
4.23 Galvanic cycling of the 3 Ah cell at 10 A (above) and 30 A (below) showing voltage drop.	93
4.24 Corrosion of the nickel-plated bolt busbars, nuts and washers after overnight cycling of the 3 Ah AC/LMO at 3 A	94
5.1 SEM images showing smooth-edged morphology of the PbSO ₄ microparticles. ‘A’ low magnification (20 K) and ‘B’ high magnification (80 K).	99
5.2 TEM images showing crystalline morphology of the PbSO ₄ nanoparticle agglomerations. ‘A, B’ low resolution TEM, and ‘C, D’ HR-TEM.	99
5.3 EDS spectrum (top) showing Pb, S and O element composition of PbSO ₄ microparticles, and XRD pattern (below) of PbSO ₄ micro-particles with ‘Anglesite’ crystal structure.	100
5.4 Cyclic voltagram of Pb/PbSO ₄ micro-particles in 1 M Li ₂ SO ₄ (aq) at a scan rate of 5 mV/sec	102
5.5 Galvanic cycling of a PbSO ₄ /LMO cell at 0.05 – 0.01 A/g (1.2-1.7 V)	103
5.6 Effect of applied current density on the specific capacity and coulombic efficiency of PbSO ₄ /LMO.	104
5.7 Cycling of PbSO ₄ /LMO at ~0.1 C with a 1:0.8 active material ratio	105
5.8 40-day cycling of 1:0.8 (PbSO ₄ /LMO) active material ratio at ~0.2 C. Specific capacity of PbSO ₄ (right ‘y’ axis) and coulombic efficiency (left ‘y’ axis).	106
5.9 SEM images of PbSO ₄ electrode films before and after 100 cycles at 0.2 C rate. ‘A’ pristine “un-cycled” electrode film, and “B-D” show a magnification series of the interesting crystal formations that developed after 100 cycles. Below: EDS spectrum the of surface showing strong presence of Pb.	107
5.10 SEM images of ccPbSO ₄ showing carbon coating. ‘A’ uncoated PbSO ₄ , ‘B – D’ 5-min heated cc PbSO ₄ at increasing magnification.	110
5.11 TEM images of ccPbSO ₄ showing evidence of carbon coating (bottom right).	111
5.12 XRD plots of ccPbSO ₄ and uncoated PbSO ₄ showing differences in minor peaks and possible indication of graphitic carbon presence.	111
5.13 Galvanic cycling of ccPbSO ₄ at 0.4 C showing stable charge/discharge. Lower plot shows PbSO ₄ /LMO cell voltage.	112
5.14 40-day galvanic cycling of ccPbSO ₄ at 0.4 C showing stable charge/discharge at 95% coulombic efficiency, <5% loss of capacity. Specific capacity of PbSO ₄ (right ‘y’ axis) and coulombic efficiency (left ‘y’ axis).	113
5.15 40-day galvanic cycling of ccPbSO ₄ at 0.2 C showing stable charge/discharge at 93% coulombic efficiency, <5% loss of capacity. Specific capacity of PbSO ₄ (right ‘y’ axis) and coulombic efficiency (left ‘y’ axis).	114

5.16 24-h full charge holding period of a ccPbSO ₄ /LMO cell cycled at 0.1 C showing insignificant loss of charge or voltage resulted from the holding period.....	115
5.17 PbSO ₄ <i>in situ</i> doping of AC in an AC/LMO cell. The cell was interrupted at the tenth cycle cell where the AC electrode was removed, doped, returned to the cell and cycling resumed. The cell capacity ('y' axis) was approximately doubled by the doping.....	118

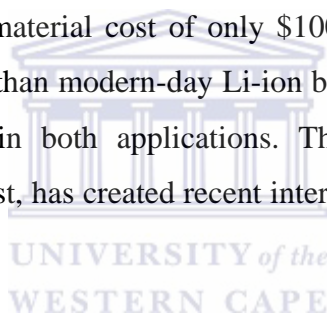


Chapter 1

Introduction

1.1 Background and motivation of the thesis

With the advent of renewable energy and electric transport comes demand for large rechargeable batteries for electric vehicles (EVs), hybrid vehicles (HEVs) and electrical energy storage (EES) at MWh scale. However, the required size of such batteries and the foreseeably large scale of their implementation present major challenges concerning the abundance and cost of their component materials. Recent targets published by the US department of energy (DOE) include: (1) a 50% cost reduction on existing EV battery price [1]; (2) a material cost of only \$100/kWh for grid EES batteries [2] (at least four times cheaper than modern-day Li-ion batteries) and, (3) a lifespan of at least 15 years for batteries in both applications. The challenge to meet these targets, particularly regarding cost, has created recent interest in alternative, potentially cheaper, battery chemistries.



AIBs (aqueous ion-intercalation batteries) are an emerging battery category that uses aqueous electrolyte and electrode materials that intercalate alkali ions (Li^+ , Na^+ or K^+). The cell format offers potentially long-term cycle life with high specific power (W/kg) suitable for HEVs, and low cost/kWh storage for EES. These features arise from using aqueous electrolyte, which facilitates faster ion intercalation and has cheaper costs than its organic counterpart in Li-ion batteries [3]. However, at approximately half the cell voltage of Li-ion batteries, the material costs of AIBs need to be at least half that of standard Li-ion batteries to provide lower cost/kWh.

Recently, a new company, Aquion®, has developed a low cost/kWh AIB cell intended for low power use in bulk energy storage [4]. The cell's electrodes comprise an activated carbon (AC) anode and an ion intercalation cathode LiMn_2O_4 (LMO). However, the cell is limited in specific energy (Wh/kg) by the AC anode, and constitutes a “hybrid battery” (half supercapacitor half battery) where AC stores charge

by EDLC (electrochemical double layer capacitance). The choice of the low specific capacity AC reflects that no sufficiently stable ion-intercalation anode material has been found to date. Thus far, all suitable ion-intercalation anode material appears to suffer major capacity loss prior to 100 cycles in aqueous electrolyte [5]. On the other hand, cathode materials such as LiMn_2O_4 (LMO) have proved extremely stable, lasting up to and beyond 10,000 cycles [3, 6, 7]. Therefore, the search for stable anode material is a central focus of the research field.

1.2 Research focus

1.2.1 AC/LMO as a high power cell

Prior to the adoption of the AC/LMO cell format by Aquion®, the first published study on AC/LMO by Wang et al [6], demonstrated the cell could supply high specific power with high specific energy retention in thin films of electrode material. The authors suggested that if an estimated 40% yield of the cell's active materials could be maintained, a practical cell format of 400 W/kg and 8 Wh/kg at a 50:1 power to energy ratio could be realized. These 'specific' properties are appropriate for high power applications such as batteries for power assist and regenerative braking in HEVs [8]. However, to counter the mass contribution of current collectors requires sufficient electrode material film thickness or loading density. This presents the problem that thicker films have higher resistance and lower power capability [4, 9]. Therefore, to determine whether AC/LMO could provide the proposed high power cell in practical cell format, the main objectives of this study were as follows:

- Confirm experimentally the previously reported high specific power and specific energy of AC/LMO in thin film electrode format (Ch. 4 Section 4.2)
- Determine the effects of AC/LMO electrode material loading density on specific power, specific energy and energy efficiency (Ch. 4, Section 4.3)
- Construct and test an up-scaled AC/LMO cell in practical format (Ch. 4, Section 4.4)

1.2.2 A PbSO₄/LMO cell for low bulk energy storage

Considering the need for cheaper, higher specific energy anodes for AIBs, a variety of mostly unexplored, high specific capacity options exist. The four common aqueous battery anodes include: Zn (re. zinc-carbon battery), MH (re NiMH battery), Fe (re Fe/NiOOH battery) and Pb (re. Pb-acid battery). While all are potential candidates against various ion intercalation cathodes, all operate at the extreme ends of the pH scale. For the mid-range pH requirement of LMO [10], only Pb (on the basis of its Pourbaix diagram) presents a viable option and has yet to be explored. Furthermore, the low cost and high specific capacity of Pb were attractive features for its investigation in the present study (Ch. 2 Section 2.6, and Ch. 5). Therefore, the main objectives of this part of the study were:

- Determination of the electrochemical behavior and charge/discharge capacity of Pb anode material in pH 7 salt based electrolyte (Ch. 5 Section 5.3)
- Cell cycling (galvanic cycling) of Pb anode material against an LMO cathode to determine achievable specific energy and cost/kWh of storage (Ch.5, Sections 5.3 – 5.6).
- Comparison of obtained testing results and cell development to theoretical values of the cell chemistry (Ch. 5, Section 5.7)

Chapter 2

Literature Review

2.1 Aqueous ion-intercalation batteries (AIBs)

2.1.1 Background and basic principles

The concept of using ion-intercalation compounds for energy storage in aqueous electrolyte was first put forward by Dahn et al., in 1994 [11]. Considering the wealth of Li-ion intercalation compounds discovered by Li-ion battery research, and their attractive properties of high specific capacity (Ah/kg) and stable cycling nature, the concept of an “aqueous Li-ion battery” placed these properties in a new setting. The potential advantages of the aqueous electrolyte are:

- A cheaper, safer, and more environmentally friendly alternative to the high voltage organic electrolyte-based Li-ion battery.
- Lower resistance of Li^+ intercalation in aqueous electrolyte, which offers much faster charge/discharge speeds than in organic electrolyte.

In the literature, aqueous Li-ion batteries are now commonly referred to as ARLBs (aqueous rechargeable Li-ion batteries). In the present study, “AIBs” provides an umbrella term because the concept has since extended to other alkali ions, such as Na^+ and K^+ and their related intercalation host materials.

Fig 2.1 (overleaf) shows a schematic of the first electrode materials used by Dahn et al., [11]. The cell comprised a vanadium oxide (VO_2) anode, a lithium manganese oxide (LiMn_2O_4 or “LMO” abbreviated) cathode and 5 M LiNO_3 (aq) electrolyte. The cell’s operating principle is analogous to standard Li-ion batteries. In the charging reaction (forward reaction) Li^+ ions de-intercalate from LMO and intercalate into VO_2 , and the reverse reaction occurs on discharge, equation (2.1):

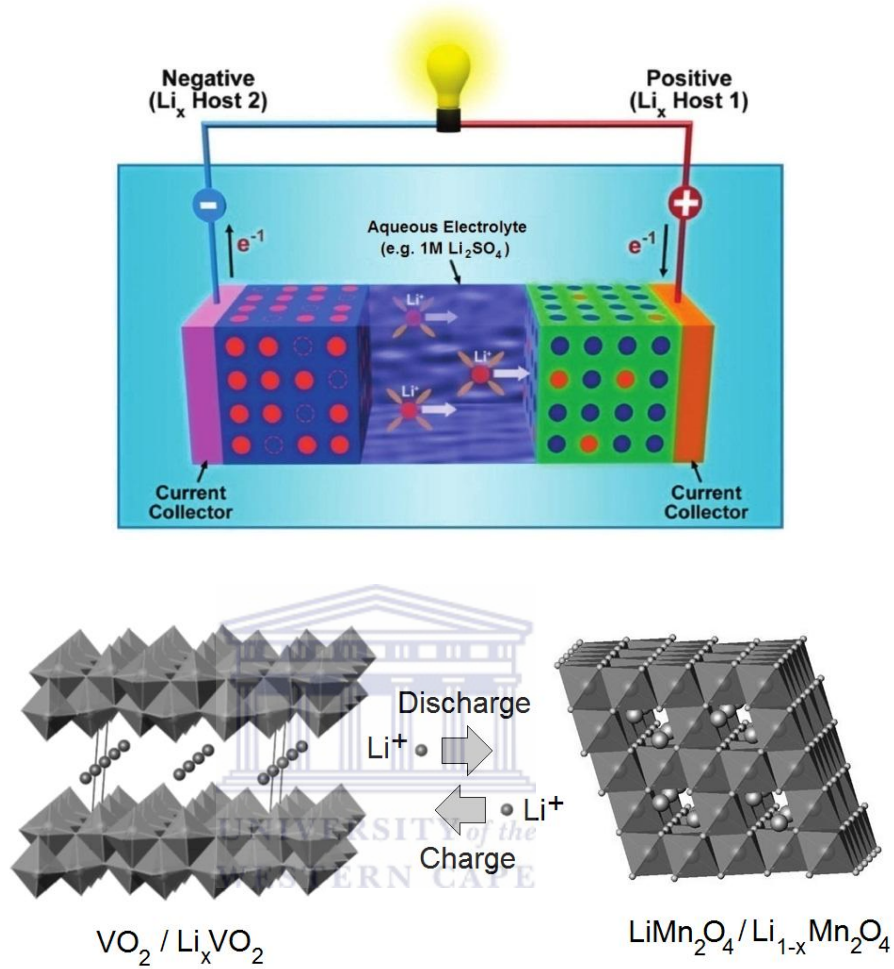
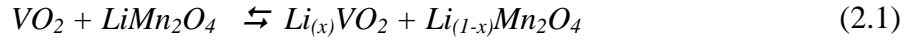


Fig 2.1 Schematic of ARLB charge/discharge process, showing Li-ion movement on discharge above, adapted from [2], and below: VO₂/LMO crystal space-filled models adapted from [12] and www.cmich.edu/petko1vg/nano.html

The potential difference of Li⁺ intercalation between VO₂ and LMO provided an average discharge voltage of ~1.5 V, which resulted in a specific energy of 75 Wh/kg considering the mass of active materials (i.e. VO₂ and LMO). The cell was cycled at only a 0.1 C rate (10 h charge/discharge) due to the low electrical conductivity of the VO₂ material used, which equates to a specific power of only 7.5 W/kg. Furthermore, the VO₂/LMO cell failed to cycle beyond 50 cycles, by which point it had lost more than 50% of its capacity. However, the cell successfully proved the concept, and gave promise for further investigation.

Since the first work of Dahn et al., ARLBs have generated considerable research interest. Fig 2.2 shows Li-ion intercalation materials that have been investigated in the aqueous cell format to date. The blue boxes in the figure show the potential range of Li-ion intercalation of anode (light blue) and cathode materials (dark blue), which fall within electrochemical window of water. The pink, yellow, orange and red boxes show the potentials of some common anode materials used in standard Li-ion batteries in organic electrolyte. The narrower available potential difference between anode and cathode materials in water limits their cell voltage to a maximum of ~2 V (when considering oxygen and hydrogen evolution overpotentials).

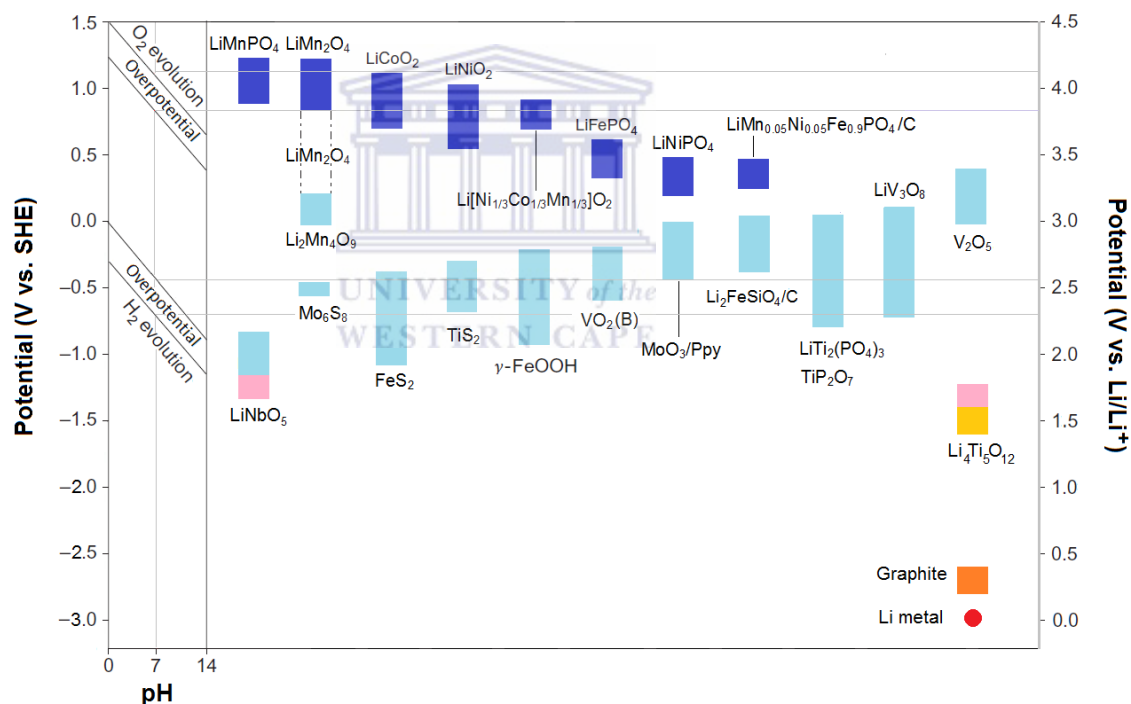


Fig 2.2 ARLB electrode materials, showing their Li-ion intercalation voltage ranges (right panel) against the pH-dependent electrochemical window of water (left panel). Cathode materials (dark blue) and anodes (light blue).

2.1.2 The effect of aqueous electrolyte on cell performance

In being limited in cell voltage by the electrochemical window of water, ARLBs cannot reach the high specific energy (Wh/kg) of standard Li-ion batteries. This can be seen from equation (2.2) below:

$$SE = \frac{Q \times V}{m} \quad (2.2)$$

...where 'SE' is specific energy (Wh/kg), 'Q' is capacity (Ah), 'V' is cell voltage and 'm' is mass (kg).

At approximately half the cell voltage of standard Li-ion batteries, ARLBs using electrodes of the same specific capacity 'Q' would have only half the specific energy. Therefore, for applications where high specific energy is vital such as portable electronics and EV batteries, ARLBs would be at least twice the size and weight of Li-ion batteries. However, the possible applications of ARLBs could include:

- (1) Low cost/kWh storage, e.g. for bulk, stationary, electrical energy storage (ESS)
- (2) low cost/kW storage, e.g. for bulk, stationary, grid power smoothing applications
- (3) High power to energy ratio (P/E) batteries, e.g. for HEVs and large transport

The first application concerns their material cost/kWh (or cost/Wh), which is a function of material cost (\$/kg), specific energy (Wh/kg) and lifespan (equation 3).

$$Cost/Wh = \frac{\$/kg}{Wh/kg \times Lifespan} \quad (2.3)$$

Equation (2.3) shows that with standard Li-ion batteries of the same lifespan but double the Wh/kg of ARLBs, the required \$/kg of ARLB material would have to be at least $2 \times$ cheaper than that of Li-ion batteries to provide cheaper cost/Wh. However, this is entirely possible since the high price of Li-ion batteries (at cheapest \$400/kWh [13]), concerns the use of expensive organic electrolyte and its related infrastructure.

The second and third applications mentioned above relate to specific power (W/kg). Aqueous electrolyte has a much higher ionic conductivity than organic solvent electrolyte by at least two orders of magnitude [3, 5], which significantly lowers the cell resistance and allows considerably higher current density. Therefore, higher specific power (SP) can be realized according to equation (2.4):

$$SP = \frac{I \times V_{ave.}}{m} \quad (2.4)$$

...where ‘SP’ is specific power (W/kg), ‘I’ is current (A), ‘V ave.’ is average cell voltage and ‘m’ is mass (kg).

In practice, reports show that some recent ARLB electrodes provide up to ten times higher specific power than standard Li-ion batteries [5, 7], (see Table 2.1). This means their charge/discharge can be ten times faster. Since ARLBs operate at half the voltage of standard Li-ion cells, equation (4) indicates that to obtain the ten times greater power density would require a twenty times greater current density. This shows the remarkable improvement in conductivity offered by aqueous electrolyte. Furthermore, it can also be estimated that the cost/kW of specific power could also be around ten times cheaper using ARLBs in place of standard Li-ion batteries. Table 2.1 shows the position ARLBs could therefore occupy in comparison to other battery technologies.

Energy system	Specific power (W/kg)	Specific energy (Wh/kg)	Cost/kWh (\$/kWh)	*Cost/kW (\$/kW)	Ref
Li-ion	150 – 3,500	50 – 300	400 – 2,000	30 – 550	[14]
Ni-MH	< 50 – 1,500	20 – 100	300 – 1,000	20 – 500	[14-16]
Pb-Acid/Pb-C	10 – 1,000	20 – 45	150 – 600	12 – 700	[2, 17, 18]
EDLC	2,000 – 5,500	0.5 – 6	>1000	< 5	[14]
ARLBs	> 1,000	10 – 55	(?)	< 10**	[5, 7]

* Estimated from references cited in table

**Estimated from reference [7]

Table 2.1 ARLBs compared to other battery technologies

2.1.3 Li-ion intercalation materials for ARLBs

As shown previously in Fig 2.2, the range of possible Li-ion intercalation materials for ARLBs must have intercalation potentials that fall within the electrochemical window of water. To achieve a cell voltage of higher than 1 V, anodes require Li-ion intercalation potentials close to or below 0 V vs. SHE, and cathodes at or above +0.5 V vs. SHE.

2.1.3.1 Cathode Li-ion intercalation materials

The common Li-ion battery cathodes LiMn_2O_4 “LMO” (spinel), LiCoO_2 “LCO” and $\text{Li}[\text{Ni}_{1/3}\text{Co}_{1/3}\text{Mn}_{1/3}]\text{O}_2$ “NMC” (layered oxides), LiFePO_4 “LFP” (Phospho-olivine) materials have all been shown to provide stable cycling in aqueous media, and capable of >80% capacity retention above at least 1,000 cycles at slow and fast C rates [3, 5, 10]. In general, the choice of LMO has been popular in studies owing to its high standard potential of Li-intercalation, low cost, and high stability [6].

- *LMO structure and properties*

Among various manganese oxide materials, spinel LiMn_2O_4 first proposed by Thackeray [19] is the most attractive cathode material for ARLBs. It has a cubic spinel structure closely related to the layered structure of $\alpha\text{-NaFeO}_2$, with a cubic-close packed array of oxygen anions (Fig 2.1). Manganese cations occupy half the octahedral interstitial sites, where Li^+ occupies one eighth of tetrahedral sites. The Mn_2O_4 framework provides three-dimensional interstitial space for Li^+ ion transport maintaining its structure over the compositional range Li_xMnO_4 ($0 \leq x \leq 1$) by changing the average Mn oxidation state between 3.5 and 4.0 on charge and discharge respectively. Typically, LiMn_2O_4 is produced by a two-stage solid state thermal reaction between a lithium salt, e.g. Li_2CO_3 , with MnO_2 using a 0.55 ratio of Li/Mn, at 530°C for 5 h, followed by 700°C for 24 h in air and 3 h cooling period [20].

In aqueous electrolyte, LiMn_2O_4 has proved particularly stable in comparison to its cycling performance in organic electrolyte, where its dissolution occurs due to attack from HF, an oxidation product of the Li^+ salt, LiPF_6 , used in organic electrolyte [21]. Studies on nano-morphologies of LiMn_2O_4 including nano-rods [22], nano-chains [23],

and micron-thin films [24, 25], have produced extremely stable capacity above 10,000 cycles with >90% capacity retention at very high charge and discharge rates, or C rates up to 100 C (36 sec charge time). In another recent study, porous LiMn_2O_4 consisting of highly crystalline nano-grains have been prepared using polystyrene as a template [26]. The material withstands current densities as high as 10 A/g (~90 C), while retaining 93% of the total 118 mAh/g capacity after 10,000 cycles at 100% DOD (depth of discharge) and providing power density up to 10 kW/kg. This suggests it can be used for a lifetime without maintenance, since the crystalline nano-structure and porous morphology aid rapid electron conductivity and Li^+ transport with minimal structural stress. The results hold great promise for the future development of high powered ARLBs in practical applications, providing that cost effective means of nanomaterial production can be developed.

2.1.3.2 Anode Li-ion intercalation materials

The majority of studies on ARLB anodes have been on either vanadium oxides or NASICON (sodium super ionic conductor) lithium titanium phosphate ($\text{LiTi}_2(\text{PO}_4)_3$), with the recent addition of molybdenum sulphide (Chevrel phase) compound (Mo_6S_8) and molybdenum oxide (MoO_3) (Table 2.2). The table shows a timeline of ARLB anode/cathode combinations tested from 1994 to present. Not all references have reported the specific energy values of the cells depending of the focus of investigations. Table 2.2 also shows that the cycling stability of the majority of ARLBs at low C rates results in rapid loss of capacity. In the case of vanadium oxides and NASICON low C rates were required to obtain the maximum specific capacity from the electrodes owing to their low electrical conductivity. The suspected reasons for the capacity loss are discussed below (Section 2.1.4). In the recent high rate (70 C) tests on MoO_3/Ppy (polypyrrole-coated) (Table 2.2), promising cycling stability at high C rate with extremely high specific energy retention has been reported [27]. Similarly, polypyrrole coated V_2O_5 on MWCNTs (multi walled carbon nanotubes) has been reported to produce 90% capacity retention over 500 cycles [28]. However, as promising as both these recent cases may seem, they both constitute very high cost/kWh materials, and despite their phenomenal energy retention at high C rate, the total span of test time of 500 cycles at high 60 C rate represents only a few hours.

Timeline	Anode/Cathode		Wh/kg	Capacity retention (%) / cycle	C rate	Ref
1994	VO ₂ (B)	LiMn ₂ O ₄	75	Failed/50	0.1	[11]
2000	LiV ₃ O ₈	LiNi _{0.81} Co _{0.19} O ₂	-	40/100	-	[29]
2007	LiV ₃ O ₈	LiCoO ₂	-	36/100	1	[30]
2007	TiP ₂ O ₇	LiMn ₂ O ₄	-	37/25	0.1	[31]
2007	LiTi ₂ (PO ₄) ₃	LiMn ₂ O ₄	58	36/25	0.1	[31]
2008	LiV ₃ O ₈	Li[Ni _{1/3} Co _{1/3} Mn _{1/3}]O ₂	-	55/10	-	[32]
2009	LiTi ₂ (PO ₄) ₃	LiMn _{0.05} Ni _{0.05} Fe _{0.9} PO ₄ /C	78	52/50	-	[33]
2010	LiTi ₂ (PO ₄) ₃	LiFePO ₄	-	85/50 (O ₂) 90/1000 (-O ₂)	0.1 6	[10]
2012	Mo ₆ S ₈	LiMn ₂ O ₄	65	-	60	[34]
2012	MoO ₃ /PPy	LiMn ₂ O ₄ nanochain	45	90/150	70	[27]
2012	V ₂ O ₅ /PPy/MW-CNTs	LiMn ₂ O ₄	55	90/500	50	[28]

Table 2.2 Timeline of various studies on ARLB cells

2.1.4 Challenges facing ARLB development

Despite nearly 20 years of research, no appropriate-voltage ion-intercalation anode material has proved sufficiently stable to retain a viable percentage of its capacity beyond 100 cycles below 10 C [5, 7]. In battery life span, this is unacceptably low and is approximately five times lower than the most short-lived battery chemistries such as lead acid cells [2].

Various reasons appear to account for the lack of anode stability. In the case of VO₂, LiV₃O₈, LiV₂O₅ [5] its dissolution occurs in aqueous electrolyte, and in the case of NASICON structures, LiTi₂(PO₄)₃ and TiP₂O₇, capacity loss is linked to reaction with dissolved oxygen in the aqueous electrolyte [10]. It has also been proposed that possibly for both cases, intercalated Li-ions at voltages below -0.3 V vs. SHE will react with both water and oxygen at all pH values, and in NASICON structures oxygen may irreversible oxidize all Ti³⁺ species in to Ti⁴⁺ to form TiO₂, phosphate, and de-intercalated Li-ion (personal communication with authors of [5]).

2.1.5 Methods for stabilizing intercalation anodes

Attempted methods to improve the cycling stability of the above mentioned anode ion-intercalation materials have included: carbon coating of the material (to prevent dissolution and improve their electrical conductivity) [35], use of salt saturated electrolyte (to reduce the concentration of water and dissolved oxygen) [34, 36, 37] and removal of dissolved oxygen [10]. However, none of these methods have significantly either improved stability or viability, and in the case of removing oxygen, the benefits (at least a 5 fold increase in stability) are outweighed by the difficulty of maintaining the cell in an oxygen free environment, particularly when usefully high cathode potentials evolve small quantities of oxygen [6].

2.2 Alternative anode material

In the absence of stable ion intercalation anodes, alternative anode materials can provide an interim means to enable the use of stable cathode material such as LMO. The choice of anode material determines what kind of cell will be achieved by the combination, i.e. high specific energy, high specific power, long lifespan, low cost, etc. Therefore, providing the material can function at the same pH as the chosen cathode, the choice of anode material could be anything from another battery system or even a supercapacitor electrode. However, the use of LMO at pH 7 is particularly attractive given its low cost, excellent cycling stability, high capacity of ~100 mAh/g in aqueous electrolyte and high voltage range of 0.8 – 1.23 V vs. SHE [5]. Reports have shown acidic electrolyte below pH 5 causes dissolution of LMO [38] and the phenomenon of irreversible hydrogen ion intercalation at low pH [5, 39]. On the other hand, the use of LMO above pH 7 would result in very limited capacity due to the upper voltage limitation of the aqueous electrolyte.

Fig 2.3 shows the pH range of Li⁺ intercalation against the pH working range of some common alternative anode materials possibilities. Of the four common battery anodes from Pb-acid, NiMH, Zn-MnO₂ and Fe-NiOOH cells, only Pb overlaps with the midrange pH required for the LMO cathode function. While there appears to be no

reports of its use as a battery anode at this pH, a report on the electrochemical behavior of Pb in 1 M Na_2SO_4 [40] suggests its conversion to PbSO_4 occurs at similar voltage to that in the acidic electrolyte of Pb-acid batteries. The possibility of using Pb and further examination of its characteristics are discussed in Section 2.6. The use of the other three common battery anodes (Zn, MH, and Fe) would require an intercalation cathode that intercalates Li^+ below 0.4 V vs. SHE in the pH 12-14 range. Such a cathode could be chosen from Fig. 2.2 (shown previously Section 2.1.1) and could possibly include LiNiPO_4 , $\text{LiMn}_{0.05}\text{N}_{0.05}\text{PO}_4$ or the super-lithiated form of LMO, $\text{Li}_2\text{Mn}_4\text{O}_9$. Fig 2.3 also shows the broad pH range of activated carbon (AC) which is a supercapacitor material of high stability and forms the topic of Section 2.3 (below).

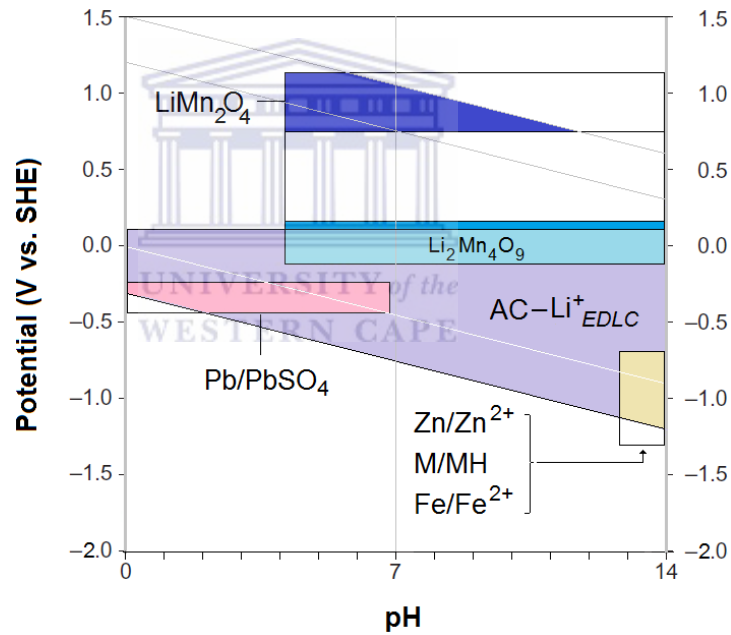


Fig 2.3 Alternative anodes for LiMn_2O_4 . The dark blue area shows the pH range where LiMn_2O_4 (LMO) can be used as a cathode. $\text{AC-Li}^+_{\text{EDLC}}$ and Pb/PbSO_4 fall within compatible pH range as anodes. Zn/Zn^{2+} , M/MH (metal hydrides) and Fe/Fe^{2+} could potentially provide anode systems against a $\text{Li}_2\text{Mn}_4\text{O}_9$ cathode at pH 13-14.

2.2.1 Zn-LMO

A recent publication by Jin Yang et al., in 2012, has demonstrated a cell that uses a Zn metal anode against an LMO cathode electrode in pH 4 mixed ion electrolyte comprising 3 M LiCl and 4 M ZnCl₂ [38]. On charging the Zn²⁺ ions in the electrolyte electrodeposit on the anode to form Zn metal, and Li⁺ ion de-intercalate from LMO to balance the loss of cationic charge in the electrolyte, and on discharge the process is reversed (Fig. 2.4).

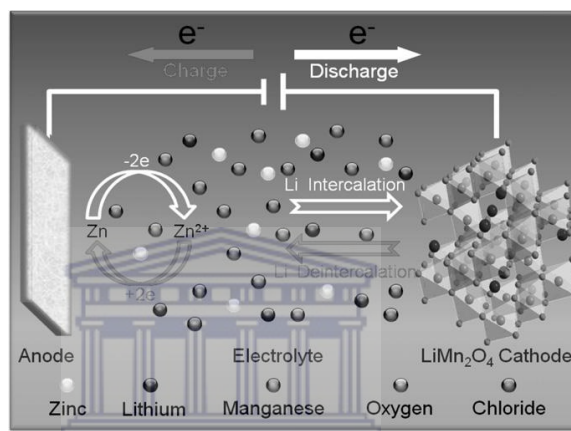


Fig 2.4 Schematic of the Zn-LMO cell showing the charge/discharge process [38].

The cell has a high voltage for an aqueous system, at 2 V (similar to Pb-acid), owing to the low electroplating voltage of Zn/Zn²⁺ (~0.7 V vs. SHE) and high overpotential for hydrogen evolution. The practical-cell specific energy of the cell was estimated to lie between 50-80 Wh/kg, and 90% capacity retention was reported over 1000 cycles at 4 C. These figures are excellent, and for bulk storage EES considering specific energy, cost/kWh, and rate high rate capability for a high specific energy cell. However, the cell eventually suffered from capacity loss, due to both dissolution of LMO, and most likely, irreversible proton intercalation in the LMO cathode at the low pH. The problem was slightly alleviated by using an unspecified doped form of LMO which managed to retain 95% capacity up to 4000 cycles. With no further recent reports, it remains unclear whether the LMO stability problem in pH 4 electrolyte has been completely resolved. Furthermore, ZnCl₂ solutions are highly acidic and rapidly form complex precipitates at higher pH values [41]. Lastly, the cell would eventually encounter the inevitable growth

of Zn metal dendrites that pose the danger of short circuiting the electrodes. In conclusion the cell is very promising but clearly has some fundamental problems to overcome at the present stage.

2.2.2 Metal-organic framework compound: MIL-53(Fe)·H₂O

Metal–organic framework (MOF) compounds have highly tunable porous structures and are potentially very interesting candidates for Li ion intercalation material. MIL-53(Fe).H₂O (‘MIL’ for Materials of Institut Lavoisier), has a crystal structure of [Fe^{III}(OH)_{0.8}F_{0.2}(O₂CC₆H₄CO₂)]·H₂O (MIL-53(Fe)·H₂O) where channels are formed between the Fe ions linked by the organic group chains (Fig 2.5). The material was tested as an intercalation material for Li-ion batteries by Férey et al., in 2007 [42].

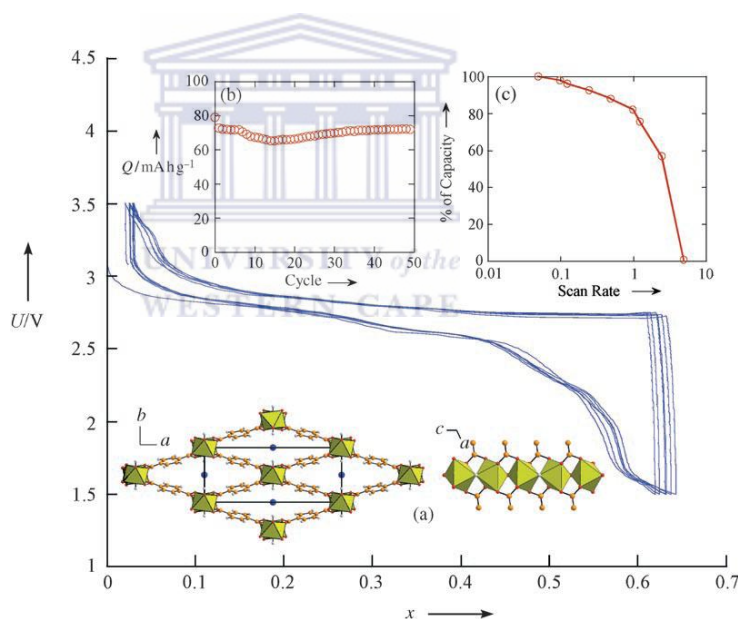


Fig 2.5 Voltage profile for a Li/ MIL-53(Fe)·H₂O half-cell cycled between 1.5 and 3.5 V at a C/40 rate, showing an ideal flat voltage plateau range for an AIB anode [42].

Fig 2.5 shows the cycling voltage curve vs. Li (spanning 3 to 1.5 V), which mostly lies in the ideal range for an aqueous anode (0 to -1.0 V vs SHE or 3 to 2 V vs. Li) and has a flat charge/discharge plateau in this region. The specific capacity of the material was estimated at ~75 mAh/g, which matches some Li-ion intercalation compounds. However, although 50 stable cycles were reported it remains unclear whether it can

sustain long-term cycling. The research on this material as Li-ion battery electrode appeared to stop after this publication, perhaps due to the low specific capacity, which is far from that achieved by Li-ion intercalation in graphite at >300 mAh/g. However, as a possible AIB anode material, it would appear to be worth investigating providing its behavior is repeatable in aqueous electrolyte.

2.2.3 Sulphur: core-shell/polypyrrole

In a very recent study, Jie Shao et al., 2013 [43], demonstrated for the first time that sulphur could be used as an anode in Li_2SO_4 (aq) electrolyte. The proposed charge/discharge reaction of the sulphur in the electrolyte is:

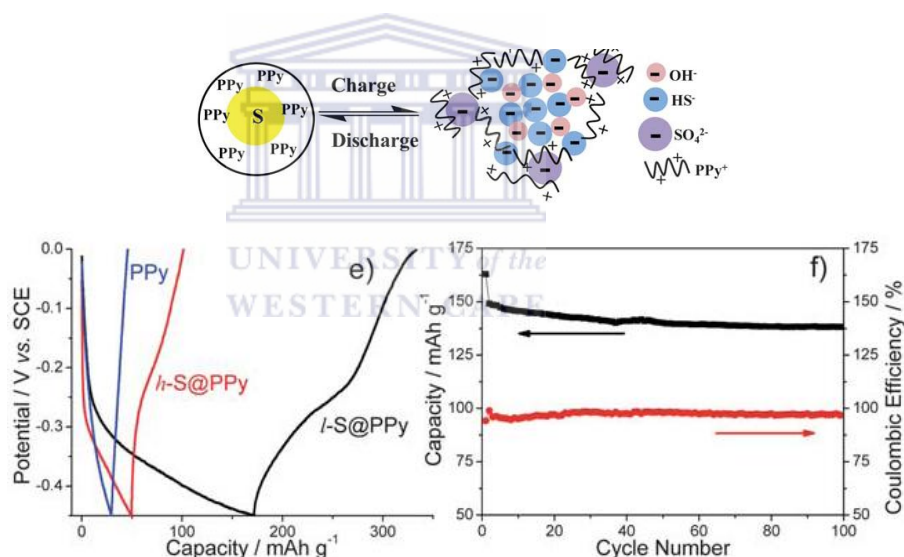


Fig 2.6 Sulphur/polypyrrole as an anode in Li_2SO_4 (aq) electrolyte. Above: charging schematic, below: (left) appropriate AIB anode voltage and (right) 100 stable cycles [43].

The polypyrrole-coated hollow sulphur microparticles (PPy-S) produced a specific capacity 160 mAh/g and had stable capacity retention over 100 charge/discharge cycles (Fig 2.6). Both the high capacity and charge/discharge voltage range of the material are very interesting. However, concerning cost, the use of Ppy may prove expensive for large batteries, and it has yet to be established what rate capabilities the material can withstand or how stable it will be over long-term cycling.

2.3 AC/LMO: a hybrid supercapacitor/battery system

The use of activated carbon (AC) as an anode against an LMO cathode is the only successful example to date of using an alternative anode in AIBs. The idea was first demonstrated by Wang et al., in 2005 [6]. The cell comprised a 2:1 mass loading ratio of AC to LMO on the anode and cathode respectively, and used a 1 M Li_2SO_4 (aq) electrolyte (pH 7) and cycled between 0 – 1.8 V. Fig 2.7 shows the schematic of this cell.

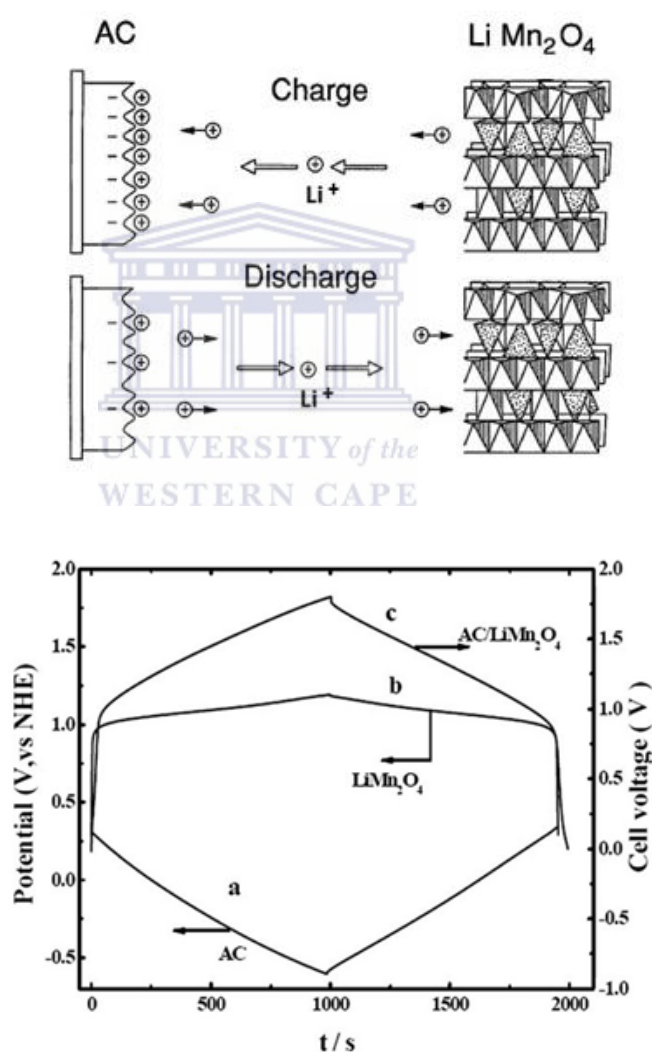


Fig 2.7 Schematic of the AC/LMO hybrid supercapacitor/battery (left), and (right) voltage cycling profile showing the cell voltage and respective voltages of the individual electrodes during charge/discharge [6].

The AC anode stores charge via EDLC (electrochemical double layer capacitance) and therefore constitutes a supercapacitor electrode. In charging, Li^+ forms a double layer on the high surface area carbon which can safely reach a voltage of -0.6 V vs. SHE prior to hydrogen evolution, and is then released back into the electrolyte on discharge to between ~0.0 to 0.4 V vs. SHE. The reported capacitance over this voltage is ~140 F/g, and in terms of capacity: ~40 mAh/g (see equation 5). The overall charge/discharge mechanism preserves the Li^+ concentration of the electrolyte in an analogous fashion to Li-ion batteries.

$$F/g = \frac{Q/g \times 3.6}{\Delta V} \quad (2.7)$$

...where 'F/g' is specific capacitance (F = Farads. 1 F = 1 coulomb/V), 'Q/g' is specific capacity (mAh/g), ' ΔV ' is electrode charge discharge voltage and '3.6' the conversion factor for mAh to coulombs.

The combined specific energy AC/LMO can be calculated using the respective average voltages and specific capacities of each electrode as follows:

AC capacity over 0.0 to -0.6 V vs. SHE = 40 mAh/g

AC average voltage = -0.3 V vs. SHE

LMO capacity over 0.8 to 1.2 V vs. SHE = 80 mAh/g

LMO average voltage = 1.0 V vs. SHE

Cell average voltage = 1.0 + 0.3 = 1.3 V

Balancing mass capacity = 2 : 1 (AC/LMO)

Total material mass 'm' for 'Q' of 80 mAh = 2 g AC + 1 g LMO = 3 g

And, using equation 2:

$$SE = \frac{Q \times V}{m} \quad (2.2)$$

Specific energy 'SE' = 34.7 Wh/kg

Owing to the high stability of AC and LMO in aqueous electrolyte, the cell has excellent cycling stability. Fig 2.8 shows the cell's 95% capacity retention of the cell over 20,000 cycles at 10 C (6 min charge) with close to 100% coulombic efficiency (ratio of charge to discharge capacity). The cell also has much higher specific energy (Wh/kg) than an equivalent AC/AC cell in the same electrolyte Fig 2.8 (right). However, most impressively the cell can be cycled above a 300 C rate (12 sec) and retains 15% of its maximum 1 C specific energy, which in terms of active material mass equals a maximum specific energy of ~35 Wh/kg at 1 C and 5 Wh/kg at >300 C with corresponding specific power of 100 W/kg to 2750 W/kg respectively. In a practical cell, these figures have been estimated to reduce to ~40% [6, 11], and thus become 14 Wh/kg : 40 W/kg (1 C) and 2 Wh/kg : 1100 W/kg.

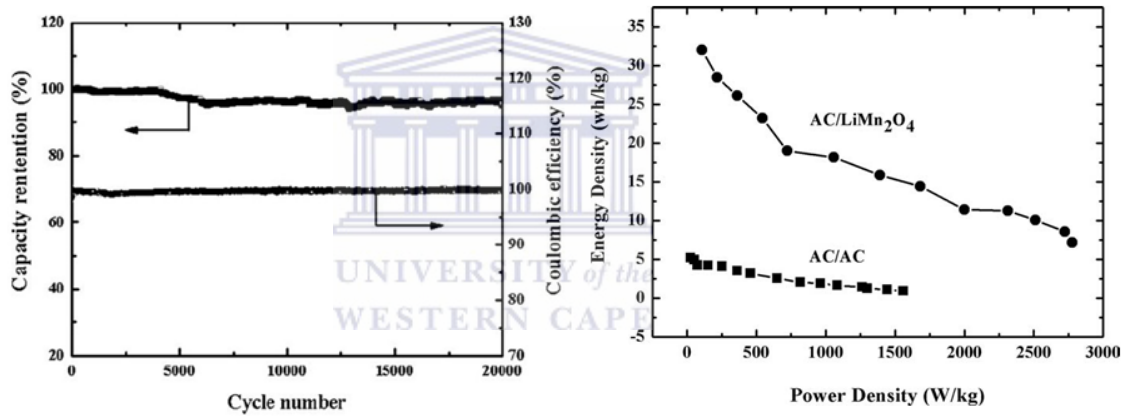


Fig 2.8 Cycling stability AC/LMO (left) and Ragone plot (right) of AC/LMO compared to an AC/AC cell over increasing current density [6].

2.3.1 Possible applications for AC/LMO cells

Fig. 2.9 (below) shows the possible Ragone plot position of a practical AC/LMO cell against other battery types. The theoretical application range extends from both 6 h (0.16 C) EES storage to high power >30 C (<2 min) applications for hybrid vehicles at >1:50 P/E (power/energy ratio) and higher P/E's. Other commercial hybrid batteries are shown on this plot, and the position of AC/LMO would theoretically be the second highest in order of increasing specific power (see below):

- AC/NiOOH: (ESMA© Russia) uses the NiMH battery cathode NiOOH [44, 45],
- AC/PbO₂ : (using the cathode of Pb-acid batteries) made by Axion Power® [46],
- AC/LMO : (using AC anode and LiMn₂O₄ cathode) [6]
- LiC (lithiated graphite anode and AC cathode) made by JSR Micro® [47],

Of the aqueous cell formats, AC/LMO would be the highest in both specific power and energy (not considering ARLB cells that have yet to prove stable, as shown in Fig 2.9, ARLB (1994) [11] , ARLB (2007) [10] and ARLB (2012) [27]). Above AC/LMO, is an organic electrolyte hybrid cell, LiC, which like Li-ion batteries requires costly electrolyte and production facilities. However, to date the AC/LMO cell has not been developed as a high power cell type, rather its use has been adopted in a low power, “low” cost/kWh system for bulk EES application developed by Aquion® (see below).

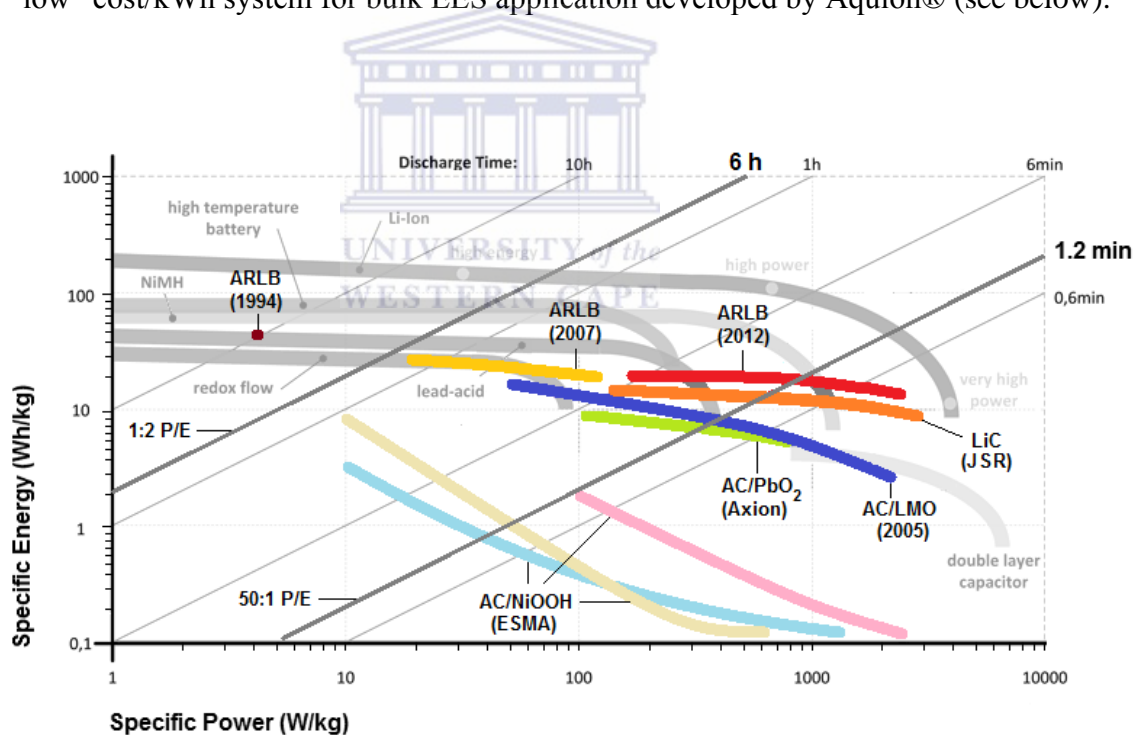


Fig 2.9 Ragone plot of various battery technologies showing the position of AC/LMO and three different ARLB cells after considering a 40% reduction for practical cell values, compiled from [6, 44-48].

2.4 AC/LMO at low power: Aquion®

In the search for a low cost and long-lived battery system for bulk EES, particularly for solar and wind power harvesting, Whitacre et al., in 2011, adopted the AC/LMO cell format in a startup company, Aquion® [4]. This represents the first commercial use of an AIB system. To lower the cost of the cell format, Whitacre et al., substituted the use of Li_2SO_4 (aq) electrolyte for $\sim 15\times$ cheaper and highly abundant Na^+ based electrolyte, Na_2SO_4 (aq). The concept required a Na^+ intercalation cathode host, e.g. NaMnO_2 , which had been previously demonstrated paired against AC in Na_2SO_4 (aq) electrolyte [49]. However, being a larger ion than Li^+ , Na^+ has much higher intercalation resistance and lower specific capacity. On exploring a variety of methods to prepare the Na^+ analogue of LMO, the most stable and high capacity structure came from charging out Li^+ from LMO in Na^+ electrolyte to form the Li^+ vacant cubic spinel structure $\lambda\text{-MnO}_2$. [4, 50] On discharge the Na^+ , being in much higher concentration than the released Li^+ , intercalates into the $\lambda\text{-MnO}_2$ instead. The cathode material yields ~ 80 mAh/g, at full charge/discharge and has a similar value to LMO at 2 C, but slightly lower than the upper limit of LMO at ~ 110 mAh/g, owing perhaps to the greater relative atomic mass of Na^+ . At the higher C rate of 6 C the material shows slightly lower energy retention than LMO most likely due to the higher resistance of Na^+ [4].

Development of the AC/LMO cell into a practical cell format, and into battery systems on the kWh scale has been demonstrated Aquion® Fig 2.10. The cell's electrodes comprise a 1:1 mass ratio of compressed 0.6 mm thick AC electrodes on stainless steel current collectors, and 0.3 mm thick LMO electrodes on either stainless steel or graphite sheet current collectors [4]. The choice of graphite sheet reflects the need to prevent long-term corrosion of the stainless steel cathode current collectors, which is heightened at slow C rates owing to the long periods of charge. Here, the use of thick layering of electrode material to reduce the cost component of current collectors, requires a slow 0.16 C rate charging owing to their high resistance, but is acceptable for 6 h EES applications for solar day length consideration. In this format, the cells reportedly provide a specific energy of 23 Wh/kg and 25 Wh/l. Therefore, as a percentage of the active material specific energy at ~ 35 Wh/kg this represents a high 65% yield, notably

higher than the 40% estimated by Wang et al., 2005, but nevertheless was achieved at the expense of specific power through the use of very thickly layered electrode material.

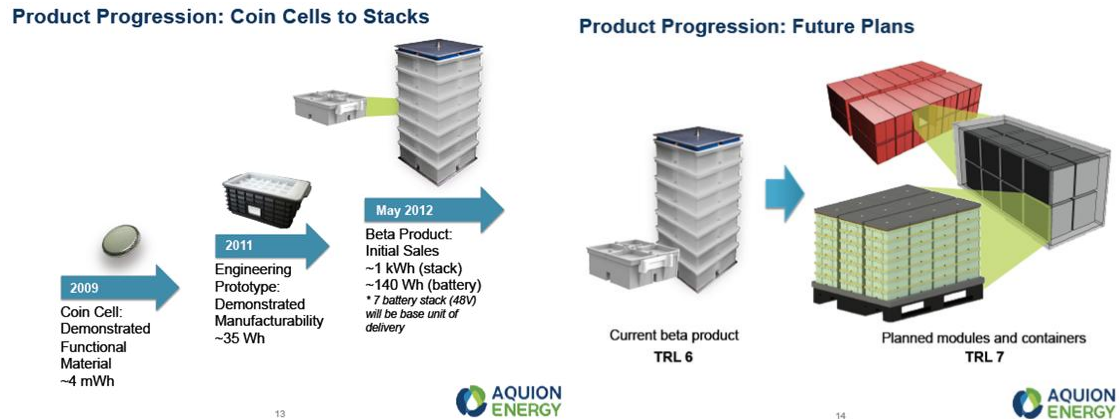


Fig 2.10 First commercial application of an AIB system by Aquion® [4].

At the time of writing, the cost/kWh of the system had yet to be stated. However, regarding a common estimate for bulk LMO purchase at between 5-10 \$/kg and possibly \$10/kg for the required high quality AC, the active material costs can be estimated using the required 2:1 mass ratio of AC/LMO, \$8.3 – 10/kg. At ~35 Wh/kg for active materials, the cost/kWh comes to \$237 – 286/kWh for the active materials alone with a total mass of 28.6 kg. The cost impact for the remaining components without more detailed information, are not possible to predict accurately. However, if the electrode's current collectors were both 304 stainless steel at ~\$2/kg and represented a possible 10% of the total active material mass, an additional cost of $\$2/\text{kg} \times 28.6 \text{ kg} \times 0.1$, coming to \$5.7 adds to the active material costs to make \$242.7 – 291.7/kWh. Therefore, it is highly likely when considering all costs i.e. packaging, electrolyte, tabs, etc., the total cost/kWh comes to over \$300/kWh. However, this is still cheaper than Li-ion batteries at cheapest \$400/kWh, and Pb-acid at \$150/kWh when considering a predicted lifespan of 15 years vs. 5 years.

2.5 AC/LMO at high power

An AC/LMO cell with Li_2SO_4 (aq) electrolyte may have a sufficiently high P/E ratio to be useful in high power applications such as FCEVs (fuel cell electrical vehicles). However, the estimated 40% specific energy reduction for a practical cell (from the active material value) does not consider the effect that the required electrode thickness might have on energy retention at high power. What is known however, is that the Aquion® cell in using Na^+ would have a higher resistance system than one using Li^+ . Therefore the use of Li^+ electrolyte may enable sufficiently higher power in a practical cell e.g. if intermediate thickness electrodes were used.

2.5.1 A battery for long-range FCEVs

If the estimated 40% scale reduction retains similar P/E ratio achieved on thin film electrodes, then high power applications seem definitely possible. Analyses of long-range drive cycles in FCEVs (fuel cell electric vehicles) show that optimal battery efficiency for power assist and regenerative braking comes with a fuel cell to battery power ratio of ~1.4:1 with the battery having a 50:1 P/E [8] (Fig. 2.11). For a 40 kW, 4-seat FCEV this equates to a 28 kW fuel cell and a 20 kW battery with 0.4 kWh storage. Table 2.3 below shows the power durations and energy storage requirements required from such a battery. Fig 2.12 shows the Ragone plot for an AC/LMO cell Li_2SO_4 (aq) with 40% practical cell reduction and the position of the 50:1 P/E line.

The point of intersection on the AC/LMO of the 50:1 P/E line gives a cell of ~8 Wh/kg and 400 W/kg. Therefore, for a 20 kW/0.4 kWh battery for the FCEV mentioned above, an AC/LMO battery would weigh 50 kg. When compared to other battery technologies along the 50:1 P/E line (Fig 2.10), the trend going up the line culminates in the lightest technology being Li-ion at 8 kg for a 20 kW/0.4 kWh battery. However, in terms of cost such high P/E ratio in Li-ion batteries becomes expensive, as shown in Fig. 2.13. Here, the required extrapolation to 50:1 P/E results in a battery cost of \$981 for 0.4 kWh.

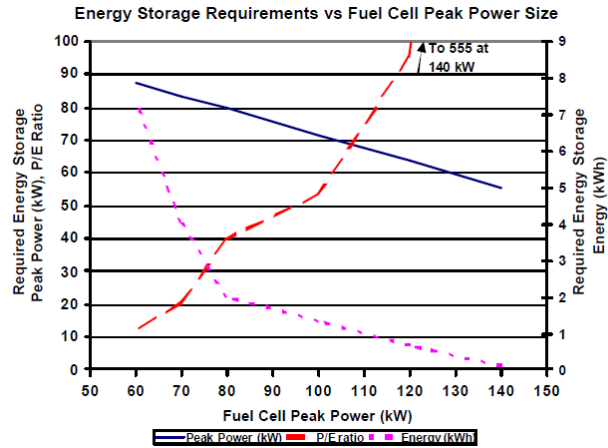


Fig 2.11 Example of the 1.4:1 fuel cell/battery power ratio, and 50:1 battery P/E ratio, for a long-range drive-cycle FCEV from [8].

Event description	Peak Power (kW)	Duration (s)	Cumulative energy (kWh)
Start up:	10	10	0.045
Power-assist:	20	3	0.024
Acceleration:	11	20	0.066
Accessory loads:	0.4	10-45 min	0.03
Regenerative braking:	20	30	0.17

Car power max. 40 kW: Fuel cell max. 28 kW, battery max. 20 kW with 0.4 kWh, adapted from [8]

Table 2.3 Battery power and energy requirements for FCEV 4-seat (40 kW) car, adapted from [8]

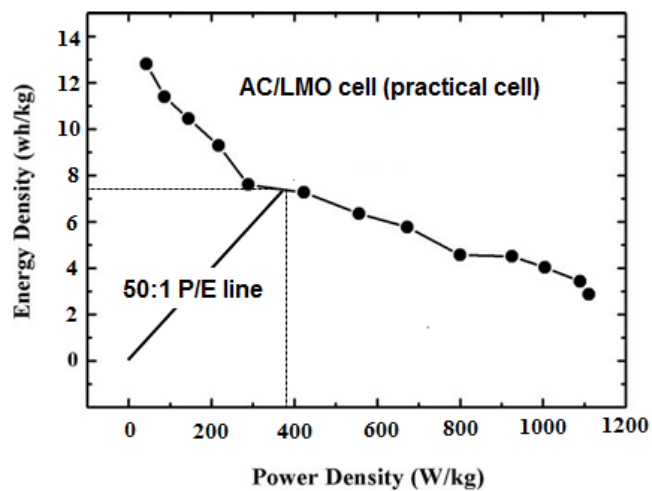


Fig 2.12 Ragone plot of AC/LMO cell with 40% practical cell reduction, showing 50:1 P/E ratio, adapted from [6]

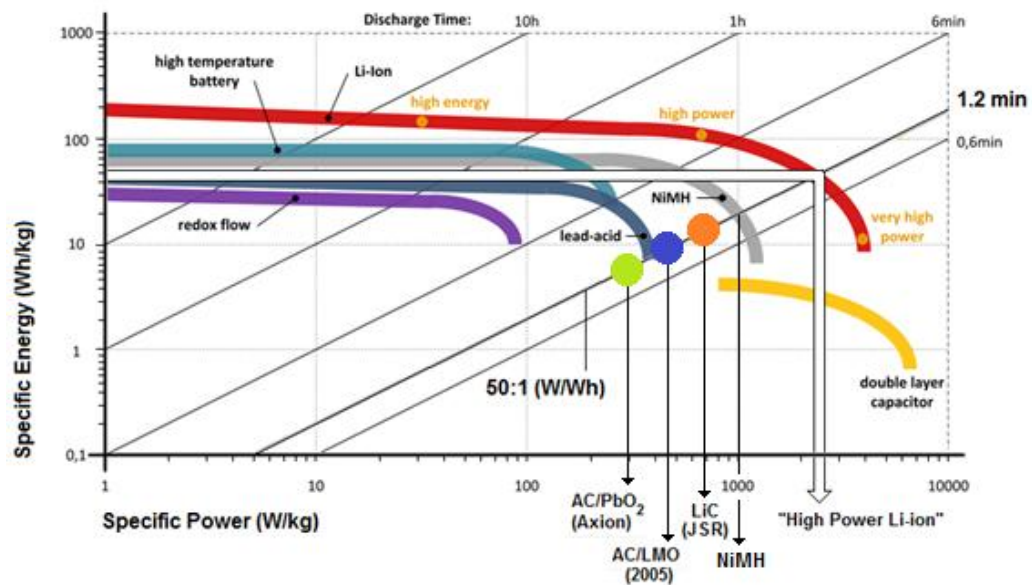


Fig 2.13 Ragone plot of battery technologies intersecting the 50:1 P/E ratio line, showing the possible position of a practical AC/LMO cell adapted from [6, 44-48]

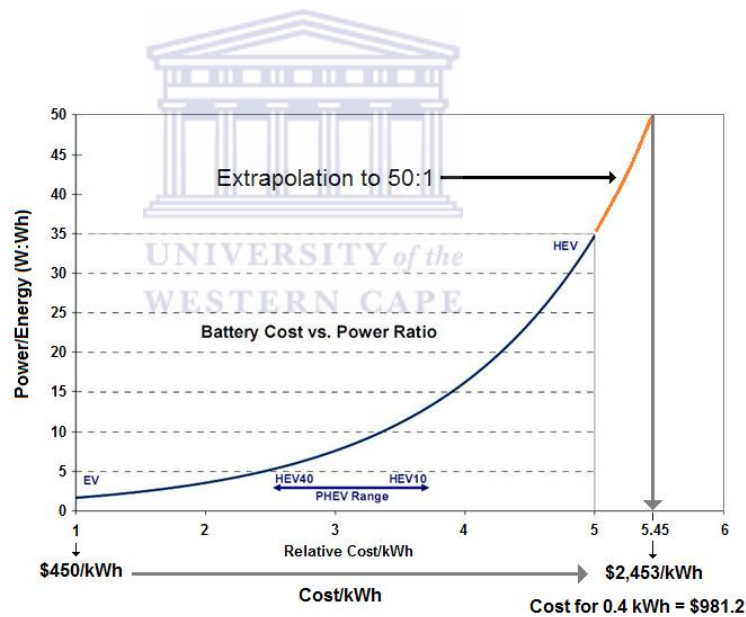


Fig 2.14 Cost of Li-ion battery at 50:1 W/Wh ratio. Graph shows extrapolation to 50:1 ratio, adapted from [51]

The high cost of the Li-ion battery arises from the factor of 5.45 reduction in specific energy density at 50:1 P/E. And, the same can be seen with NiMH by the rapid down turn curve of its Ragone plot at 50:1 P/E Fig 2.13. Sourcing the cost of the hybrid technologies, Axion® and LiC®, for this application was not possible to calculate owing to limited available information on the systems. The possible cost of an AC/LMO for the 0.4 kWh, 50:1 P/E battery can be estimated at \$393. This calculation

is based on the \$982.5/kWh figure calculated in Section 2.5.2 (below), and places the AC/LMO at more than $2 \times$ cheaper than a Li-ion battery used for the same high power purpose, with possibly higher lifespan (owing to AC stability), and safer operation owing to the use of benign Li_2SO_4 (aq) electrolyte. The AC/LMO cell would however be approximately $6 \times$ heavier at 50 kg as opposed 8 kg for the Li-ion battery.

2.5.2 Considerations for a high power practical AC/LMO cell

Without exact knowledge of the complete mass and cost contribution of all the components that combine to make a practical AIB cell, the isolated values of active material specific energy and power are only academic. A 40% reduction of active material properties (e.g. specific energy and power) has been suggested [6, 11], but this cannot predict how electrodes will behave using thick layers of electrode material. Whitacre et al., found that very thick AC/LMO electrodes can provide practical cells of 65% of the active material value albeit at great expense of specific power [4]. Here, it can be assumed that if higher power cells were required the electrode material thickness would need to be reduced.

Table 2.4 (below, overleaf) shows that the active materials AC and LMO in thin film used by Wang et al., represented only 18% of a practical cell's total mass i.e. resulting in only 6.3 Wh/kg at maximum, and 3.6 Wh/kg at 50:1 P/E. Clearly, this is much lower than the 40% estimate. To calculate how much active material ($0.773 x$) (re. Table 2.4) would be required to represent 40% of the total cell mass requires the following equation:

$$0.773x = 0.4(130 + x) \quad (2.8)$$

Where 0.773 is the fraction of active materials in electrode film (Table 2.4), ' x ' is the total mass of electrode film, and 130 mg is the combined mass of two current collectors and one separator.

$$x = 139.4 \text{ mg electrode material}$$

$$0.773 x = 107.8 \text{ mg AC + LMO}$$

The value corresponds to $\sim 3.5 \times$ the mass of active material actually used on the current collectors in the Wang et al., experiment (Table 2.6). This would also mean that the electrode material would have to be $\sim 3.5 \times$ thicker than in the experiment to achieve the stated 40%.

Electrode film	Mass (mg)	Mass (%)
Active material	85	77.3
Carbon black	10	9.1
PTFE	5	4.5
Electrolyte	10	9.1
Total	110	100

As used by Wang et., al [6], 18% active material cell		
1 cm ² electrodes	Mass (mg)	Active material. (%)
LMO	10.2	6.0
Carbon black	1.2	
PTFE	0.6	
Current collector 1	60	
AC	20.4	12.0
Carbon black	2.4	
PTFE	1.2	
Current collector 2	60	
Electrolyte	3.6	
Separator	10	
Total	169.6	18

Table 2.4 Considering mass contributions of cell components on thin film electrodes. Above: components of electrode film, and below, the thin film cell tested by Wang et al., 2005.

To establish an approximate idea of how much the 40%-corrected AC/LMO cell might cost/kWh, some estimations can now be made regarding the above material quantities. Table 2.5 shows the cost calculations for the 40% active material mass cell at P/E 2:1 and 50:1 (High power); the calculations do not include connection tabs, cell packaging or preparation solvents etc., and used common estimates for material cost/kg in bulk supply. The predicted cost of the cell at P/E 50:1 ratio is \$996.25/kWh. Compared to Li-ion batteries at P/E 50:1 at \$2453/kWh, this is $\sim 2.5 \times$ cheaper (Section 2.5.1 re. Fig 2.14).

Material	Cost/kg	Cell mass (mg)	Mass %	\$/1kg cell	% cost	14 Wh/kg P/E 2.1 (\$/kWh)	8 Wh/kg P/E 50:1 (\$/kWh)
LMO	10	35.7	13.3	1.33	16.7		
AC	15	71.4	26.7	4.00	50.2		
Carbon black	5	9.7	3.7	0.18	2.3		
PTFE	5	4.9	1.9	0.10	1.3		
Li ₂ SO ₄	5	9.7(aq)	3.7(aq)				
		1.0 (s)	0.4 (s)	0.02	0.25		
Stainless steel	5	120	45.9	2.30	28.9		
Separator (cotton)	1	10	3.8	0.04	0.5		
Totals		261.4	100	7.97	100	569.29	996.25

Table 2.5 Cost calculations for a 40% active material mass cell at P/E 2:1 and P/E 50:1

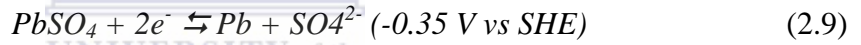
The table also shows that AC is by far the most expensive component of the cell both concerning its cost/kg and quantity required owing to its low specific capacity of 40 mAh/g. In the Aquion® cell, recognising this, Whitacre et al., [4] have introduced a lower cost carbon source, glucose, as precursor for an AC production target of <\$10/kg. Furthermore, it of interest to note that the percentage cost of Li₂SO₄ is so low in the above cell, that changing the electrolyte to Na₂SO₄ at ~15× lower cost/kg, makes little difference to the overall cost of the cell. Moreover, the use of Na⁺ may even increase the cost of the cell particularly where high specific power is required, owing to its far greater intercalation resistance.

2.6 A Pb anode for low cost/kWh

The limited specific capacity of AC of only 40 mAh/g and its high cost/kg (\$15/kg) are detracting features for its use in large EES batteries. Much higher capacity anodes exist in other aqueous battery systems, as were examined in Section 2.2. Nevertheless, not many are suited to operation in benign pH 7, 1 M Li₂SO₄ (aq), electrolyte, which would be required for use with an LMO cathode. However, while no published studies appear to exist on the subject, the use of Pb as an anode at pH 7 in 1 M Li₂SO₄ (aq) electrolyte might offer the same function as it does in Pb-acid batteries in H₂SO₄ electrolyte.

2.6.1 Pb/PbSO₄: electrochemical behaviour

At ~\$150/kWh, Pb-acid batteries provide the lowest cost/kWh storage of all rechargeable batteries [2]. The anode of Pb-acid batteries is essentially Pb metal, which undergoes chemical conversion to PbSO₄ in the discharge reaction of the battery.



The theoretical specific capacity of PbSO₄ is 174 mAh/g, and in practice over 100 mAh/g can be obtained from the material in Pb-acid batteries [17]. Here the essential electrolyte component for the reaction is the SO₄²⁻ ion, which exists in both H₂SO₄ (aq) and 1 M Li₂SO₄ (aq) electrolyte. Cyclic voltammetry studies on Pb metal in 1 M Na₂SO₄ [40] have shown that reversible redox peaks for the Pb/PbSO₄ reaction occur at similar potentials in H₂SO₄ [52], at -0.35 V vs. SHE (Fig 2.15). The Pourbaix diagram of Pb also suggests that below pH 8 the electrode reaction will proceed entirely between Pb and PbSO₄, with PbO formation only occurring far into the alkali region [53]. Therefore, the above evidence combined suggests that Pb could provide a functional anode in pH 7 sulphate salt-based electrolytes.

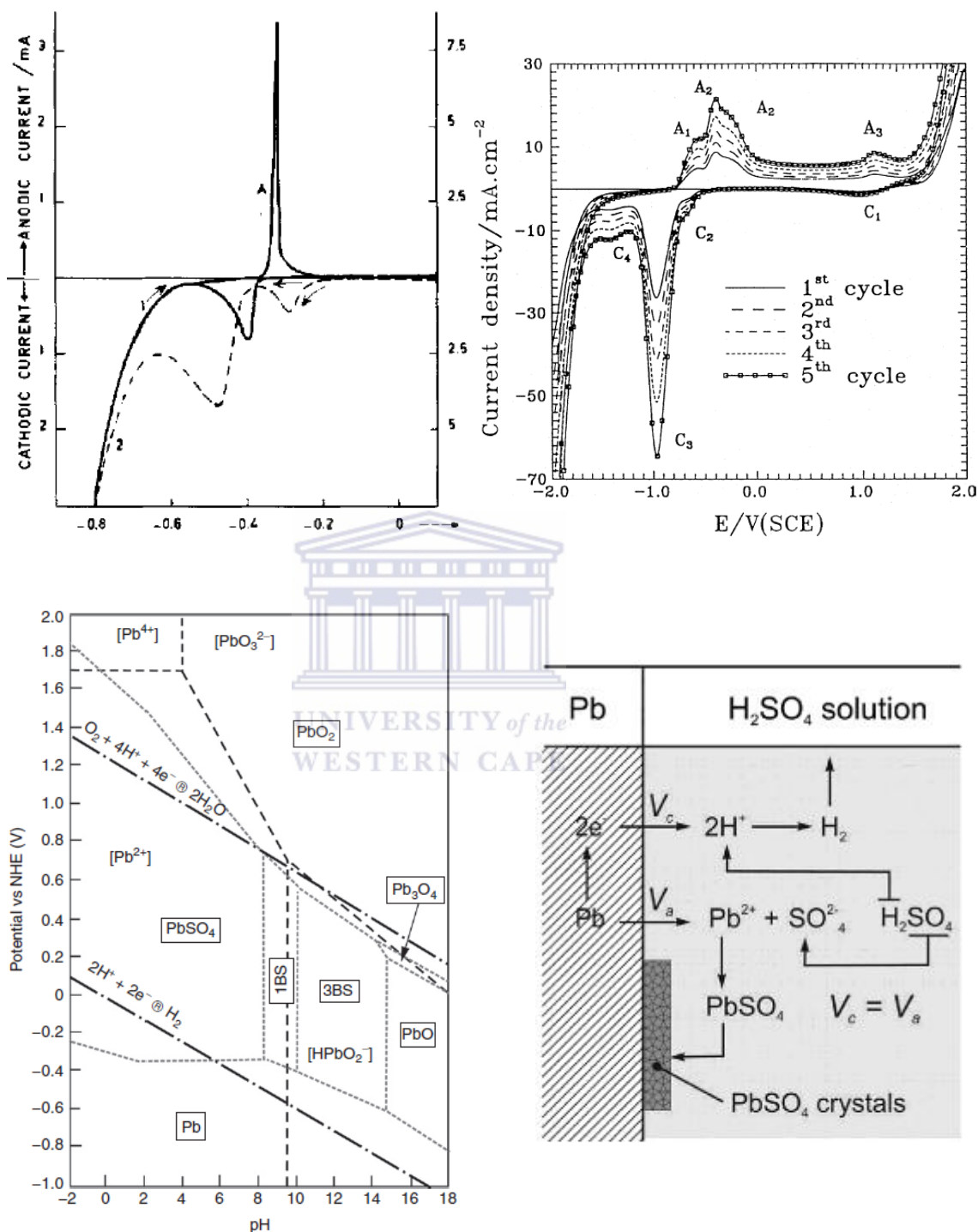
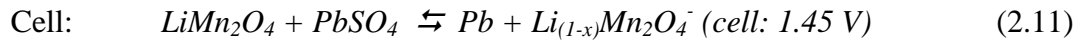
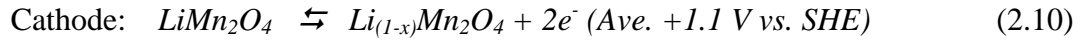
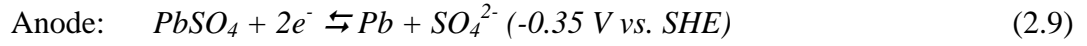


Fig 2.15 Cyclic voltammetry of Pb metal in H_2SO_4 (top left) [52] and Na_2SO_4 (aq) (top right) [40] show corresponding cathodic peaks relating to Pb/ PbO_4 conversion (-0.35 V vs. SHE). Below: Pourbaix diagram of Pb (left) and schematic of Pb charge/discharge (right) [53].

2.6.2 A theoretical PbSO₄/LMO cell

If a cell was to be made comprising a PbSO₄ anode and an LMO cathode in 1 M Li₂SO₄(aq) electrolyte, a charge/discharge voltage profile and active material specific energy can be predicted as follows:



Here, the theoretical average 1.45 V cell voltage is already higher than that of AC at 1.3 V (Section 2.3). Next, assuming a specific capacity of 100 mAh/g is accessible from both materials [2, 6], the following active material specific energy could be obtained from equal mass loadings of the material on current collectors:

$$\text{SE} = \frac{100 \times 1.4}{2} = 70 \text{ Wh/kg} \quad (2.1)$$

And, if a practical cell could retain 65% of active material specific energy using thick electrodes for an EES bulk storage device (re. Aquion®, Section 2.4) a practical specific energy of 45.5 Wh/kg might be obtainable, which is comparable to Pb-acid batteries [2] despite the fact Pb-acid batteries have a higher cell voltage of 2.1 V. Furthermore, the value is almost double the specific energy of Aquion® AC/LMO cells at ~23 Wh/kg.

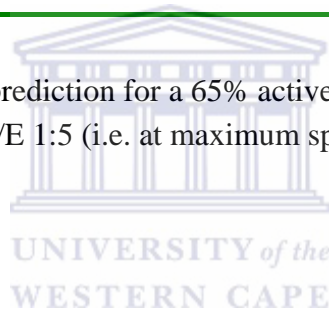
2.6.3 Estimated cost/kWh of a PbSO₄/LMO cell

A prediction of material cost/kWh can be made using the approach outlined Section 2.5. The following calculations were made assuming the same electrode additive components of active materials, carbon black conductive material, PTFE binder and electrolyte at 77.3:10:5: mass percentage (Table 2.6). A very low cost \$115.6/kWh can be realized assuming 65% of the active material's specific energy value can be accessed. This cost is lower than Pb-acid batteries at \$150/kWh, but does not include

other cost such as packaging, tabs, other production-related costs and profit margins etc. Therefore, a modest estimate would be that the cost is similar.

Material	Cost/kg	Cell mass (mg)	Mass %	\$/1kg cell	% cost	45.5 Wh/kg P/E 1:5 (\$/kWh)
LMO	10	265.5	32.5	3.25	61.8	71.44
PbSO ₄	2	265.5	32.5	0.65	12.4	14.33
Carbon black	5	62.5	7.6	0.38	7.2	8.32
PTFE	5	30.9	3.8	0.19	3.6	4.16
Li ₂ SO ₄	5	62.5 (aq) 6.3 (s)	7.6 (aq) 0.76 (s)	0.04	0.8	0.92
Stainless steel	5	120	14.7	0.74	14.1	16.30
Separator (cotton)	1	10	1.2	0.01	0.2	0.23
Totals		817	100	5.26	100	115.60

Table 2.6 Cost/kWh prediction for a 65% active material mass PbSO₄/LMO cell at P/E 1:5 (i.e. at maximum specific energy)



$$0.773x = 0.65(130 + x) \quad (2.7)$$

Where 0.773 is the fraction of active materials in electrode film (Table 2.4), 'x' is the total mass of electrode film, and 130 mg is the combined mass of two current collectors and one separator.

$$x = \text{mg electrode material}$$

$$0.773 x = \text{mg PbSO}_4 + \text{LMO}$$

2.6.4 Possible advantages of a PbSO₄/LMO cell

Assuming a PbSO₄/LMO cell might cost the same as a Pb-acid battery (Table 2.8), it could also offer the following advantages:

- As ~32.5% of the PbSO₄/LMO cell mass, PbSO₄ has a total Pb content in the cell of 22.2%. For the same cost/kWh and specific energy, Pb-acid batteries contain a total Pb content of 60% of the cell mass [17]. This means that the PbSO₄/LMO cell would facilitate $\sim 2.7 \times$ more efficient use of Pb than Pb-acid cells. The reason for this difference is that Pb-acid cells use heavy Pb metal current collectors that do not participate in charge storage.
- Having one LMO ion-intercalation electrode, a PbSO₄/LMO cell would have lower resistance to charge transfer than two chemical conversion electrodes as found in Pb-acid cells. The cell may therefore have faster charge/discharge speeds
- The use of benign pH 7 aqueous salt electrolyte has obvious safety benefits over using concentrated sulphuric acid.
- Lower possibility of hydrogen evolution on the Pb anode at pH 7.

Regarding recycling, the Pb electrode could be recycled in the same way as Pb acid battery electrodes. The LMO electrodes of longer lifespan could be retained in the cell and the Pb anodes removed. Here, the stainless steel current collectors of the Pb anode after having the spent PbSO₄ removed could possibly be cleaned and reused.

Chapter 3

Methodology

3.1 Experimental techniques and instrumentation

3.1.1 Material preparation and characterization

3.1.1.1 Electrode film preparation

Electrode films, when sufficient active material was available, were made from 1 g quantities of electrode dough. To prepare the electrode dough, 0.85 g of active material powder was dry-mixed in a beaker with 0.1 g carbon black (SuperP-Li® Timcal) and 0.05 g PTFE (0.083 g 60% wt/wt aqueous suspension: Teflon® 30-N, Dupont). Isopropanol (~0.5 ml) was added to the mix and stirred with a spatula to form a pliable dough. The dough was hand-rolled out and re-compressed into a tight “swiss roll” five times on a glass pan using a 2.5 cm diameter swagelock pipe, with frequent addition of isopropanol drops to the dough to prevent loss of pliability. To obtain a consistent desired thickness of film, e.g. 0.25 mm, the rolled dough was fed into rolling press (MTI© model MSK-HRP-MR100B) set to measure. The films were dried in an oven at 100°C for at least 2 h to evaporate isopropanol and any volatile surfactants in the PTFE solution. Finally, a required mass of film was cut and weighed before pressing into nickel 80-mesh or 304 stainless steel 80-mesh (Alfa Aesar) current collectors at 12 MPa (~120 kg/cm²) for 10 sec.

3.1.1.2 Morphological analysis by SEM and TEM, and elemental analysis by EDS

Scanning electron microscopy (SEM) provides a means to view the surface morphology of material at up to 500,000 × magnification. The technique requires the surface of the material under examination to be electrical conductive. In the case of poorly conductive materials such as PbSO₄ used in this study, the particles were splutter coated with gold. All micrographs were taken at the UWC Physics department using a ‘Zeiss Gemini Auriga field emission microscope’. Transmission electron microscopy (TEM) and high resolution transmission electron microscopy (HRTEM) allows a deeper structural

analysis and crystal lattice detection to be made via penetration of electrons through the particle structure. All micrographs were taken at the UWC Physics department using a state of the art high powered ‘Tenai G² F20 X-twin MAT 200 kV Field Microscope’. Energy dispersive X-ray spectroscopy (EDS) allows elemental analysis of material, via detection of emitted X-rays from the movement of electrons between orbitals. Spectra were obtained from samples analysed on the ‘Zeiss Gemini Auriga field emission microscope’.

3.1.1.3 X-ray diffraction (XRD) analysis

XRD crystal structure identification and analysis of prepared samples was carried using a ‘Bruker D8 Powder Diffractometer’ (Ithemba labs, Cape Town, South Africa) with a theta-theta goniometer using Cu K α radiation operated at 40 kV and 35 mA at room temperature.

3.1.2 Electrochemical characterization

3.1.2.1 Cyclic voltammetry (CV)

CV provides a means to determine the current response to imposed voltages on electrode materials. In the present study, redox peaks relating to charge and discharge mechanisms were of interest and provided a guideline for material suitability for use as either battery anodes or cathodes. CV was not used to determine the specific capacity or capacitance of material, as the direct response to actual battery cycling conditions at constant current were of greater concern. CV was carried on electrode films (as prepared above 3.1.1.1) using an SCE (saturated calomel electrode) reference electrode and activated carbon (AC) films as a counter electrode, using an ‘Autolab electrochemical work station’ (PGSTAT128N, Eco Chemie, The Netherlands). All CV analyses were carried out in open cell format at room temperature.

3.1.3 Galvanic cycling

3.1.3.1 Battery test cycling machinery

Galvanic cycling of cells at constant current was carried on four different sized battery testers according to the required current or size of the cell. For a current range of 0.01 to 1.0 mA, e.g. used on 10 mg PbSO_4 films, an 8-channel LAND (5 V, 1 mA CT2001, China) battery tester was used. Cycling of high power AC/LMO cells, requiring between 1 – 10 mA, or 10 – 100 mA, 1 – 20 A (for an up-scaled 1 Ah AC/LMO cell) was carried out on three accordingly sized 8-channel NEWARE® (5 V, China) cycling machines.

3.1.3.2 Individual electrode voltage analysis

To monitor the voltage on individual electrodes with respect to an SCE reference electrode during constant current charge/discharge cycling, up to three separate channels of the battery cycling machine were used independently to monitor the anode, cathode and cell voltage respectively (Fig 3.1).

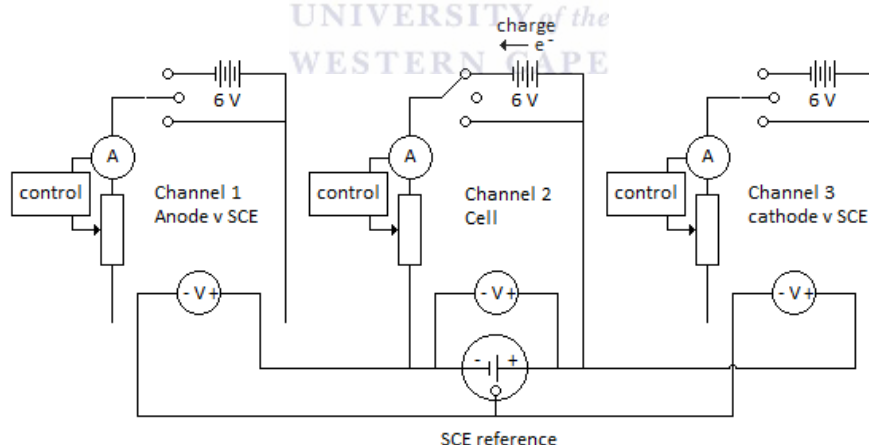


Fig. 3.1 Schematic of three-channel cycle testing. Channel 1 measures the voltage of the anode v SCE reference electrode; channel 2 cycles the cell and measures cell voltage; and channel 3 measures the cathode voltage v SCE.

Chapter 4

High power AC/LMO cell development

4.1 Introduction

Section 2.5 of this thesis considers the possibility that a high power AC/LMO cell might offer ~40% of the specific energy and specific power of its active materials. Such a cell would deliver ~400 W/kg at ~8 Wh/kg (P/E 50:1) and be of interest in high power applications, e.g. as a battery for FCEV (fuel cell electric vehicles), (Section 2.5.1). The roughly estimated material cost/kWh of the AC/LMO battery is $> 2 \times$ cheaper than high power Li-ion batteries, but the battery would be $\sim 6 \times$ heavier and larger. In the 4-seater FCEV example, a 0.4 kWh 50 kg AC/LMO battery would be much heavier than a 0.4 kWh 8 kg Li-ion battery. However, as a small fraction of the car's total mass, and considering passenger weight variations, the difference is probably less dramatic regarding fuel consumption and worth consideration regarding its potentially much lower cost.

Considering the above possibilities, the following studies investigate whether the AC/LMO cell in practical cell format could supply the above target figures. In the literature, studies of AIB electrode materials rarely extend their analyses beyond that of the specific energy of the active material mass tested as thin film electrodes. However, in practical cells, the specific energy of such thin films would be drastically reduced by the high mass component of current collectors. As a rough estimate based on the thin-film cell format used by Wang et al., the inclusion of current collector mass would reduce the active material specific energy to $< 20\%$ in a practical cell. Section 2.5 calculated a practical cell would require $\sim 3.5 \times$ thicker electrode material film on current collectors to achieve the estimated 40% reduction of specific energy and specific power of AC/LMO active materials.

However, it is well known that increase in electrode material thickness increases electrode resistance by lengthening paths of electron and ion movement [54, 55]. These factors ultimately determine how much specific energy and specific power an electrode material combination can supply. Therefore, tests on thicker films are clearly essential for determining an electrode material's true value for practical applications.

One possible reason for why tests on thicker film electrodes are not regularly carried out is the apparent lack of a convenient test method. Thin electrode films can be easily prepared, pressed into metal mesh current collectors, and quickly tested in open glass vials of electrolyte. On the other hand studies on thicker films require a few more steps. The first of these being a calculation on how much film per cm^2 of current collector would be needed to produce a target specific energy in a practical cell. Secondly, a means of reliably producing an even thickness of thick electrode film is required, and thirdly an appropriate cell is required to test the thicker form of electrode. Section 4.3 of this Chapter explored these requirements and constructs a custom-designed cell for studying the effects of electrode thickness. Prior to this are characterizations of the AC and LMO active materials (Section 4.2) and lastly an up-scaled high power 1 Ah cell is constructed and tested in Section 4.4.

4.2 Basic properties & cycling performance of AC & LMO

The first aim of the study was to characterize the electrochemical properties and galvanic cycling performance of the active materials AC and LMO (Section 4.2.1.1, below). The study by Wang et al. [6] provided target figures of merit, namely the specific energy and specific power values achievable from the thin-film electrode format. These derive from the active materials' specific capacity, voltage and rate capability. In the present study, cyclic voltammetry was used to examine the potentials of electrode activity on AC and LMO. This was followed by galvanic cycling of the electrodes to determine their specific capacity and rate capability. To provide a more detailed examination of cell performance, individual electrode potentials were also monitored during cycling using an SCE reference electrode. All studies were carried out

on thin-film electrodes of loading density between 10 to 40 mg/cm² of electrode film on 80 mesh nickel or stainless steel 304 current collectors. The electrode films comprised 85:10:5 (active material, carbon black, PTFE) mass percentage and all tests were carried out in 1 M Li₂SO₄ (aq) electrolyte according as outlined below. Finally, conclusions are made concerning the performance of the materials and their comparison to those used by Wang et al.

4.2.1 Experimental

4.2.1.1 Active materials, SEM, and electrode film preparation

Commercially available active materials AC (coconut-based YP-50F (YP-17) Kuraray Chemical Co., Ltd) and LMO (“High power” LM021-HK, Shanshan Tech.) were used in this study. AC and LMO were examined by SEM using a (Fig 4.1) to their determine particle size range. Electrode films contained 85:10:5 (active material, carbon black and PTFE) mass percentage (Chapter 3, Section 3.1.1.1).

4.2.1.2 Cyclic voltammetry (CV) and Galvanic cycling

CV was carried out in an open three-electrode cell (Fig 4.1). The cell comprised: a working electrode of 10-mg AC or LMO electrode film covering a 1 cm² area of 304 stainless steel mesh current collector in pH 6 (as prepared) 1 M Li₂SO₄ (aq) solution; an auxiliary electrode of 200 mg AC electrode film covering ~4 cm² of current collector; and a saturated KCl ‘calomel’ (SCE) reference electrode. Thin film AC and LMO electrodes (20 and 10 mg of film respectively) were cycled in 1 M Li₂SO₄ (aq) electrolyte using a ‘Neware (5 V, 0.1 – 10 mA range)’ battery cycler. All cycling experiments used constant current with a 0 – 1.8 V cell charge/discharge voltage range set according to Wang et al., 2005 [6].

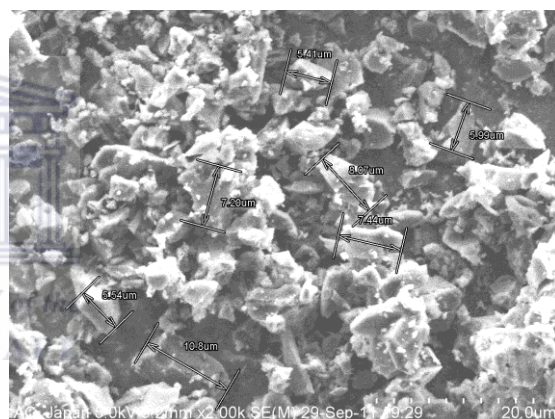
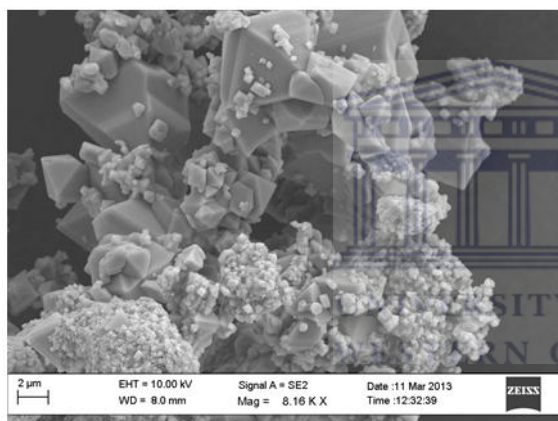


Fig 4.1 Photograph of the three-electrode cell (top) showing 1 cm² area of working electrode on the left side of vial, SCE reference electrode in the middle and large auxiliary electrode on right side of the vial. Below are SEM images of commercial LMO (left) and AC (right) used in this study, showing wide particle size range between ~0.1 to 10 μm.

4.2.2 Cyclic voltammetry on LMO and AC electrodes

Cyclic voltammetry (CV) was used to determine the potentials of Li^+ intercalation in LMO and the EDLC (electrochemical double layer capacitance) behaviour of Li^+ on AC. Wang et al. used an in-house synthesized LMO and a commercially available phenol resin derived AC. In combination these provided a stable cell voltage of 1.8 V at various current densities of charge. The potentials of the LMO and AC at full charge were +1.2 and -0.6 V vs. SHE respectively, where neither material produced oxygen or hydrogen evolution respectively at these potentials.

4.2.2.1 Results and discussion

Fig 4.2 shows the CV scan of a 1 cm^2 10-mg LMO film electrode cycled at 5 mV/sec between +0.2 and +1.6 V vs. SHE. A pair of redox peaks +1.0 and +1.2 V vs. SHE are present on the anodic scan which indicate the double phase nature of Li^+ de-intercalation. In the cathodic scan the two peaks reappear at +1.1 and +0.9 V vs. SHE, showing the reaction is reversible.

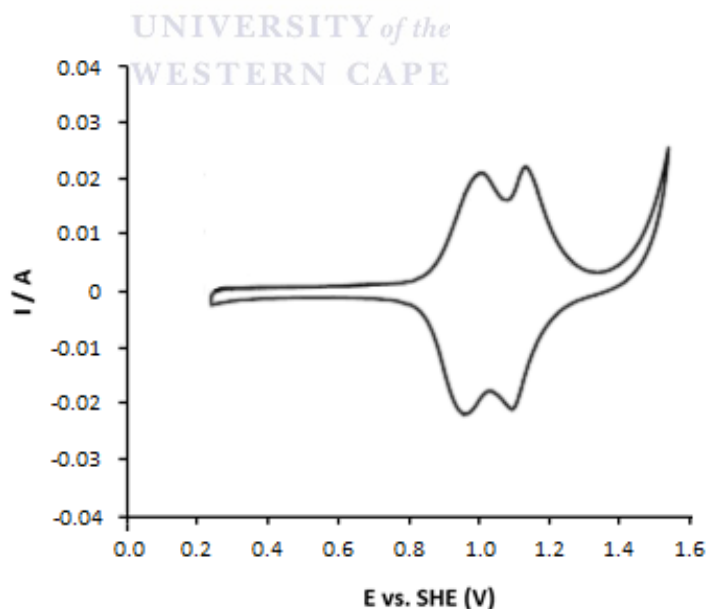


Fig 4.2 Cyclic voltammetry of a 1 cm^2 10 mg LMO film electrode at a scan rate 5 mV/sec. In anodic scan (analogous to charging) the double peaks of Li^+ intercalation at +1.0 and +1.2 V vs. SHE occur prior to onset of oxygen evolution at +1.35 V.

The double peaks relate to resistance differences in Li^+ intercalation at the surface and interior of the crystal spinel structure and are commonly observed in both organic electrolyte Li-ion batteries and ARLBs [6, 56]. Importantly, the results also show insignificant current response related to oxygen evolution until about +1.35 V which is safely beyond the higher voltage peak of Li^+ de-intercalation (charging).

Fig 4.3 shows the CV plot of a 1 cm^2 10-mg AC film electrode cycled at 5 mV/sec between -0.9 and +0.5 V vs. SHE. The scan has the characteristic square shape of EDLC (electrochemical double layer capacitance) capacitance, where Li^+ ions adsorb within the pores of AC on the cathodic scan (equivalent to charging in an AC/LMO cell) and are released on the anodic scan (re. discharge in AC/LMO cells). In the cathodic scan, hydrogen evolution begins to increase dramatically from -0.75 V vs. SHE toward the more negative direction. In the anodic scan direction onset of oxygen evolution appear to begin prior to +0.5 V vs. SHE, or an alternative explanation is that absorbed hydrogen is reduced back to protons at this potential [57]. However, within the

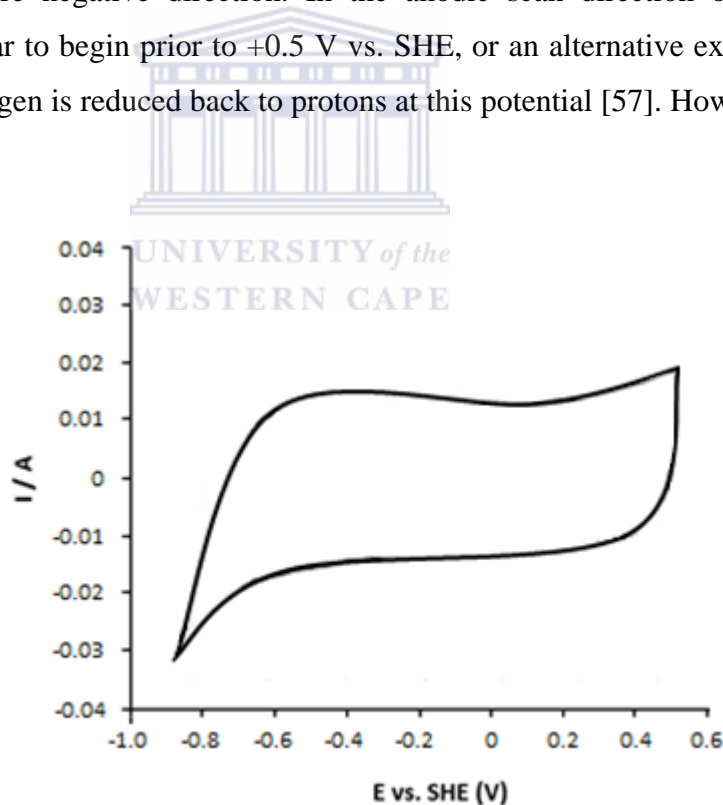


Fig 4.3 Cyclic voltammetry of a 1 cm^2 10 mg AC film electrode at a scan rate 5 mV/sec. The plot has the characteristic shape of EDLC with onset of hydrogen evolution occurring at ~ -0.75 V vs. SHE in the cathodic scan direction.

potential range of interest for the AC anode, the region of between -0.65 and 0.2 V vs. SHE appear as stable reversible capacitance plateaus. Therefore, within the safe voltage window of the electrolyte, combining the most positive LMO cathode potential of +1.2 V vs. SHE with the most negative AC potential of ~0.6 V vs. SHE gives a maximum cell voltage of 1.8 V.

4.2.3 Galvanic cycling of thin-film AC and LMO electrodes

The following galvanic cycling experiments aimed to determine the specific capacity and rate capability of the AC and LMO active materials in thin film electrode format. Achieving optimal specific energy and specific power, requires that cells should have electrodes with the correct mass ratio of active materials. These can only be determined experimentally and are determined by charging voltage and current density. Therefore, the following studies examined the relationship between these factors on the individual electrodes and then combined as cells.

4.2.3.1 Consideration of specific capacity, charging voltage and current density

The maximum specific energy in the thin film format reported by Wang et al. was 32 Wh/kg. The electrodes had a 2:1 mass ratio of AC and LMO (in ~20 and 10 mg thin films respectively) and were cycled at 200 mA/g of active material. This information allows the current density on each electrode's active material content to be calculated. In the 2:1 mass ratio of active materials, AC and LMO have 66.6% and 33.3% of the combined mass respectively. Therefore, the current density on AC and LMO were 300 mA/g ($200/0.6$) and 600 mA/g ($200/0.3$) respectively.

In order to appreciate how the value of 32 Wh/kg arises from the above experiment, the schematic in Fig 4.4 shows the relationship of the electrode behaviour involved. The graphs show that, as the cell charges, the potential difference between the electrodes (i.e. cell voltage) increases and reaches the set maximum of 1.8 V. Here, LMO reaches 1.2 V vs. SHE at its maximum charge (i.e. fully de-lithiated), and the AC reaches -0.6 V vs. SHE (i.e. from EDLC formation with Li^+). At full charge the recorded specific capacity of the cell is 25 mAh/g considering the combined mass of the active materials.

On discharge, the average cell voltage is 1.28 V and the specific discharge capacity also ~25 mAh/g (i.e. close to 100% coulombic efficiency). Here, the specific energy ('SE') using equation (2.2) is specific capacity ('Q/m') \times 'V',

$$SE = \frac{Q \times V}{m} \quad (2.2)$$

$$25 \text{ mAh/g} \times 1.28 \text{ V} = 32 \text{ Wh/kg}$$

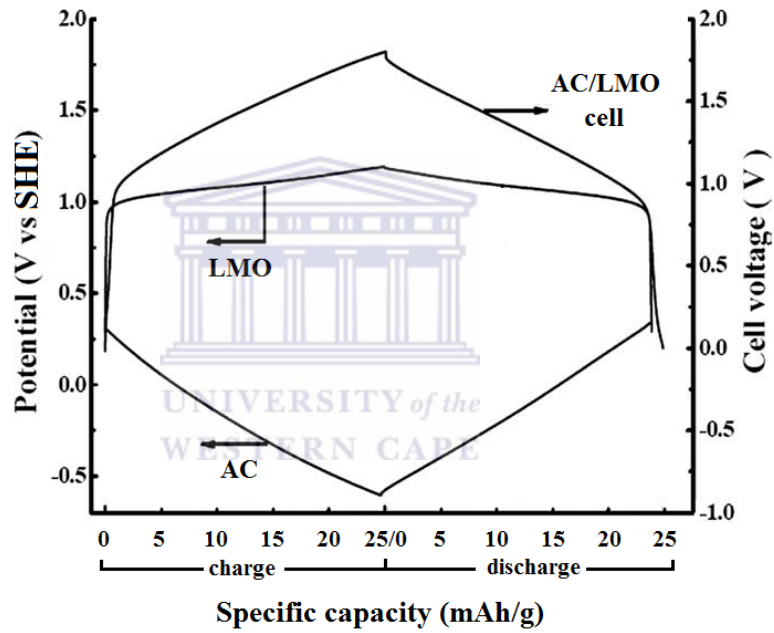


Fig 4.4 Schematic showing derivation of the 32 Wh/kg from AC/LMO active materials, adapted from [6] to show specific capacity.

Using the mass fractions of the AC and LMO and the cell's specific capacity, the specific capacities of the AC and LMO at their respective current densities are as follows:

- AC specific capacity = $25 \text{ mAh/g} / 0.6 = 37.5 \text{ mAh/g}$ at 300 mA/g
- LMO specific capacity = $25 \text{ mAh/g} / 0.3 = 75 \text{ mAh/g}$ at 600 mA/g

And, for AC, 37.5 mAh/g was obtained over +0.35 to -0.6 V vs. SHE (i.e. 0.95 V) and for LMO 75 mAh/g was obtained over +0.9 to +1.2 vs. SHE (i.e. 0.32 V). Therefore, the above figures provided a basis for evaluating the AC and LMO used in the present study.

4.2.3.2 Effect of charging voltage on specific capacity at a fixed current density

The following study aimed to establish if the AC and LMO could provide the above specific capacities over the same potential ranges used by Wang et al. Here, the potentiometer leads of the cycling channel were connected to the electrode of interest and an SCE reference electrode. This allowed cycling the electrode over a fixed potential range while directly recording its capacity. Table 4.1 summarizes the settings and targets. The experiments used a counter electrode of AC or LMO of $>2 \times$ the expected capacity of the electrode of interest.

Electrode	Potential range (V vs. SHE)	Current density (mA/g)	Active Mass used (mg)	Target ave. potential (V vs. SHE)	Target SQ (mAh/g)
AC	Starting V to -0.6	300	17.2	-0.13	37.5
LMO	Starting V to +1.2	600	8.87	+1.05	75

Table 4.1 Setting and targets for establishing a comparison of active materials

- *Results and discussion*

Fig 4.5 (upper plot) overleaf shows the specific capacity of AC cycled at 300 mA/g between its starting potential of +0.412 V vs. SHE and -0.6, -0.65, -0.7, -0.75, -0.8 and -0.85 V vs. SHE. The results show that the starting potential of the AC electrode was -0.062 V vs. SHE higher than the target figure of +0.35 V vs. SHE. This represents a 6% larger voltage range for EDLC charge storage of Li^+ , i.e. capacity. However it also means that the average cell voltage difference between AC and LMO would be lower at the beginning of charge and at the ending of discharge. Charging to -0.6 V vs. SHE produced an average voltage of ~ -0.12 V compared to the target figure of -0.13 V vs. SHE, and the specific discharge capacity of AC was 33.14 mAh/g, $\sim 12\%$ lower than the target figure of 37.5 mAh/g. In terms of specific capacitance (F/g), this is also lower considering the greater voltage range. The difference being 177.9 F/g compared to 142.1 F/g, however the larger voltage range is a mitigating factor. Setting the charging to lower potentials resulted in increased capacity but at the expense of coulombic efficiency, which dropped to only 95% at -0.9 V vs. SHE, Fig 4.4 (lower plot). The shape of the charge curve also begins to bend slightly upward from -0.8 V vs. SHE and below, indicating the onset of hydrogen evolution.

Fig 4.6 (upper figure) shows the specific capacity of LMO cycled at 600 mA/g between its starting potential of +0.559 V vs. SHE and +1.2, 1.25, 1.3, 1.4, 1.45 and 1.5 V vs. SHE. Increasing the charging voltage resulted in increased discharge specific capacity from 58 mAh/g to 81 mAh/g between +1.2 and +1.5 V vs. SHE respectively. This occurred with increased voltage drop between charge and discharge, and an increasingly upward turn of the charge curve indicating full de-lithiation of LMO. The discharge plots also show a slight wave at their beginning at higher voltages, the origin of which remains unclear. At +1.3 V vs. SHE, the voltage drop of ~ 0.1 V falls just below 1.2 V vs. SHE, which suggests that this charging limit would leave an electrode at a resting potential below that of oxygen evolution. This charging potential also matched the target figure of 75 mAh/g. The lower plot in Fig 4.5 shows that coulombic efficiency remained above 95% across the increasing charge voltage on LMO. This indicates that oxygen evolution was minimal, and that rapid polarization of LMO on full lithiation at the high current density of 600 mA/g probably prevented its occurrence.

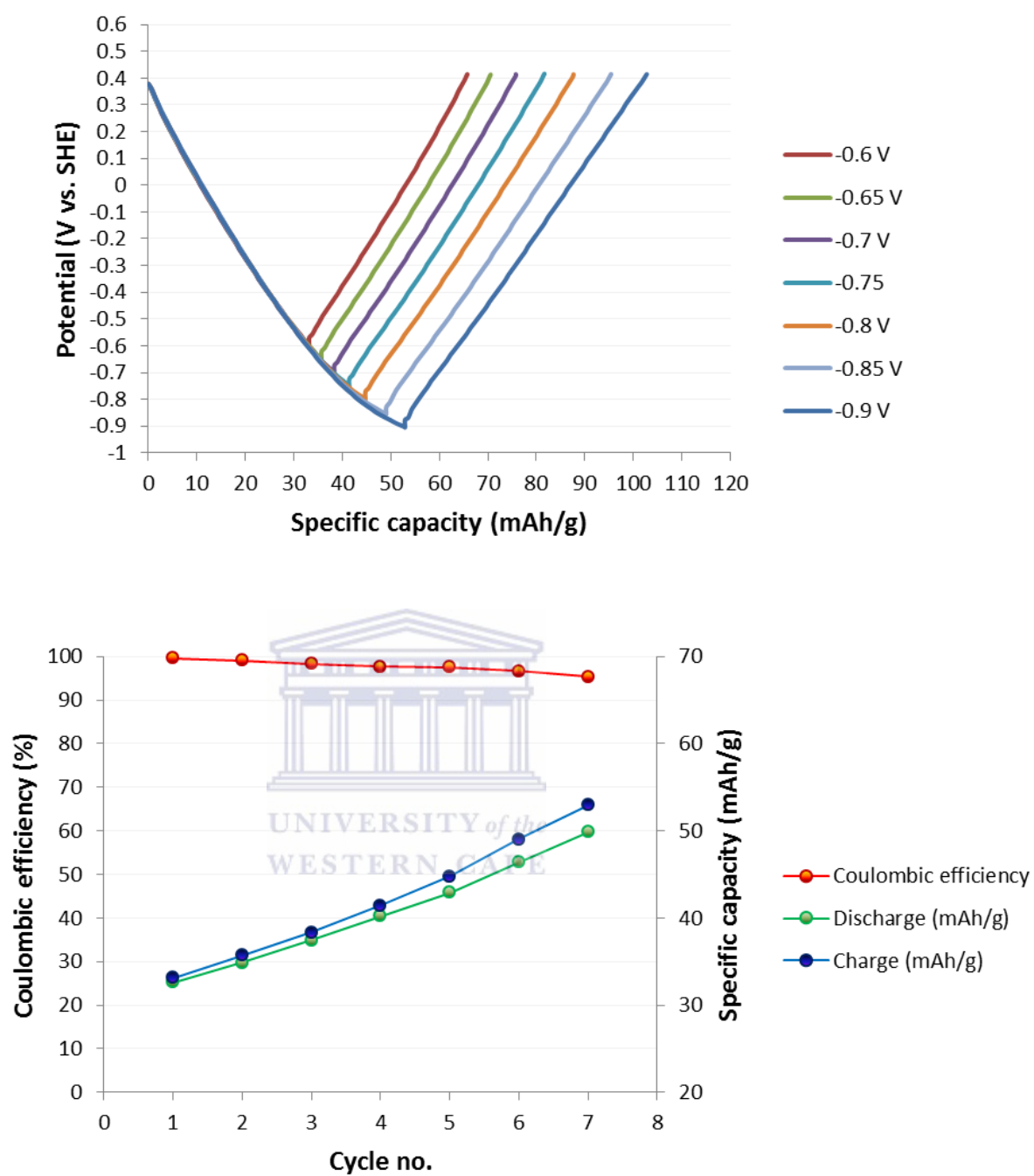


Fig 4.5 Charging thin-film AC electrode at 300 mA/g to a series of lower potentials from -0.6 to -0.9 V vs. SHE (above). Effect on coulombic efficiency (below), where cycle numbers 1 to 7 represent -0.6 to -0.9 V vs. SHE.

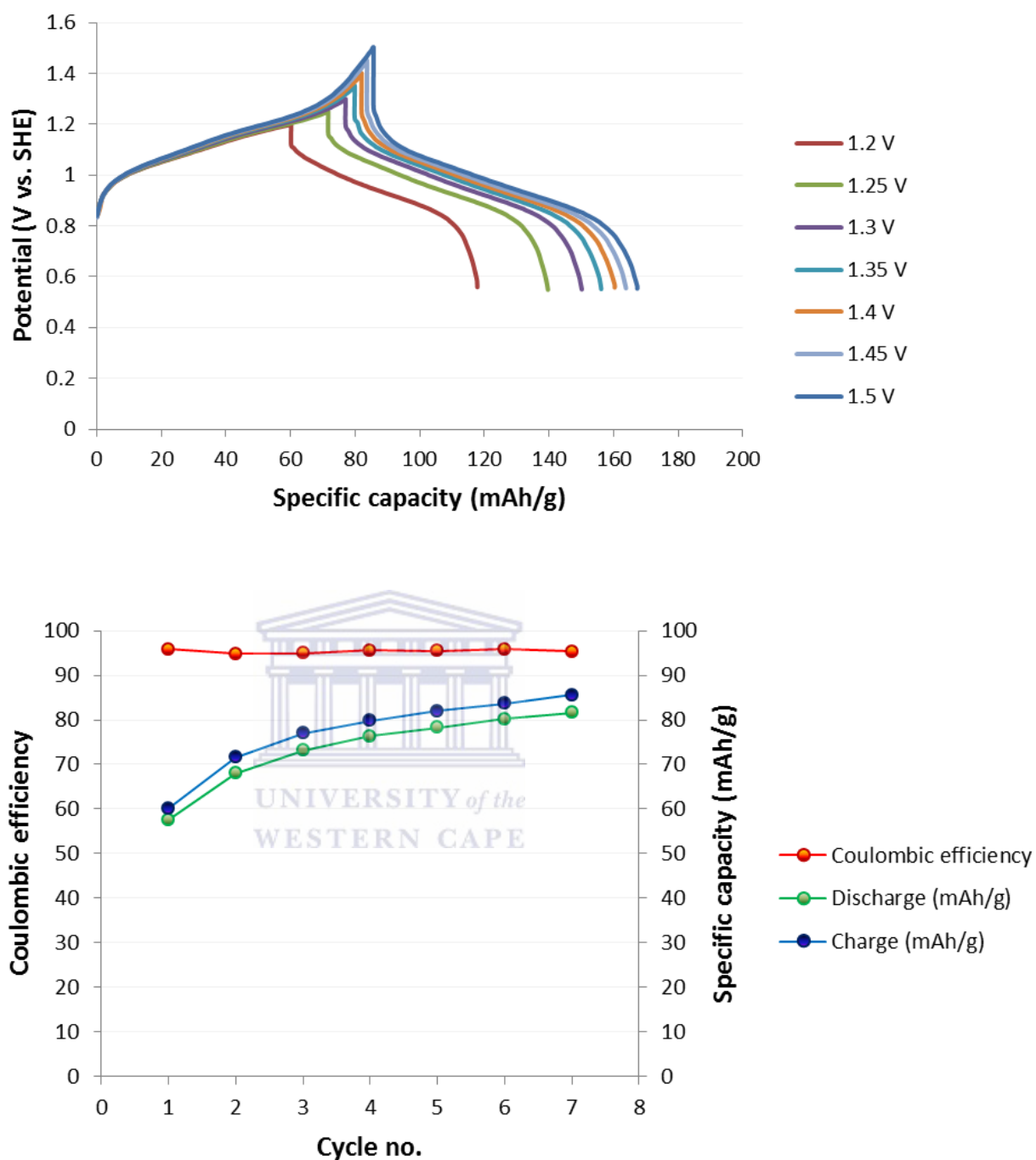
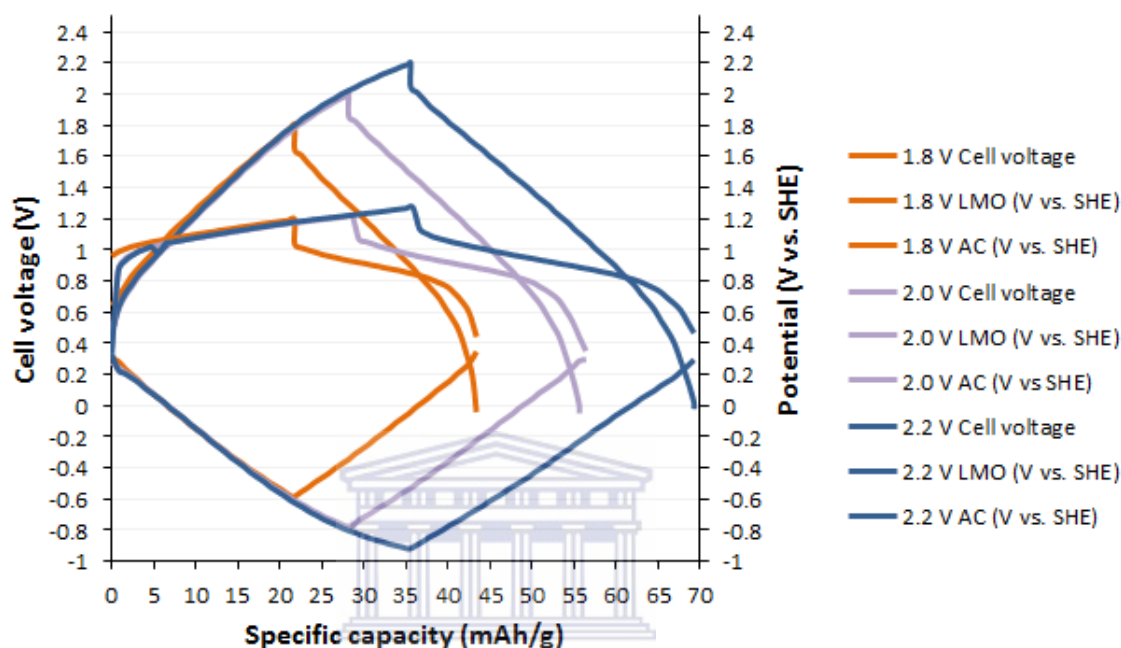


Fig 4.6 Charging thin-film LMO electrode at 600 mA/g to a series of higher potentials from +1.2 to +1.5 V vs. SHE (above). Effect on coulombic efficiency (below), where cycle numbers 1 to 7 represent +1.2 to +1.5 V vs. SHE.

The above results suggested that AC and LMO can be quite safely charged beyond -0.6 V vs. SHE and +1.2 V vs. SHE respectively at 200 mA/g total current density. Therefore, to further explore this possibility, the two electrodes were placed together to form a cell, which was then charged to 1.8, 2.0 and 2.2 V at 200 mA/g. The



Cell voltage (V)	Charge (mAh/g)	Discharge (mAh/g)	Coulombic efficiency (%)	Ave. discharge (V)	Charge energy (Wh/kg)	Discharge energy (Wh/kg)	Energy efficiency (%)	Ave. discharge power (W/kg)	Rate (C)	Discharge time (min : sec)	P/E
1.8	23.44	23.33	99.5	0.95	25.45	22.16	87.1	190.0	8.6	6:54	9:1
2.0	27.0	26.44	98.0	1.14	35.33	30.14	85.3	228.0	7.6	7:53	8:1
2.2	36.34	34.67	95.4	1.21	50.73	41.95	82.7	242.0	5.8	10:20	6:1

Fig 4.7 Charging AC/LMO (2:1) at 200 mA/g up to 2.2 V, approaching the onset of hydrogen evolution on AC.

plot in Fig 4.7 shows the combined plots of the individual electrode potentials and cell voltage. Charging to 2.2 V produced a marked increase in specific energy and specific power. At 1.8 V, the average cell discharge was < 1.0 V and produced only 22 Wh/kg specific energy ($23 \text{ Ah/kg} \times < 1.0 \text{ V}$) and an average specific power of $< 200 \text{ W/kg}$ ($200 \text{ Ah/kg} \times < 1.0 \text{ V}$). In contrast, at 2.2 V the average cell discharge voltage rose to $\sim 1.21 \text{ V}$ and produced a specific energy 42 Wh/kg ($35 \text{ Ah/kg} \times 1.21 \text{ V}$) and an average specific power of 242 W/kg ($200 \text{ Ah/kg} \times \sim 1.21 \text{ V}$). Furthermore, the table in Fig 4.7 shows that the higher charging voltage only resulted in 5% reduction in energy efficiency. At 2.2 V charge, LMO charged beyond +1.2 V vs. SHE but dropped below this amount when the current switched to discharge. The AC electrode charge curve showed signs of upward curve toward the end of charge suggesting the onset of hydrogen evolution. Nevertheless, the 95% reversible coulombic efficiency suggests that perhaps hydrogen reabsorption occurred on discharge. This raised the question of whether the reversible nature of the charge was maintainable after a storage period at full charge. Therefore, the cells were then charged to 1.8 and 2.2 V and held for 30 min

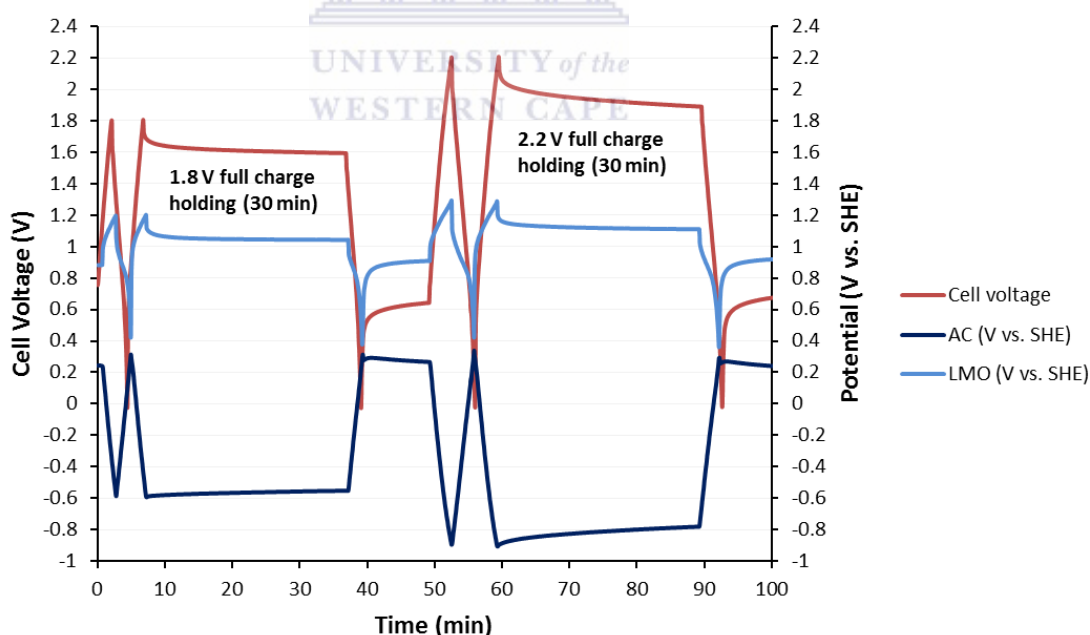


Fig 4.8 Full charge holding for 30 min at 1.8 and 2.2 V on AC/LMO (2:1).

at full charge and then discharged (Fig 4.8). The plot shows that the LMO electrode at both 1.8 V and 2.2 V cell charge voltages produced a stable, flat, holding plateau over the 30 min period. On the AC electrode, the cell charged to 2.2 V showed a faster gain in potential over the holding period compared to the cell charged to 1.8 V. However, the resultant loss in energy efficiency caused by the holding period at 2.2 V amounted to < 3% of the value obtained previously without the holding period, comparing 82.7 and 81.4% energy efficiencies respectively.

- *Conclusions*

Overall, the specific capacities of AC and LMO at their target charging voltages and respective current densities were: 33.14 mAh/g and 58 mAh/g, compared to the targets of 35.7 mAh/g and 75 mAh/g. However, while these values are lower than the targets, the study found that charging LMO above +1.2 V vs. SHE, and AC below -0.6 V could produce higher specific capacities with little loss of coulombic efficiency. Using an active material mass ratio of 2:1 (AC:LMO) and charging cells to 2.2 V at 200 mA/g, the active materials could produce a specific energy of 42 Wh/kg and a specific power of 420 W/kg, which amounts to nearly double the specific energy and specific power obtained at 1.8 V at the same current density. The gain in specific energy would appear to far outweigh the 5% loss of energy efficiency by charging to 2.2 V, and the <3% difference in full charge holding efficiency over a 30 min period.

4.2.3.3 Effect of current density on 2:1 mass ratio (AC:LMO) thin film electrodes

To examine the effects of current density on specific capacity, electrodes of 2:1 (AC:LMO) mass loading ratio were cycled at 0 – 1.8 V over a range of 400, 200, 100, 50 and 25 mA/g. The effects of current density were examined on individual electrode potentials and cell voltage monitored simultaneously as the cells cycled.

- *Results and discussion*

Fig 4.9, from top to bottom, shows the cell voltage/time plot (top), the LMO potential/time plot (middle) and the AC potential/time (bottom) of the cell cycled at 0 – 1.8 V over the 400 to 25 mA/g range. The plots show how cell voltage changes as the

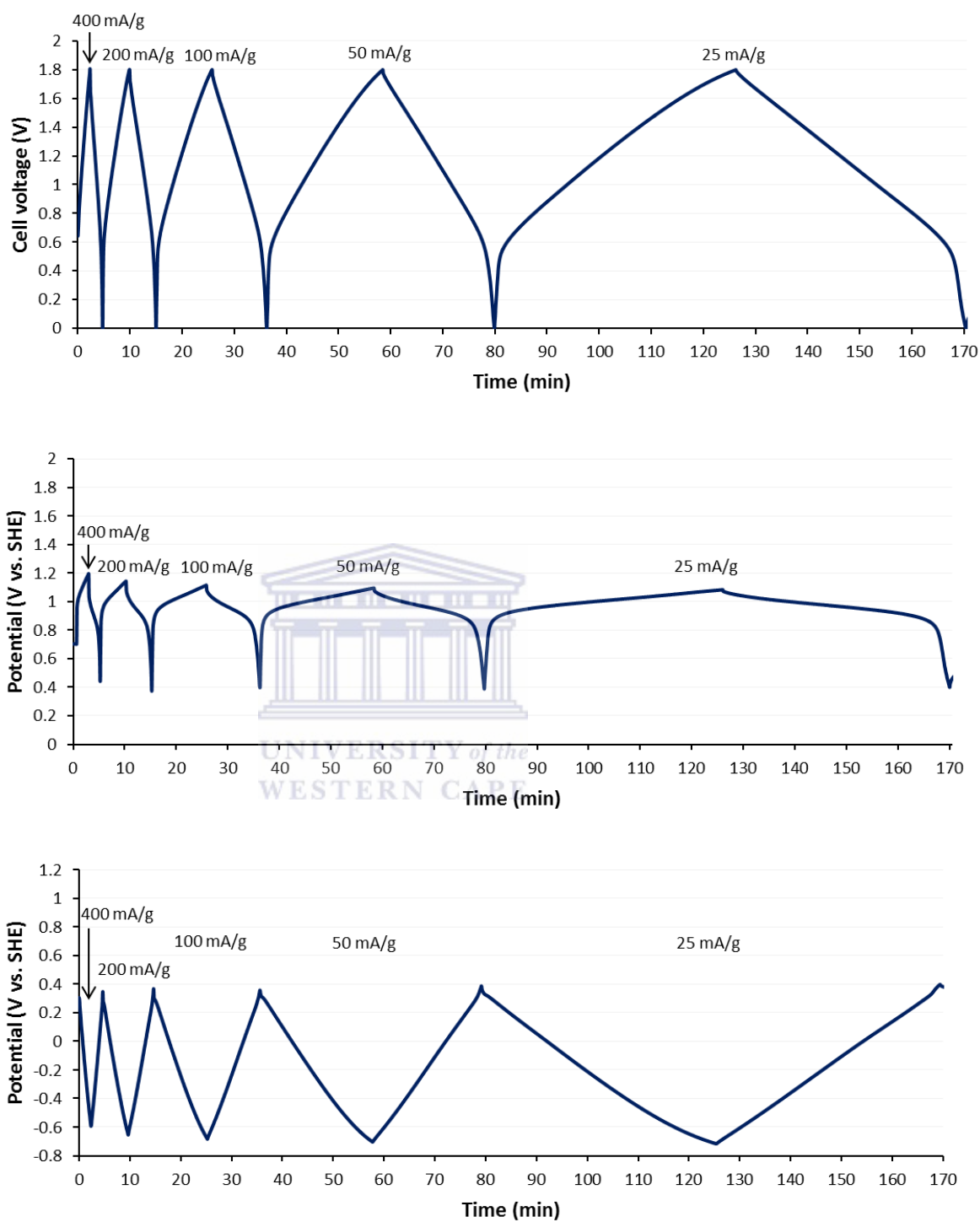


Fig 4.9 Three voltage/time plots of AC/LMO (2:1) charged 1.8 V over 400 – 25 mA/g showing: cell voltage (top); LMO potential (middle), and; AC potential (bottom).

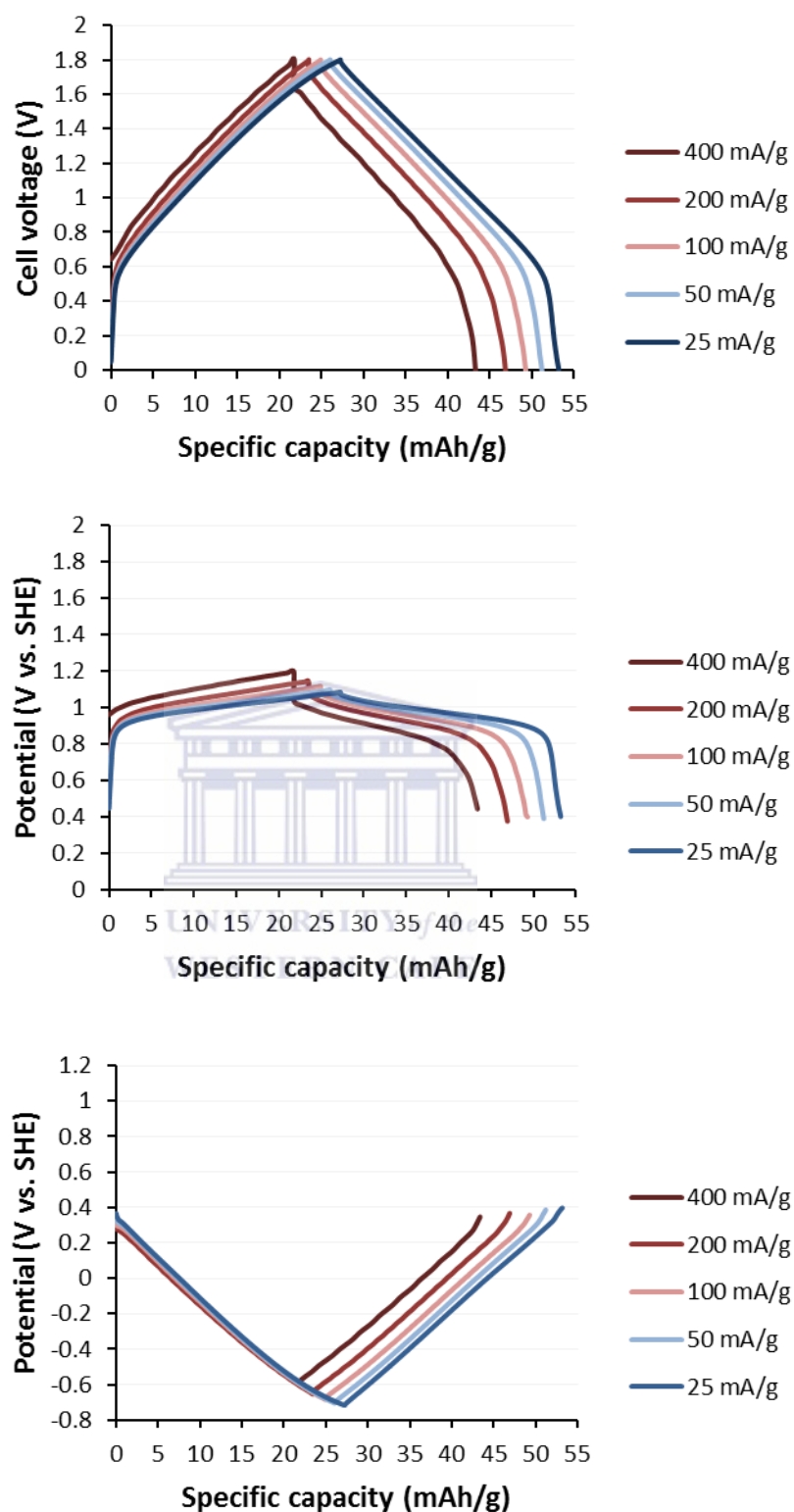


Fig 4.10 Three voltage/specific capacity plots of AC/LMO (2:1) charged to 1.8 V at 400 – 25 mA/g showing: cell voltage (top); LMO potential (middle), and; AC potential (bottom).

vector sum of the individual electrode voltages during charge and discharge. Fig 4.10, shows the voltage profiles plotted against cell specific capacity. Here, the LMO potential plot shows the upper limit of its charge potential decreased with decreasing current density, from +1.2 V at 400 mA/g and dropping to below +1.1 V vs. SHE at 25 mA/g. This trend coincides with decreasing voltage drop between charge and discharge, resulting in less difference between the average charge and discharge voltage. Therefore, specific capacity of LMO decreases with increased current density as a result of electrode polarization.

The increase in available LMO specific capacity with decreasing current density caused the AC electrode to charge to lower potentials for the cell to reach its full charge voltage limit of 1.8 V. At 25 mA/g, AC reached close to -0.75 V vs. SHE, whereas LMO only reached +1.05 V vs. SHE. Therefore, at low current densities more AC could be used to achieve capacity balance on the electrodes. Fig 4.11 (below) shows that optimal energy efficiency was reached at 50 mA/g, after which the energy efficiency began to drop due

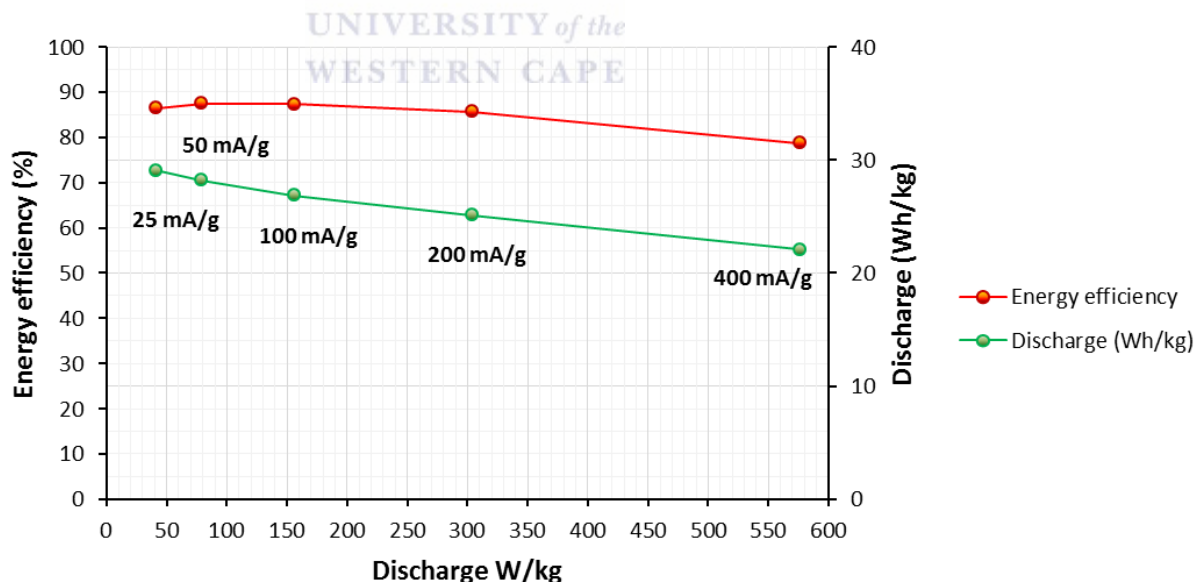


Fig 4.11 Ragone plot and energy efficiency of AC:LMO (2:1) charged to 1.8 V 400 – 25 mA/g. Showing maximum energy efficiency at 50 mA/g.

to hydrogen evolution on the AC due to the low potential reached in combination with the low current density of 25 mA/g.

- *Conclusions*

Increasing current density significantly lowered the specific capacity of the LMO electrode. Here, increasing polarization caused LMO to reach higher potentials at a faster rate, which caused the cell to reach 1.8 V at a faster rate. Conversely, increasing current density did not cause any significant polarization on the AC electrode, but rather polarization on LMO indirectly determined the extent of its charge. Therefore, the results are consistent with the different means of charge storage on the electrodes, where Li^+ intercalation in LMO has notably higher resistance than that of Li^+ EDLC formation on the AC surface. The results also suggest that at lower current densities on thin-film electrodes, a higher than 2:1 ratio of AC:LMO would allow the cell to be charged to the full extent of LMO capacity rather than forcing the AC electrode closer to hydrogen evolution potential. Conversely, at high current densities, increasing AC ratio content would push LMO even closer to oxygen evolution potential which would ultimately increase the risk of metal current collector corrosion. Weighing up these possible outcomes, the 2:1 ratio would appear a safe balance that places the strain on the more stable AC electrode rather than on LMO and the current collectors.

4.3 A study on AC/LMO electrode material loading density

The thickness, or loading density, of electrode material on current collectors is an important determinant of cell properties (e.g. Wh/kg, W/kg, cost/kWh and cost/kW). The majority of studies on AIBs report only the active material's specific energy and specific power in thin film electrodes. Such electrodes, owing to the vastly larger mass percentage of current collector, would offer little more than 10% of their active material value of specific energy and specific power as a practical cell format. Therefore, higher loading densities of active material on current collectors are essential for practical cells. The following study explores the effect of loading density on cell performance.

4.3.1 Experimental

4.3.1.1 Standardized testing conditions

In addition to electrode loading density, other variables relating to electrode and cell construction can also affect cell performance. For instance, the elasticity/shear factor of electrode film material can vary depending on the amount of electrode dough kneading time. This can affect the extent of particle contact and interstitial pore space between the particles. Secondly, the assembly pressure of the electrodes in the cell can also affect these factors. Therefore, both preparation methods and cell construction need to be as consistent as possible to avoid these variables.

4.3.1.2 Choice of current collector

The choice of current collector material constitutes an entire field of study in itself, since both its mass and cost contribution in the cell will vary with its thickness and make up. For the present study a standard 80-mesh 304 stainless steel (Alfa Aesar) current collector was chosen based on its common use in AIB research and large surface area for contact with the active material (Fig 4.11). The mesh area density was $\sim 60 \text{ mg/cm}^2$ with a wire thickness of $\sim 0.1 \text{ mm}$ and a mesh thickness of $\sim 0.2 \text{ mm}$.

4.3.1.3 Construction of an adjustable test cell

In order to test a range of electrode thicknesses, an adjustable cell was designed that could supply sufficient contact pressure for the electrode assembly and house a reference electrode. The cell was constructed from a clear acrylic block which allowed inspection of the electrode assembly during cycle tests (Fig 4.11). The central well in the middle of the cell houses the electrode assembly (anode/cotton cloth separator/cathode) and allows insertion of a reference electrode above it. The flat ends of two internal stainless steel 316 rods forms the contact point with the metal mesh current collectors of the electrodes. Each rod has two rubber O rings to prevent electrolyte leakage. Behind the rods, a threaded internal bolt allows tightening of the cell, which in turn has a second thinner bolt attachment to attach the clips of the battery cyclor.

4.3.1.4 Variable loading density disc electrodes

The electrodes for the above cell comprised 1 cm² discs of 304 stainless steel 80 mesh current collectors onto which 85:10:5 mass ratio electrode dough was pressed in a cylindrical die at 12 MPa for 5 min. To maintain consistency of electrode dough, 1 g batches of dough were made with a consistent method of kneading (Section 4.1.1.3). The range of electrode loading densities spanned five doublings of thickness from a starting quantity of 10 mg of electrode film (Fig 4.12). Table 4.2 shows the corresponding measured thicknesses and amounts of active material involved.

AC electrode			LMO electrode		
Thickness (mm)	Total mass (mg)	AC mass (mg)	Thickness (mm)	Total mass (mg)	LMO mass (mg)
0.11	10	8.5	~0.05	10	8.5
0.219	20	17	0.088	20	17
0.436	40	34	0.175	40	34
0.875	80	68	0.35	80	68
1.75	160	136	0.7	160	136
3.5	320	272	1.4	320	272
7.0	640	544	-	-	-

Table 4.2 Electrode thicknesses and the corresponding masses of electrode material

4.3.1.5 Terminology used for loading density

The study refers to ‘loading density’ as the total active material (AC + LMO) used on two 60 mg, 1 cm² current collectors. E.g. a stated ‘50 mg loading density’ refers to 50 mg of total active material, which at 2:1 (AC:LMO) comprises 33.33 mg AC and 16.66 mg LMO each on a 60 mg current collector. Calculations for ‘total cell’ specific capacity and energy etc. were made considering the mass contributions of active materials, electrode film additives, electrolyte and current collectors.

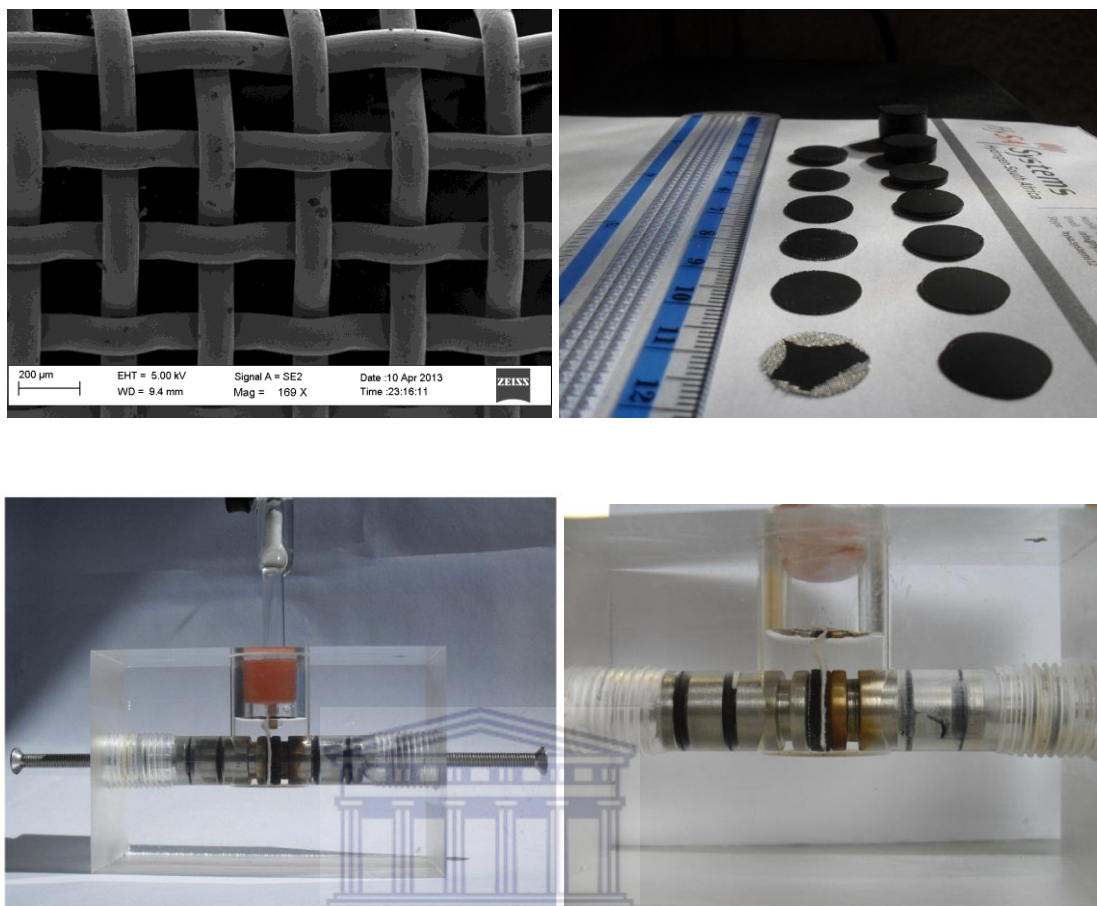


Fig 4.12 SEM of the 304 stainless steel 80-mesh current collector at 169 × mag (top left). Photograph of disc electrodes (top right) with loading densities of 10 – 320 mg/cm² of LMO electrode dough (left of picture), and 10 – 640 mg/cm² of AC electrode dough (right of picture). Photographs of the adjustable test cell (below) with close-up of electrode assembly showing electrodes and cotton cloth separator.

4.3.1.6 Current density range, electrode loading density and cell voltage

The current densities of interest for high power applications lay between 1000 and 1300 mA/g in respect of the combined mass of AC and LMO active materials. This range corresponded to the 50:1 (P/E) for high power applications. Current densities of 600, 800, 1000, 1200 and 1400 mA/g were tested on three sets of electrode mass loading densities corresponding to 25, 50 and 100 mg of active material where the AC:LMO mass ratio was 2:1. Cells were charged to 1.8 and 2.2 V over the range of current densities tested.

4.3.2 Results and discussion

4.3.2.1 Effect of loading density on active material voltage drop and specific capacity

In Section 2.5, the calculated adjustment to achieve a practical cell of 40% of the active materials specific energy required $\sim 3.5 \times$ higher loading density than the thin-film (~ 25 mg active material) format. The following study compared the cycling performance of thin film to that of two doublings of electrode material loading density, representing 25, 50 and 100 mg of total active material. The cells were cycled at current densities from 600 – 1400 mA/g, which spanned the 50:1 P/E (1000 – 1300 mA/g) ratio reported by Wang et al, for the thin film format.

Fig 4.13 shows the voltage/specific capacity plots of 25, 50 and 100 mg active material loading density of the cells charged to 1.8 V. Comparing the three plots, the effect of loading density on electrode polarization is clearly visible in the form of increasing voltage drop as loading density increases. Interestingly, the highest discharge specific capacity came from the 50 mg loading density at 600 mA/g and not from the 25 mg. The reason for this is unclear, but might relate to the inability to apply the same electrode assembly pressure to the very thin film LMO electrode. Here, the bulk of the film's mass lay between wires of the current collector, which effectively shielded it from the electrode assembly pressure. This aside, at higher current densities, the effect of increased loading densities dramatically reduced the cells' specific capacity: e.g. comparing specific capacities at 1400 mA/g which drop from 15, 13, to 3 mAh/g over the 25, 50 and 100 mg loading densities.

Comparing the extent of voltage drop over all current densities tested between the three loading densities, the effect of doubling the loading density was roughly equivalent to doubling the current density. Furthermore, the effect of increasing the loading density increased the percentage decrease of specific capacity over the current density range tested. Here, the difference between specific capacity at 600 mA/g compared to 1400 mA/g dropped by 34, 44, and 74% in 25, 50 and 100 mg loading densities respectively. Therefore, while the effect of loading density on voltage drop was roughly

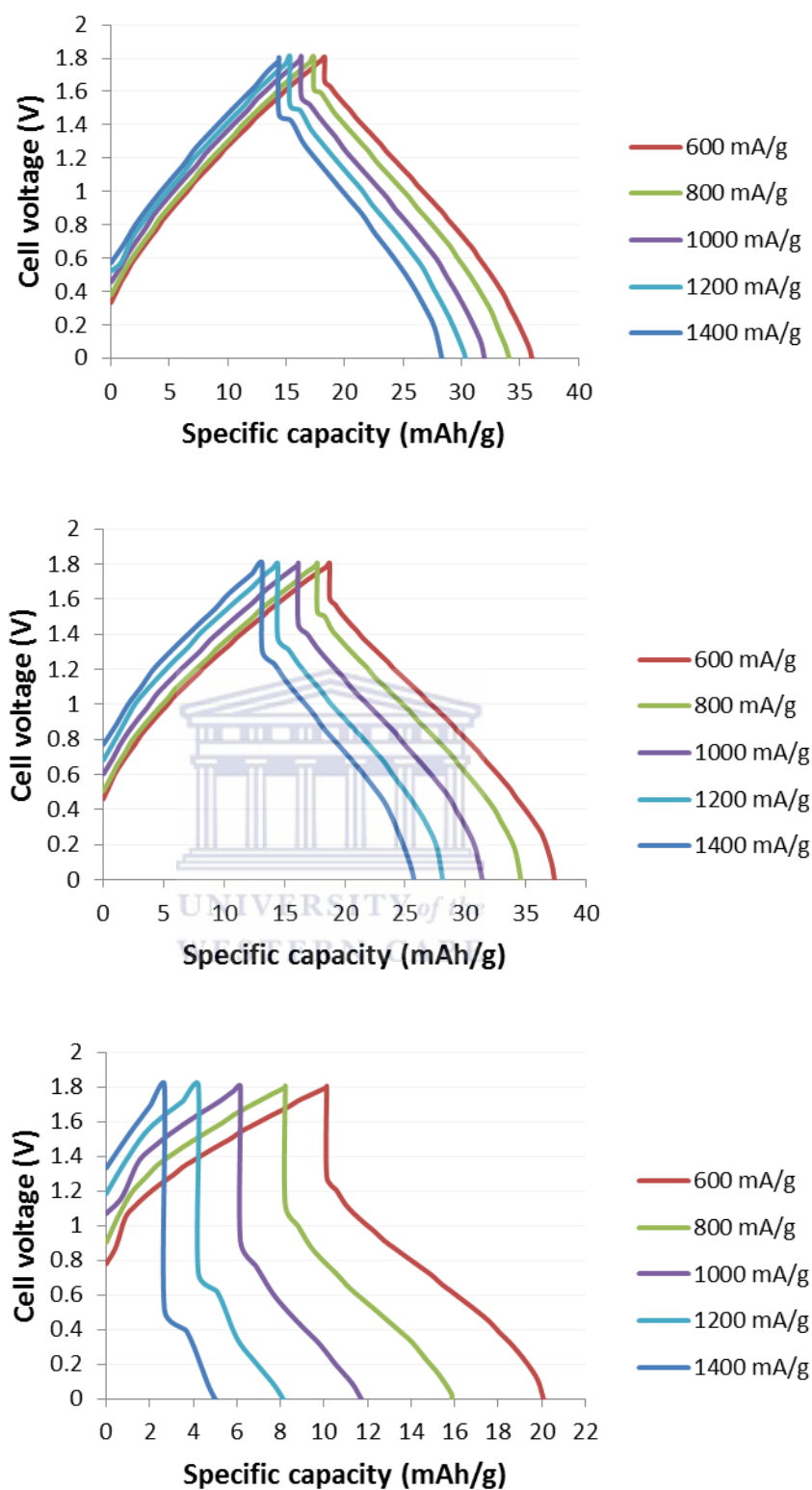


Fig 4.13 Effect of current density on three loading densities of active material at 2:1 mass ratio: 25 mg (top), 50 mg (middle) and 100 mg (bottom) charged to 1.8 V.

linear, its effect on specific capacity was more pronounced, suggesting that as film thickness increases an additional mechanism of specific capacity decrease occurs. This relates to resistance increases in electrolyte ion movement within the interstitial spaces of the film, and to electron conductivity.

Interestingly, the graphs also show that the relationship between the size of voltage drop and specific capacity is different in 25, 50 and 100 mg loading densities. The matching sized voltage drop of 0.04 V at 1400 mA/g in 25 mg and at 1000 mA/g in 50 mg produced different specific discharge capacities of 13 mAh/g and 15 mAh/g respectively. Conversely, the matching sized voltage drop of ~0.06 V at 1400 mA/g in 50 mg and at 600 mA/g in 100 mg produced specific capacities of 12 mAh/g and 9.5 mAh/g respectively. Therefore, again this signifies a more complex relationship between resistance and specific capacity. Overall an increase in loading density had the same affect as an increase in current density on voltage drop across the 25, 50 and 100 mg range. However, increasing loading density from 50 and 100 mg caused greater voltage drop and and greater reduction in specific capacity than from 25 to 50 mg.

4.3.2.2 *Effect of loading density on specific energy and specific power*

Given that the purpose of increasing loading density was to counter the effect of current collector mass contribution on specific energy, the calculations in Table 4.3 show the total specific energy and specific power of a practical cell using 25, 50 and 100 mg active material loading densities. The ‘cell total’ rows of the table consider the combined mass of electrode dough with electrolyte (77.3% active materials, 9.1% carbon black, 4.5% electrolyte), two current collectors (total 120 mg) and separator (10 mg) (reviewed in Section 2.5). Fig 4.14 shows the values and their respective energy efficiencies. The plot shows that none of the loading densities can reach the target figure proposed in Section 2.5 of 8 Wh/kg: 400 W/kg at the top of the 50:1 P/E line in the figure. At 25 mg of active materials, the mass of current collector renders the active material mass at only 15.4% of the cell total. At 100 mg of active materials, while forming a higher percentage of cell mass, the loss of specific capacity and large voltage drop (shown previously in Fig 4.13) results in very low specific energy at high current

	600 mA/g		800 mA/g		1000 mA/g		1200 mA/g		1400 mA/g	
	Wh/kg	W/kg	Wh/kg	W/kg	Wh/kg	W/kg	Wh/kg	W/kg	Wh/kg	W/kg
25 mg AM:	17.77	583.68	16.76	770.32	14.75	892.8	14.06	1104.48	13.12	1201.34
Cell total:	2.74	89.89	2.58	118.63	2.27	137.49	2.17	170.09	2.02	185.01
AM mass (15.4%)										
50 mg AM:	18.55	596.73	15.46	731.12	13.54	886.6	11.08	967.92	9.95	1093.26
Cell total:	4.77	153.36	3.97	187.90	3.48	227.86	2.85	248.76	2.56	280.97
AM mass (25.7%)										
100 mg AM:	7.08	427.08	4.41	462.72	2.26	481.05	1.42	517.13	0.96	545.44
Cell total:	4.44	267.78	2.77	290.13	1.42	301.62	0.89	324.24	0.60	341.99
AM mass (62.7%)										

Table 4.3 Comparison of specific energy and specific power of active material (AM) and cell total, using 25, 50 and 100 mg of active materials.

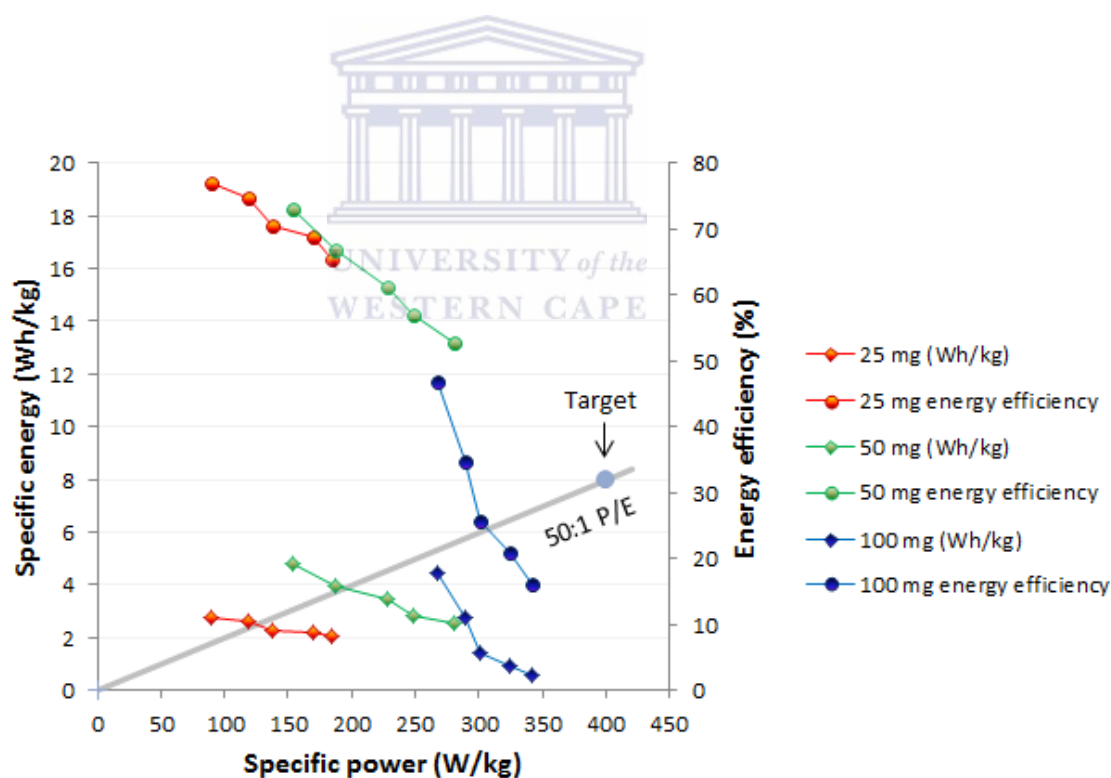


Fig 4.14 Ragone plot of cells charged to 1.8 V, showing cell total specific energy, specific power and energy efficiency using 25, 50 and 100 mg loading densities of active materials (each cycled at 600, 800, 1000, 1200 and 1400 mA/g).

densities and very low energy efficiency. However, the 100 mg plot suggests that a current density lower than 600 mA/g would intersect the 50:1 P/E ratio line at a higher point than the lower two loading densities with predictably higher than 50% energy efficiency at 600 mA/g. At 50 mg, a value of 4 Wh/kg: 200 W/kg was obtained on the 50:1 P/E ratio line, with close to 70% energy efficiency, which among the plotted points would represent the optimal value, albeit at almost exactly half the value predicted in Section 2.5. Therefore, a battery at this specific energy and specific power, for a 0.4 kWh FCEV, would be 100 kg as opposed to the target of 50 kg.

4.3.2.3 *Effect of cell charging to 2.2 V*

In Section 4.2 (4.2.3.1), charging cells beyond 1.8 V to 2.2 V at 200 mA/g resulted in considerable increase in specific energy and specific power. Fig 4.15 shows the voltage/specific capacity plots of 25, 50 and 100 mg loading densities charged to 2.2 V over 600, 800, 1000, 1200 and 1400 mA/g current density range. The plots show the same general trends observed for charging to 1.8 V, with the notable difference that the average discharge voltages and specific capacities are considerably higher. The difference between voltage drop of the lowest and highest current density was also less for all three loading densities at 2.2 V. Also, there was a notably larger voltage drop at 1400 mA/g at 1.8 V charging compared to 1400 mA/g at 2.2 V (comparing 100 mg loading density plots in Fig 4.13 and 4.15). These phenomena therefore suggest an association with either charging time or a relationship between voltage drop and the amount of charge on the electrode.

Fig 4.16 shows the plotted cell total specific energy, specific power and energy efficiency. Here, the plot for the highest loading density of 100 mg did intersect the 50:1 P/E line at the target value of 8 Wh/kg: 400 W/kg. However, at this value the energy efficiency was only ~42%. Further down the 50:1 P/E line, the plot for 50 mg loading density intersects the 50:1 P/E line at 6 Wh/kg: 300 W/kg at a higher energy efficiency of 60%. Therefore, the effect of charging to 2.2 V increased specific energy and specific power by ~33.3%, but with an accompanied loss in energy efficiency of ~5%. The loss of energy efficiency would appear to derive less from voltage drop and more from loss of coulombic efficiency through hydrogen evolution at the AC anode at low potentials.

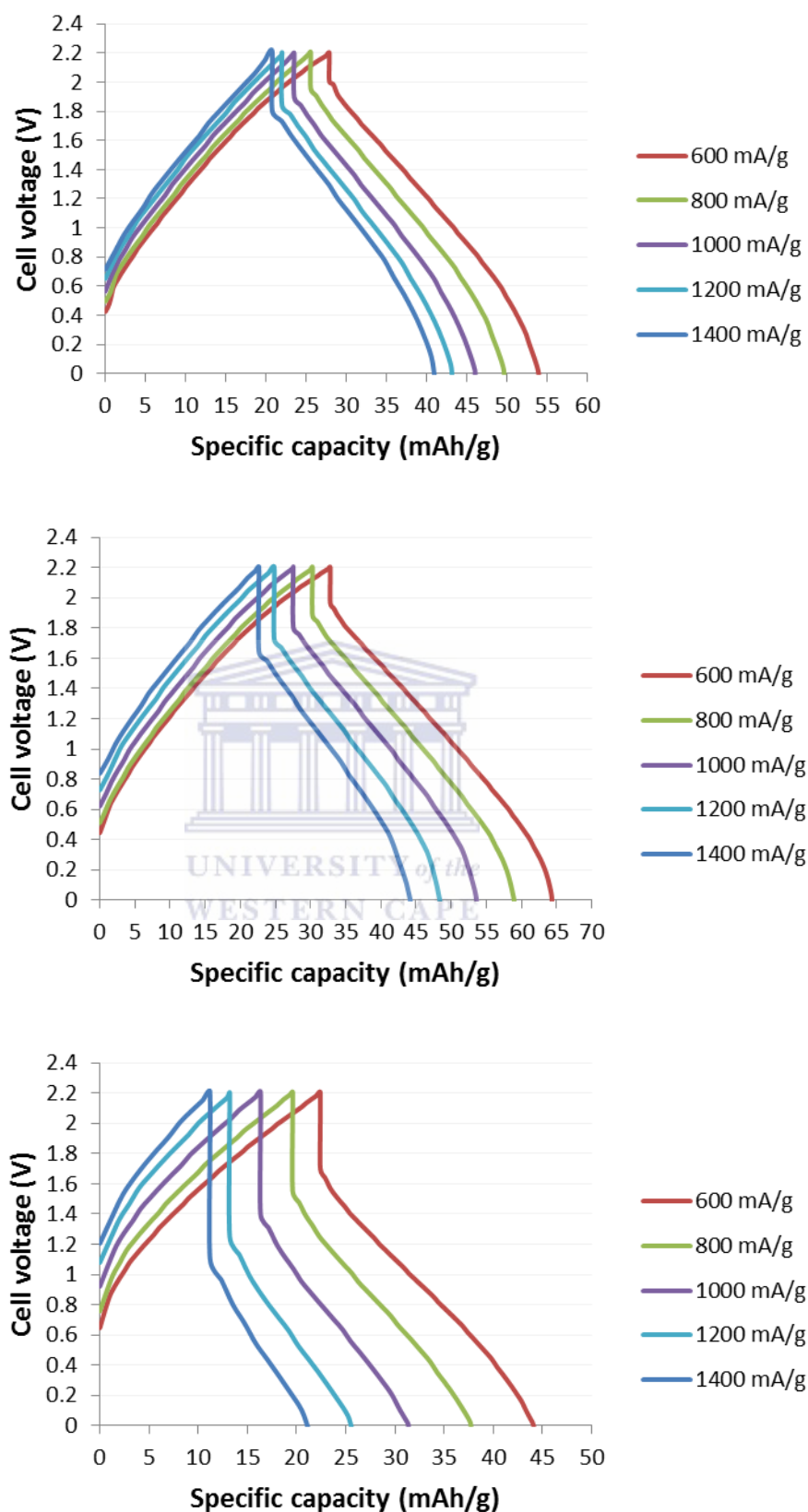


Fig 4.15 Effect of current density on three loading densities of active material at 2:1 mass ratio: 25 mg (top), 50 mg (middle) and 100 mg (bottom) charged to 2.2 V.

	600 mA/g		800 mA/g		1000 mA/g		1200 mA/g		1400 mA/g	
	Wh/kg	W/kg	Wh/kg	W/kg	Wh/kg	W/kg	Wh/kg	W/kg	Wh/kg	W/kg
25 mg AM:	30.10	693.06	27.28	906	24.17	1075.4	22.10	1252.56	21.03	1451.8
Cell total:	4.64	106.73	4.20	139.52	3.72	165.61	3.40	192.89	3.24	223.58
AM mass (15.4%)										
50 mg AM:	35.11	667.56	31.31	873.68	26.97	1030.5	23.39	1189.32	21.42	1381.94
Cell total:	9.02	171.56	8.05	224.54	6.93	264.84	6.01	305.66	5.50	355.16
AM mass (25.7%)										
100 mg AM:	19.19	530.64	13.96	616	10.47	698.1	7.79	753.72	5.44	758.66
Cell total:	12.03	332.71	8.75	386.23	6.56	437.71	4.88	472.58	3.41	475.68
AM mass (62.7%)										

Table 4.4 Cells charged to 2.2 V. Comparison of specific energy and specific power of active material (AM) and cell total, using 25, 50 and 100 mg of active materials.

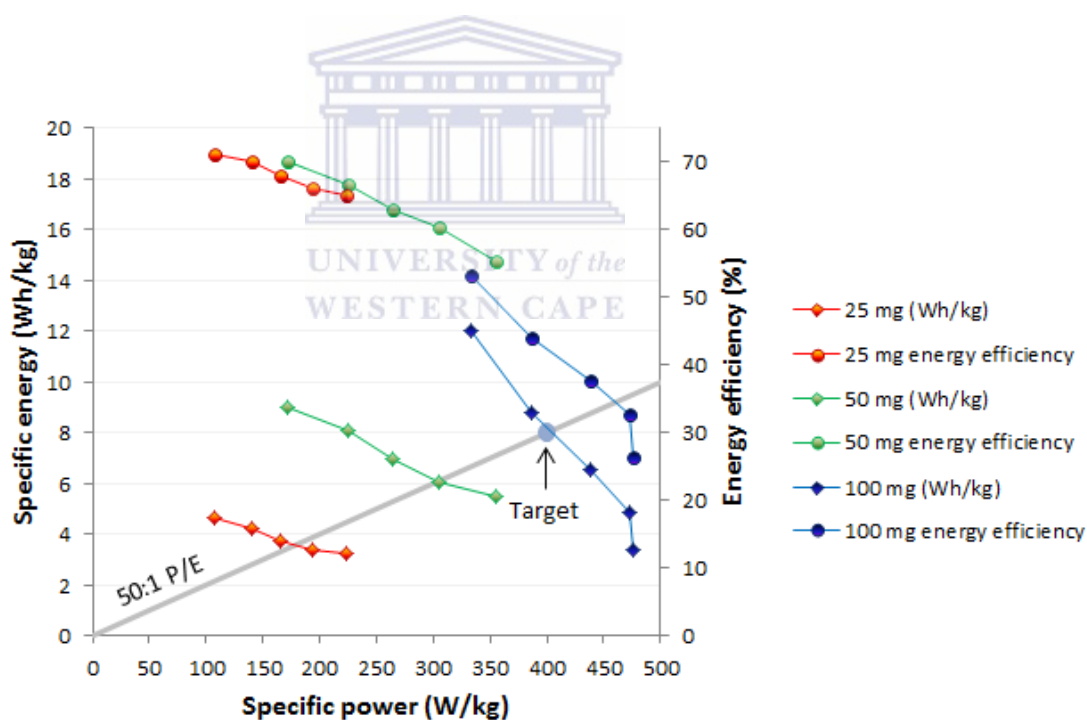


Fig 4.16 Ragone plot of cells charged to 2.2 V, showing cell total specific energy, specific power and energy efficiency using 25, 50 and 100 mg loading densities of active materials (each cycled at 600, 800, 1000, 1200 and 1400 mA/g).

4.3.3 Conclusions

The main conclusions from the AC/LMO loading density tests at high power (i.e. spanning the 50:1 P/E) were as follows:

- The resistance of increased loading density does not allow the practical cell target figure of 8 Wh/kg:400 W/kg to be reached using a 1.8 V cell charge
- Charging cells to 2.2 V allows the target to be reached using a 100 mg loading density of active materials but at only 42% energy efficiency
- A 50 mg loading density at 1.8 V charge produced 4 Wh/kg:200 W/kg at 70% energy efficiency.
- A 50 mg loading density at 2.2 V charge produced 6 Wh/kg:300 W/kg at 60% energy efficiency.

The above results indicate that depending on energy efficiency requirements, various options concerning charge voltage and loading density can be applied for a 50:1 P/E. However, the above studies only considered the maximum power tolerance of the materials, which in practical applications represent variable fractions of the average power requirements. In the case of a high powered FCEV battery, a real test model would consider the power requirements of the drive cycle. Here, the overall energy efficiency of the cells would be higher than reported in the above studies and correspond to the average power required as opposed to just the maximum power required. Finally, the results show the importance of testing cells at practical loading densities, and that common assumptions on practical yields of specific energy and power by extrapolating results from thin film studies do not accurately predict thicker electrode film behaviour.

4.4 Up-scaling to a 3 Ah high power cell

The previous sections of this chapter experimentally established the specific energy that an AC/LMO cell might provide at high specific power (50:1 P/E) with optimized mass ratio and loading densities of active materials. However, larger cells for practical applications differ considerably in design to the cells used thus far in the study. Firstly, the electrode film materials in practical cell formats are pressed into both sides of the current collector. This is an advantageous feature in that the paths of electron and ion movement are halved, i.e. having to travel only half the thickness of the film to reach the current collector. In theory, this might have very beneficial effects on specific energy and power. However, accompanying this are negative features of up-scaling. Here, increased electrode size means that current must move longer distances from the far end of the electrode to the tab (point of external circuit attachment). Furthermore, as the electrode's width and length are increased, its surface area to volume ratio decreases, which ultimately increases the path length of ion movement to the interior of the film. Lastly, depending on the electrode or cell size, the amount of current passing through the tab connections at a 50:1 P/E can become formidably high and require safety considerations concerning heat management. E.g. for the seemingly small capacity of 1 Ah (less than a standard AA size battery) the required current for this amount of charge to pass at 50:1 P/E (at 1.2 min) is 50 A. Therefore, while the cell voltage of 1.8 V or 2.2 V poses no threat of electrocuting human beings, poorly connected tabs and wiring, or small short circuiting contact points, could overheat to cause sparks and burns.

To date the only published studies on AC/LMO cells in an up-scaled cell format have been done by the Aquion® group [4]. These cells have very thick electrode film layers of 6 and 3 mm thickness for AC and LMO respectively. The cells obtain a specific energy of 23 Wh/kg but owing to the thickness of the electrode film require at least a 6 h charging period and are therefore low in specific power. In the present study, the electrode films found optimal for high power were at most ~1 mm for AC and 0.5 mm for LMO and thus are $\sim 6 \times$ thinner than those for high energy density. Considering that this represented the 100 mg loading density used in the previous section, the double

sided loading used on large format cells might provide the higher power performance of a 50 mg loading density given the halving of the electron pathway. Therefore, the following studies began by examining the effect of double-sided electrode film loading on large format electrodes. Then, having established the specific capacity of these electrodes, the material quantities for a 3 Ah cell were determined and the cell was constructed and tested.

4.4.1 Testing large-format electrodes

The following experiments investigated the performance of AC and LMO at high power in large-format electrodes. The sizing and design of the electrodes was based on the decision to use an upright parallel plate electrode configuration for the intended up-scaled 3 Ah cell. This cell format facilitated strong electrode tab connections using bolts instead of welding (which can weaken stainless steel and accelerate its corrosion). The details of electrode construction and cycle testing are described below.

4.4.1.1 Experimental

- *Determination of electrode size*

The previous tests on loading densities of active materials revealed that different options exist regarding the choice of current density and cell voltage for obtaining a specific energy and specific power on the 50:1 P/E ratio line. These variables determine the active material quantity to obtain a specified amount of energy or power. The present study chose the capacity of 3 Ah (at 50:1 P/E) for the up-scaled cell target capacity. Table 4.5 shows how the amount of active used to obtain this capacity at 50:1 P/E is dependent on the cell voltage and loading density of the active materials. The table shows that at 2.2 V the cell would use ~33% less materials than at 1.8 V owing to the higher specific energy obtainable at this voltage.

	Specific properties				3 Ah cell properties					
*Options (with 50 mg loading)	Active material (mAh/g)	Active material (Wh/kg)	Total cell P/E (Wh/kg: W/kg)	Active material (mA/g)	Active material (g)	Current collector (cm ²)	Max current (A)	Mass (g)	Energy (Wh)	Power (W)
1.8 V	~17	15.46	4:200	800	176.5	7,058.8	150	682.5	2.73	136.5
2.2 V	~25	23.39	6:300	1200	120	2,400	150	468.3	2.81	140.4

*50 mg loading refers to 50 mg total active materials between two 1 cm² current collectors

Table 4.5 Effect of cell voltage on material quantities for a 3 Ah high power cell at 50:1 P/E.

Although Table 4.5 provided a guideline of the material quantities involved, it was of interest to determine whether higher loading density could be used for double-sided loading of electrode film on current collectors. To test this possibility, electrodes were constructed at ~100 mg loading density as described below.

- *Electrode construction*

The electrodes comprised the previously used 304 stainless mesh current collectors and 85:10:5 electrode dough. Square sections of current collector were cut to form a coating area for the film of 7.5×7.5 cm (~56.25 cm²). An uncoated tab connection area of ~4 cm² was left at the top of the current collector for the attachment of the ‘bus bar’ bolt, onto which more electrodes could be later threaded (Fig 4.17). AC and LMO electrode dough was prepared and pressed into both sides of the current collectors. To obtain an active material loading density of ~100 mg, AC and LMO dough was rolled to 1 mm and 0.5 mm thick films respectively using a measured setting on the rolling machine. The sheets were then dried for 2 h at 100°C and cut to measure the current collectors. The inward facing side of each electrode film was then brushed with

isopropanol to facilitate adhesion and pressed at 100 kg/cm^2 into the current collectors for 5 min, using a 10-tonne shop press. The electrodes were then trimmed to remove excess film from their edges and then dried overnight at 100°C .

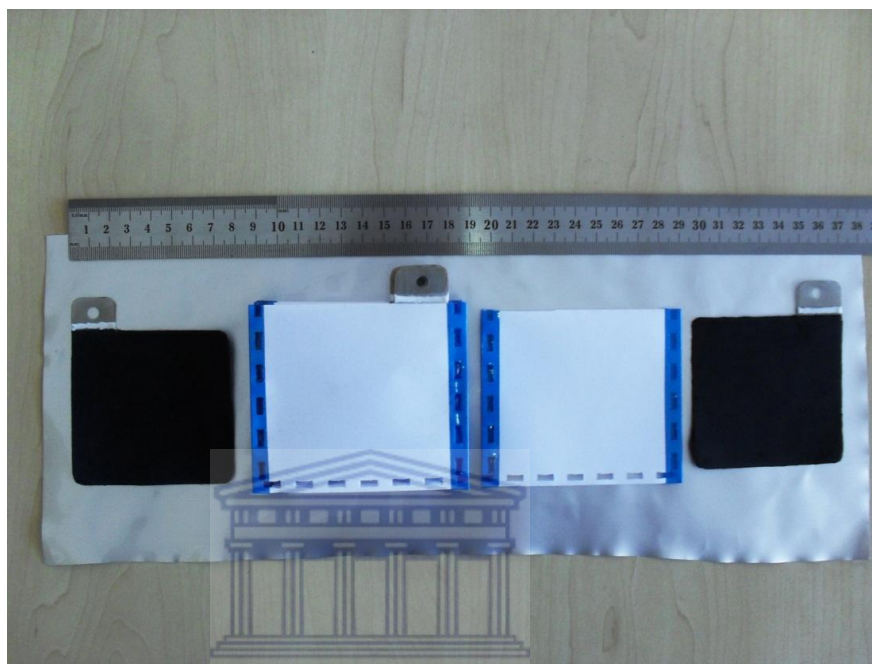


Fig 4.17 Large-format (100 mg loading density) electrodes tested for the 3 Ah (50:1 P/E) power cell, showing paper sleeve separators and tab connection points for the bolted bus bar.

- *Cell assembly and galvanic testing*

The electrodes were laid flat on a square plastic fastening plate and placed in a large glass petri dish with one of the electrodes slotted inside a paper sleeve envelope as a separator (Fig 4.16). Each electrode was then fastened to a vertically positioned stainless steel bolt running through the fastening plate and the electrode secured with two tightened nuts and washers. The bolts were then connected to the clips of a 1 – 100 A LAND® battery tester, and the electrode assembly flooded with 1 M $\text{Li}_2\text{SO}_4(\text{aq})$ electrolyte. The AC/LMO electrode pair, for the $\sim 57 \text{ cm}^2$ area had a total mass of $\sim 5.7 \text{ g}$ ($\sim 6 \text{ g}$) active material. Galvanic cycling was carried out using current densities of 600, 800, 1000, 1200 and 1400 mA/g to span the 50:1 P/E ratio, and charging voltages of 1.8 and 2.2 V were compared.

4.4.1.2 Results and discussion

Fig 4.18 and Fig 4.19 (overleaf) show galvanic cycling plots of the large-format AC/LMO electrodes with 100 mg active material loading density. The plots show that at the 50:1 P/E ratio the electrodes produced marginally lower voltage drop and higher cell total specific energy than the same loading density used previously in the thickness test cells. Fig 4.18 shows the plotted values in terms of cell total figure, i.e. considering a 62% yield from the active materials according to its mass percentage of the cell total mass. Here, the 100 mg loading density charged to 2.2 V produced nearly 10 Wh/kg at the 50:1 P/E, which is ~2 Wh/kg higher than the target figure of 8 Wh/kg. However, although the energy efficiency was higher by ~8% than for 100 mg loading density in the thickness test cells, its value of ~50% is still quite low. Cell charging to 1.8 V in the large format cell also produced marginally higher specific energy than the corresponding thickness cell test, with slightly higher energy efficiency, 53%, than the 2.2 V cell charge probably due to lower losses in coulombic efficiency.

4.4.1.3 Conclusions

Galvanic cycling of large format electrodes with ~100 mg loading density produced ~10% higher specific energy than the same loading density in the previously studied thickness test cells. This may be due to the double sided loading of electrode film on the current collectors, which suggests that this format of electrode should be used for future test purposes on electrode loading density. The capacity values of the large-format electrodes provided a basis on how many electrodes would be required for the 3 Ah cell (see next Section 4.4.2).

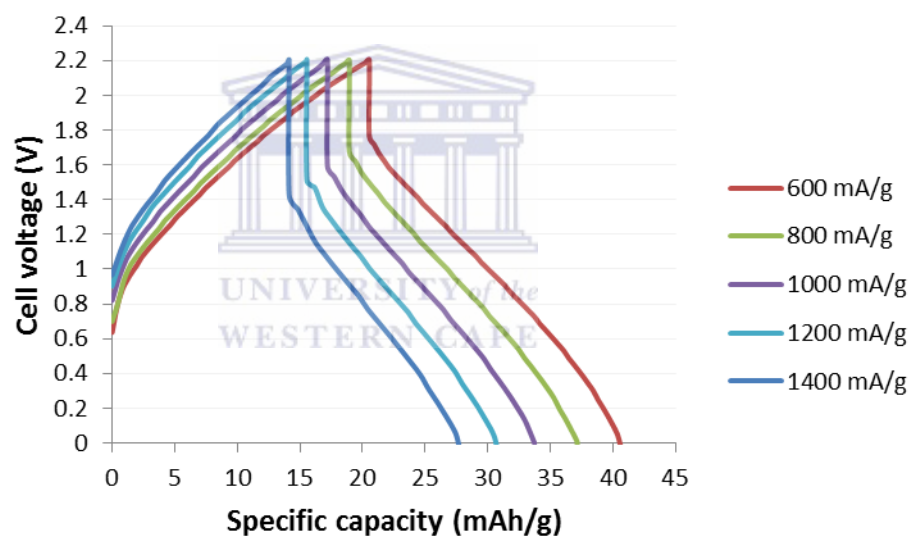
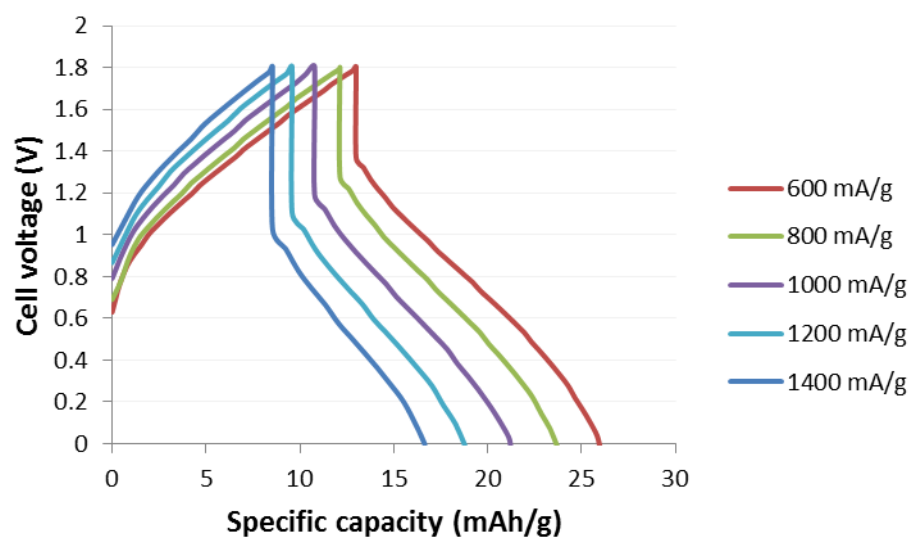


Fig 4.18 Large-format (100 mg loading density) AC/LMO electrodes cycled at 600 – 1400 mA/g to 1.8 V charge (above), and 2.2 V charge (below).

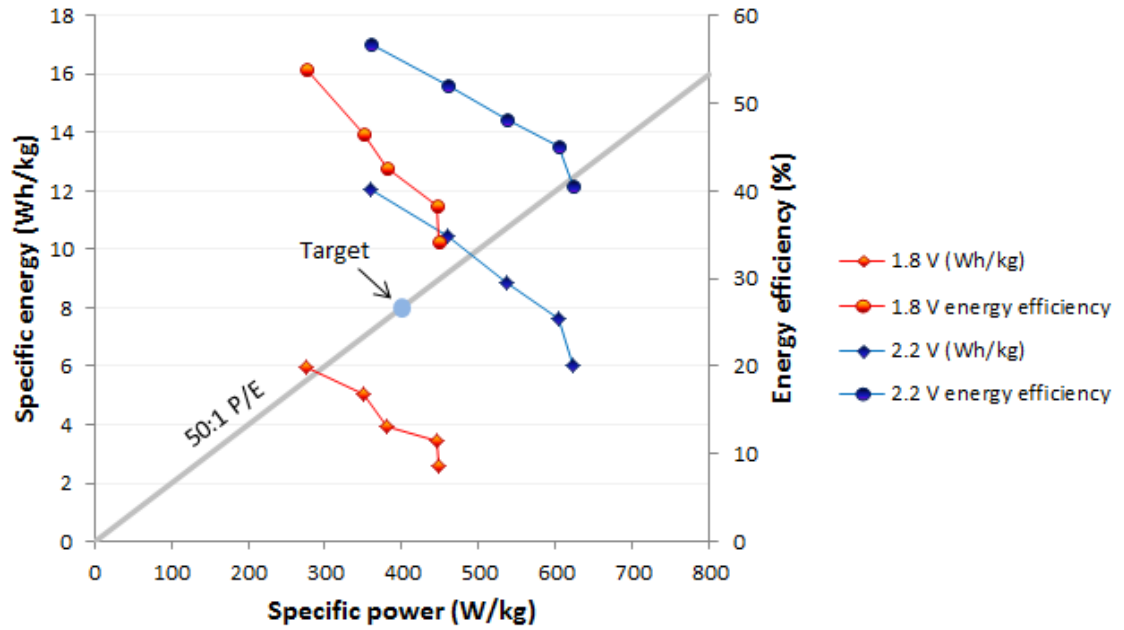


Fig 4.19 Total cell specific energy and specific power of large-format AC/LMO electrodes with 100 mg loading density cycled at 600 – 1400 mA/g to 1.8 V charge and 2.2 V charge.

4.4.2 Construction and cycling of a 3 Ah cell

Using the specific capacity values of the large-format electrodes at ~50:1 P/E ratio, the two options for total number of electrodes and for the 3 Ah cell were as follows:

- Using a 1.8 V charge at 600 mA/g (P/E 46:1):

Average cell discharge voltage:	0.78 V
Specific capacity of active materials:	~13 mAh/g
Current used for electrode pair (active material):	$5.7 \text{ g} \times 600 \text{ mA/g} = 3.42 \text{ A}$
Capacity of electrode pair (active material):	$5.7 \times 13 \text{ mAh/g} = 74.1 \text{ mAh}$
Total electrodes (3000 mAh):	$2 \times (3000/74.1) = 80.97$
Total active material (3000 mAh):	$(80.97 \times 5.7 \text{ g})/2 = 230.75 \text{ g}$
Total current for 3 Ah cell:	$3.42 \text{ A} \times (80.97/2) = 138.45 \text{ A}$
Total cell energy:	$3 \text{ Ah} \times 0.78 \text{ V} = 2.34 \text{ Wh}$
Total average cell power:	$138.45 \text{ A} \times 0.78 \text{ V} = 107.95 \text{ W}$
Estimated total cell specific properties:	6.36 Wh/kg; 293.4 W/kg

- *Using a 2.2 V charge at 800 mA/g (P/E ~40:1):*

Average cell discharge voltage:	0.95 V
Specific capacity of active materials:	~19 mAh/g
Current used for electrode pair (active material):	$5.7 \text{ g} \times 800 \text{ mA/g} = 4.56 \text{ A}$
Capacity of electrode pair (active material):	$5.7 \times 19 \text{ mAh/g} = 108.3 \text{ mAh}$
Total electrodes (3000 mAh):	$2 \times (3000/108.3) = 55.5$
Total active material (3000 mAh):	$(55.5 \times 5.7\text{g})/2 = 158.18 \text{ g}$
Total current for 3 Ah cell:	$4.56 \text{ A} \times (55.5/2) = 126.45 \text{ A}$
Total cell energy:	$3 \text{ Ah} \times 0.95 \text{ V} = 2.85 \text{ Wh}$
Total average cell power:	$126.45 \text{ A} \times 0.95 \text{ V} = 120.13 \text{ W}$
Estimated total cell specific properties:	11.32 Wh/kg: 426.36 W/kg

Therefore, in terms of using matching numbers of anodes and cathodes the above two options equate to 80 electrodes for 1.8 V and 56 electrodes for 2.2 V charge. Given the large difference between the numbers, an intermediate number of electrodes of 60 was chosen (comprising 30 anodes and 30 cathodes), which could also cater for higher testing of current densities at 2.2 V.

UNIVERSITY of the
WESTERN CAPE

4.4.2.1 Experimental

- *Cell construction*

Electrode dough was prepared and processed into electrode film for $30 \times \text{AC}$ anodes and $30 \times \text{LMO}$ cathodes. The films were pressed into large-format current collectors as previously described in Section 4.4.1. Fig 4.20 shows the stacking arrangement of the electrodes with alternate paper sleeve separators, with the bolt bus bars and washers, and the final electrode assembly bound in PTFE tape to provide assembly pressure on the electrodes. The cell was placed in a clear plastic Ziploc® bag with two holes sealed by rubber washers for the anode and cathode bus bar bolts to pass through. The bag was flooded with 150 ml 1 M Li_2SO_4 (aq) electrolyte and the electrodes were soaked for 24 h. Fig 4.21 shows the cell in its final plastic casing measuring $\sim 10 \times 10 \times 5$ cm, and its electrode connections to battery cycling machine.

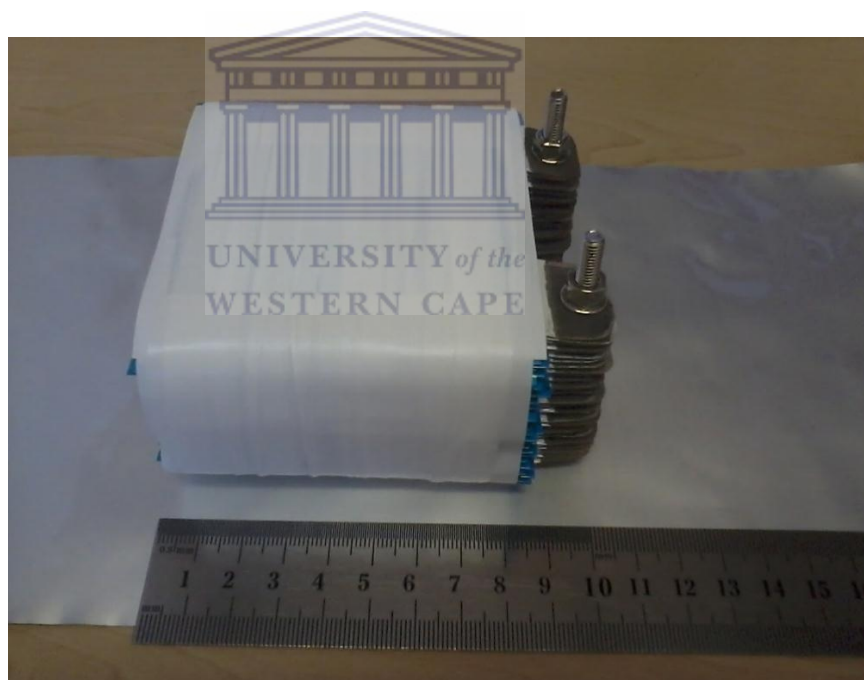
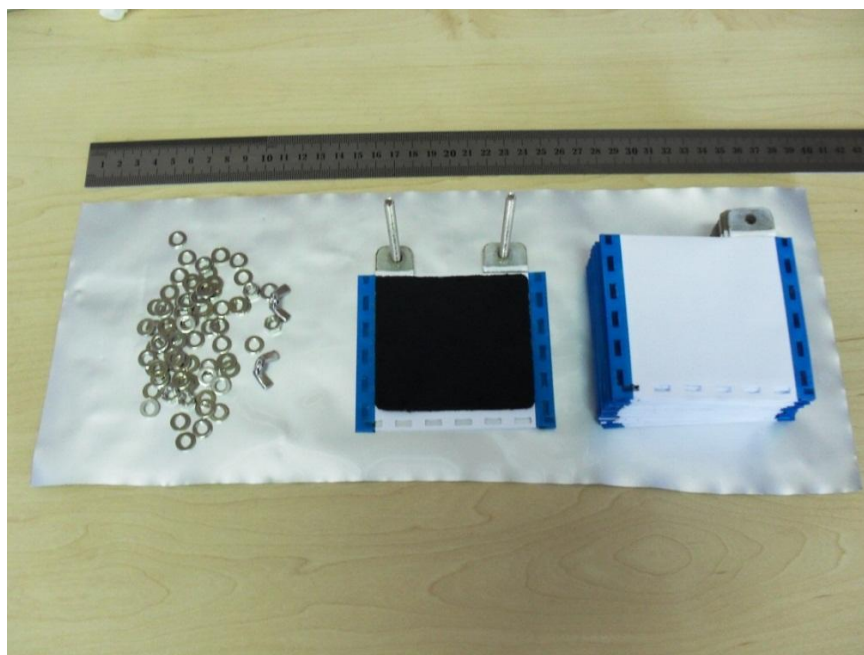


Fig 4.20 Electrode assembly of the 3 Ah cell, showing bolt bus bar and paper sleeve separators (above), and final 60-electrode assembly wrapped in PTFE tape (below).



Fig 4.21 Final assembly of the 3 Ah cell in casing (above), and connection to the battery cycling machine (below). The cell measured $\sim 10 \times 10 \times 5$ cm (500 ml) and had a total mass of ~ 747 g.

On final assembly the total cell mass and masses of its respective components were as shown in Table 4.6

Components	Mass (g)
Current collectors	220
*Electrode film (AC + LMO)	201
Electrolyte 1 M Li_2SO_4 (aq) (150 ml)	167
Washers, nuts and bolts	105
Paper separator and packaging	54
Total	747

*Electrode film (85% mass active material):

AC + LMO = 171 g

AC = 114 g

LMO = 57 g

Carbon black (10%) = 20.1 g

PTFE (5%) = 10.05 g

Table 4.6 Total mass and component masses of the 3 Ah cell on final assembly

- *Galvanic cycling*

Galvanic cycling of the 3 Ah cell was carried out using 200 A LAND® battery cycling machine. Considering the results for the large-format electrodes, the current densities of 600 mA/g for 1.8 V and 800 mA/g for 2.2 V produced P/E ratios close to 50:1. Therefore, for the cell's ~200 g of active material, these current densities equate to ~120 A and 160 A respectively. The highest available current density available from the cycling machine was 200 A or 1000 mA/g for 200 g of the active material. Therefore, a range of 100, 200, 400, 600, 800, 1000 mA/g could span 20 to 200 A, comparing 1.8 and 2.2 V charging.

4.4.2.2 Results and discussion

As a safety measure, the cell was first cycled at 1.8 V charge using a low 3 A current (~15 mA/g). This measure was to ensure that all 60 electrodes had sufficiently low resistance contact with the bolt busbars prior to galvanic cycling at high C rates (requiring very high current). Fig 4.22 shows the voltage/time plot of the 3 A current

produced, which produced a surprising low capacity of only 2.6 Ah at this current density over 48 min or 1.25 C. Given that slow charging (at 25 mA/g) of AC/LMO in small test cells produced ~23 mAh/g (Section 4.2.3), the equivalent capacity for 200 g of active materials would be 4.6 Ah, and the theoretical current to obtain this capacity over 1 h or 1 C would be 4.6 A. Therefore, the result showed that only 56% of the 200 g of active materials' anticipated capacity was accessed, resulting in an active material specific capacity of only 12.5 mAh/g.

To investigate the cause of the low capacity, the cell was unwrapped from its PTFE tape binding and the electrodes allowed to soak overnight in the absence of assembly pressure. On reassembly, the busbar bolts were tightly secured and the electrolyte levels in the cell checked to ensure full coverage of the electrodes. However, these measures failed to significantly improved the performance of the cell. Suspecting that some form of resistance was responsible for the low capacity, the busbar bolts, nuts and washers were replaced by an equivalent set made from lower resistance nickel-plated mild steel. Galvanic cycling of the cell at 3 A produced a marginally improved 2.9 Ah capacity of 63% of the 200 g or ~14.5 mAh/g. The results indicated that the large-format cell size had cumulative resistance at its multiple electrode contact points which seemed to significantly reduce the available capacity accessible from the electrodes' active materials. Further cycling of the cell at higher current densities produced the expected drop in capacity owing to increasing electrode polarization and voltage drop. Fig 4.22 shows the cycling plots of increased current of 10 and 30 A, which produced a proportional voltage drop in accordance to the increased density. Lastly, an overnight cycling experiment of the cell at 3 A current caused a dramatic drop in cycling efficiency with an accompanied loss of capacity retention. On inspection of the cell, prolific corrosion of the nickel-plated busbar bolts, nuts, and washers had occurred (Fig 4.24), which unfortunately caused irreparable damage to cells electrodes through rust contamination.

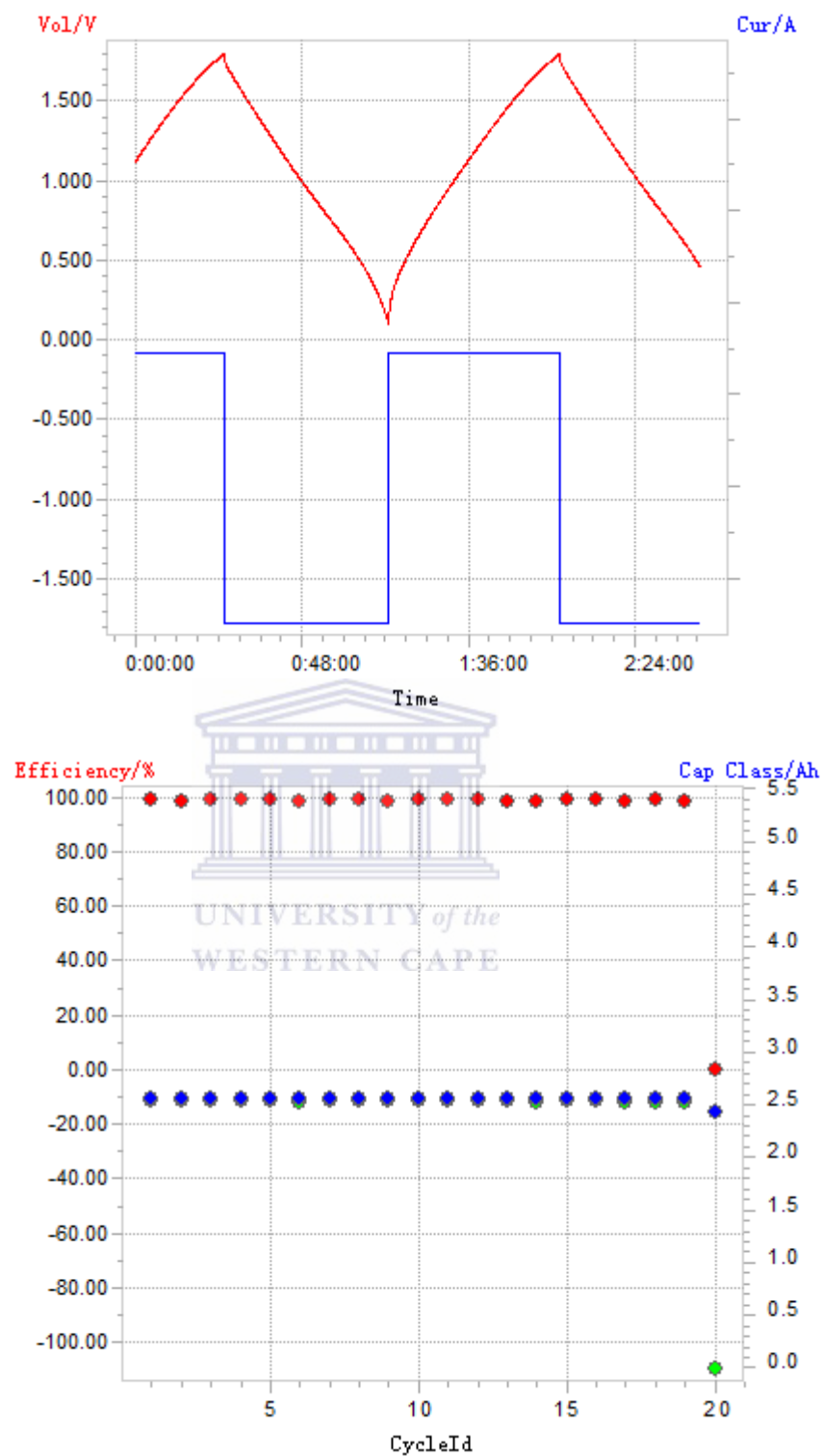


Fig 4.22 Galvanic cycling of the of the 3 Ah cell at 3 A showing the less than 4.6 Ah anticipated capacity of 2.6 Ah

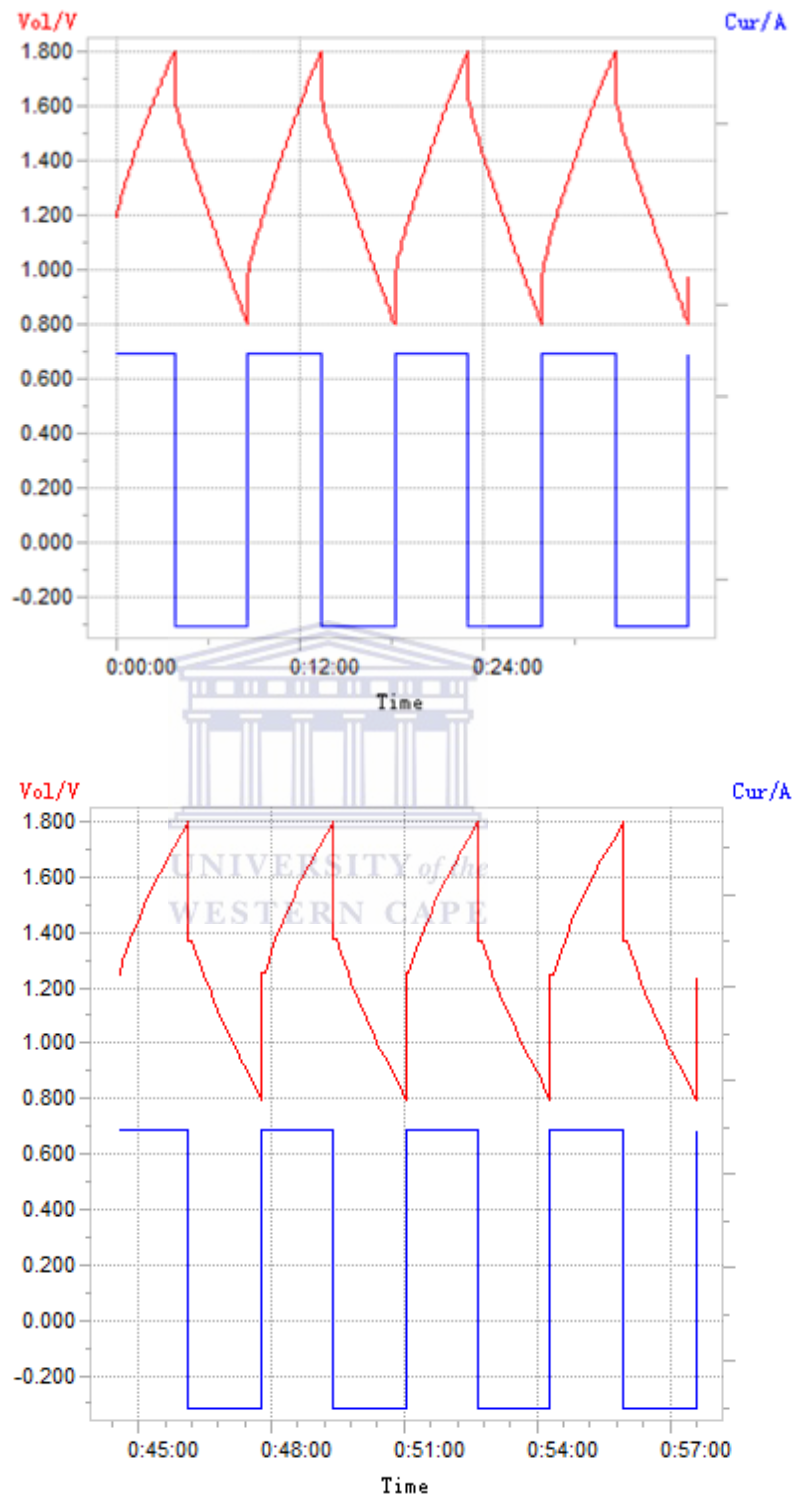


Fig 4.23 Galvanic cycling of the 3 Ah cell at 10 A (above) and 30 A (below) showing voltage drop



Fig 4.24 Corrosion of the nickel-plated bolt busbars, nuts and washers after overnight cycling of the 3 Ah AC/LMO at 3 A

4.5 Conclusions

The work presented in this chapter explored a variety of aspects concerning the viability and development of the aqueous AC/LMO cell format in high power applications. Galvanic cycling revealed that doublings of electrode film loading density increased electrode polarization and voltage drop to similar levels as doublings in applied current density. To sufficiently offset the mass contribution of current collectors required at least 50 to 100 mg active material between an electrode pair. However, these loading densities produced between 50-60% of the specific energy and specific power estimated from thin film studies at the 50:1 P/E ratio of interest for FCEVs. The reduction was caused by high polarization and voltage drop on the LMO electrode due to reduced electron conductivity and ionic transport in the thick-film loading densities. However, the study also found that these effects could be mitigated by increasing the charging voltage from 1.8 V to 2.2 V. Galvanic cycling on large-format electrodes using a 100 mg loading density of active materials with a 2.2 V charge did produce the 50:1 P/E FCEV battery target figure of 8 Wh/kg:400 W/kg compared to 6 Wh/kg:300 W/kg at 1.8 V charge with minimal extra loss of <5% energy efficiency. Finally, construction and galvanic cycling of up-scaled 60-electrode cell of 3 Ah (theoretical capacity at 50:1 P/E) revealed important issues concerning large-scale cell design and resistance at electrode connections to the busbar. The cell produced only 63% of the capacity expected from a low starting current density of 15 mA/g and irreparably rusted on account of using nickel-plated mild steel in an attempt to improve the conductivity of the busbar.

Chapter 5

Development of a PbSO₄/LMO cell

5.1 Introduction

Section 2.6 of this thesis proposes a novel PbSO₄/LMO cell comprising a PbSO₄ anode and an LMO cathode in 1 M Li₂SO₄ electrolyte. Strong evidence suggests that the charge/discharge reaction of the Pb/PbSO₄ anode in Pb-acid batteries [52] occurs in an analogous manner at pH 7 in sulphate-containing electrolyte over the same standard potential range [40]. Using the practical specific capacity values of LMO and PbSO₄ from their respective traditional cell formats, the calculated specific energy of the PbSO₄/LMO cell's active material is 70 Wh/kg and 45 Wh/kg for a 65% practical cell value. The practical cell value is almost double that of the AC/LMO Aquion® cell at 23 Wh/kg [4] and similar to that of Pb-acid batteries [17]. Furthermore, the theoretical cost/kWh of the cell is the same as Pb-acid cells (\$150/kWh) [2] but has the advantage of using close to 3 × less Pb. Considering the current importance of Pb-acid cells and their potential for bulk EES applications, the use of nearly 3 × less Pb for the same cost/kWh of storage would have considerable commercial implications.

This chapter presents an investigation of the above system considering the theoretical figures as potential targets for the research. The presented work includes: Material synthesis and characterization of PbSO₄ anode material (Section 5.2), electrochemical characterization (Section 5.3), carbon-coating of PbSO₄ (Section 5.4), thick-film cycling (Section 5.5) and overall conclusions to the chapter (Section 5.6).

5.2 Synthesis and characterization of PbSO₄ micro-particles

5.2.1 Introduction

Although PbSO₄ is the reversible discharge product of Pb-acid batteries, its low electrical conductivity is a contributing factor of their short lifespan of ~500 – 1,000 cycles [58]. The phenomenon known as “sulphation” occurs when the battery is held for long periods in the fully discharged state, and is characterized by the formation of large PbSO₄ crystal formations (>100 µm) of high electrical resistance [59, 60]. Therefore, in electrode material preparation it is important to obtain a small, even, starting particle size of material to ensure sufficient electrical conductivity. In the manufacture of Pb-acid battery electrodes, small particle size is achieved using very finely ground “leady oxides” that contain a complex mix of Pb and Pb oxides, which are heat cured on to Pb grid current collectors as a paste with H₂SO₄, and then formed by slow “electrode formation” charge cycles [61, 62]. The electrical conductivity of the Pb metal and PbO content plays an important role in the initial electrode formation during charging.

In place of heavy Pb metal grids, the present study aimed to use much lighter stainless steel mesh current collectors with pressed electrode film as the electrode material format. Here, a more facile method to prepare the electrode material was required to avoid corrosion of the steel at high temperature with H₂SO₄. Furthermore, the standard inclusion of conductive element (carbon black) at 10% material mass provided a substitute for the conductive Pb element to facilitate the direct use of PbSO₄ particles as electrode starting material. Therefore, in place of leady oxide, PbSO₄ micro-particles were synthesised using a simple precipitation method, where saturated solutions of Pb(NO₃)₂ and a low cost source of sulphate, Na₂(SO₄), were mixed to precipitate colloidal PbSO₄ micro-particles (see below).

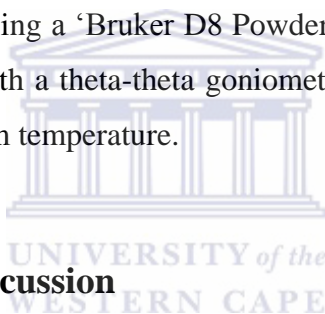
5.2.2 Experimental

5.2.2.1 Preparation of PbSO_4 micro-particles

50-ml saturated solutions of $\text{Pb}(\text{NO}_3)_2$ and Na_2SO_4 (Sigma-Aldrich) were prepared with de-ionized water and mixed together by drop-wise addition with vigorously stirring for 10 min. The resultant white precipitate of PbSO_4 was filtered and washed twice in de-ionized water to remove residual soluble reactants. The final product was dried at room temperature and then ground with a pestle and mortar to form a fine powder.

5.2.2.2 Material characterization of PbSO_4 micro-particles

Morphological studies were carried out using high-powered SEM and TEM (with Au coating to ensure conductivity) on a ‘Zeiss Gemini Auriga field emission microscope’ and ‘Tenai G² F20 X-twin MAT 200 kV Field Microscope’ respectively. EDS elemental analysis was carried out on the above-mentioned instruments, and crystal structure identification by XRD using a ‘Bruker D8 Powder Diffractometer’ (Ithemba labs, Cape Town, South Africa) with a theta-theta goniometer using $\text{Cu K}\alpha$ radiation operated at 40 kV and 35 mA at room temperature.



5.2.3 Results and discussion

Fig 5.1 ‘A, B’ shows SEM images of the prepared PbSO_4 micro-particles. The particles had smooth-edged angular morphology with an average size distribution of $\sim 0.2 - 1 \mu\text{m}$. Under TEM imaging (Fig 5.2 ‘A–D’) the micro-particles appeared to comprise closely bound agglomerations of much smaller nano-particles of $\sim 5 \text{ nm}$ with definable edges and observable polycrystalline lattice fringes. However, no detached nano-particles appeared outside the micro-particles, despite the inclusion a 15-min sonication step for TEM sample preparation, which indicates their tightly bound nature. EDS analysis (Fig 5.3) confirmed the presence of the elements Pb, S and O, with no evidence of nitrogen contamination from unreacted $\text{Pb}(\text{NO}_3)_2$. XRD (Fig 5.3) confirmed the presence of PbSO_4 crystal structure showing >70 matching 2θ peak positions ($10-75^\circ$) of orthorhombic “Anglesite” (highly crystalline PbSO_4) JCP2 pattern: 00-036-1461 (*).

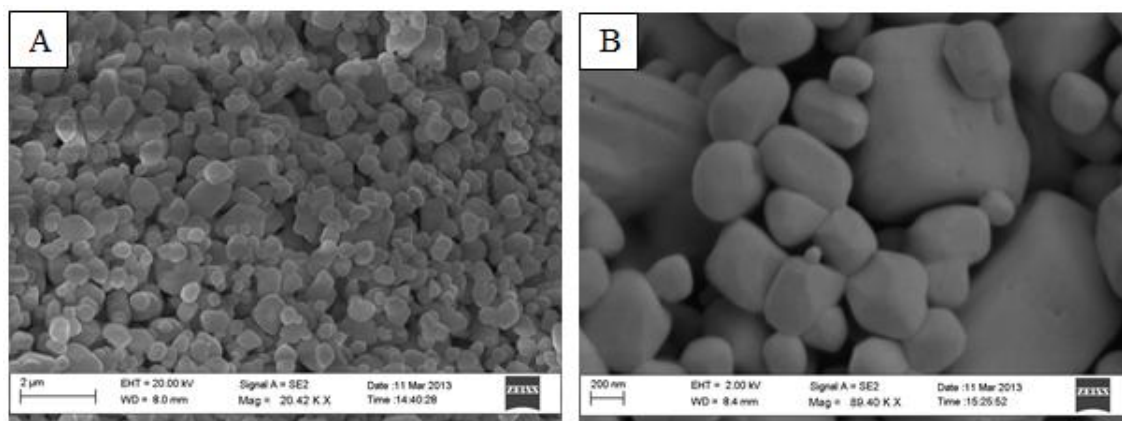


Fig 5.1 SEM images showing smooth-edged morphology of the PbSO_4 microparticles. ‘A’ low magnification (20 K) and ‘B’ high magnification (80 K).

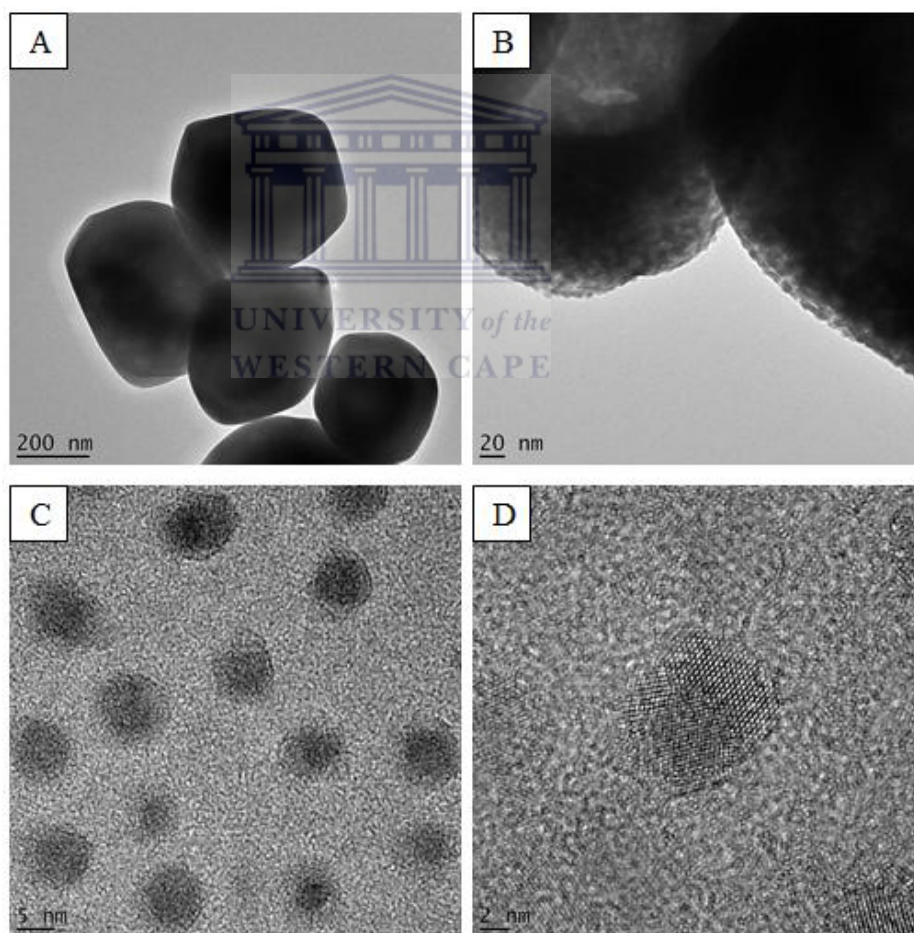


Fig 5.2 TEM images showing crystalline morphology of the PbSO_4 nanoparticle agglomerations. ‘A, B’ low resolution TEM, and ‘C, D’ HR-TEM.

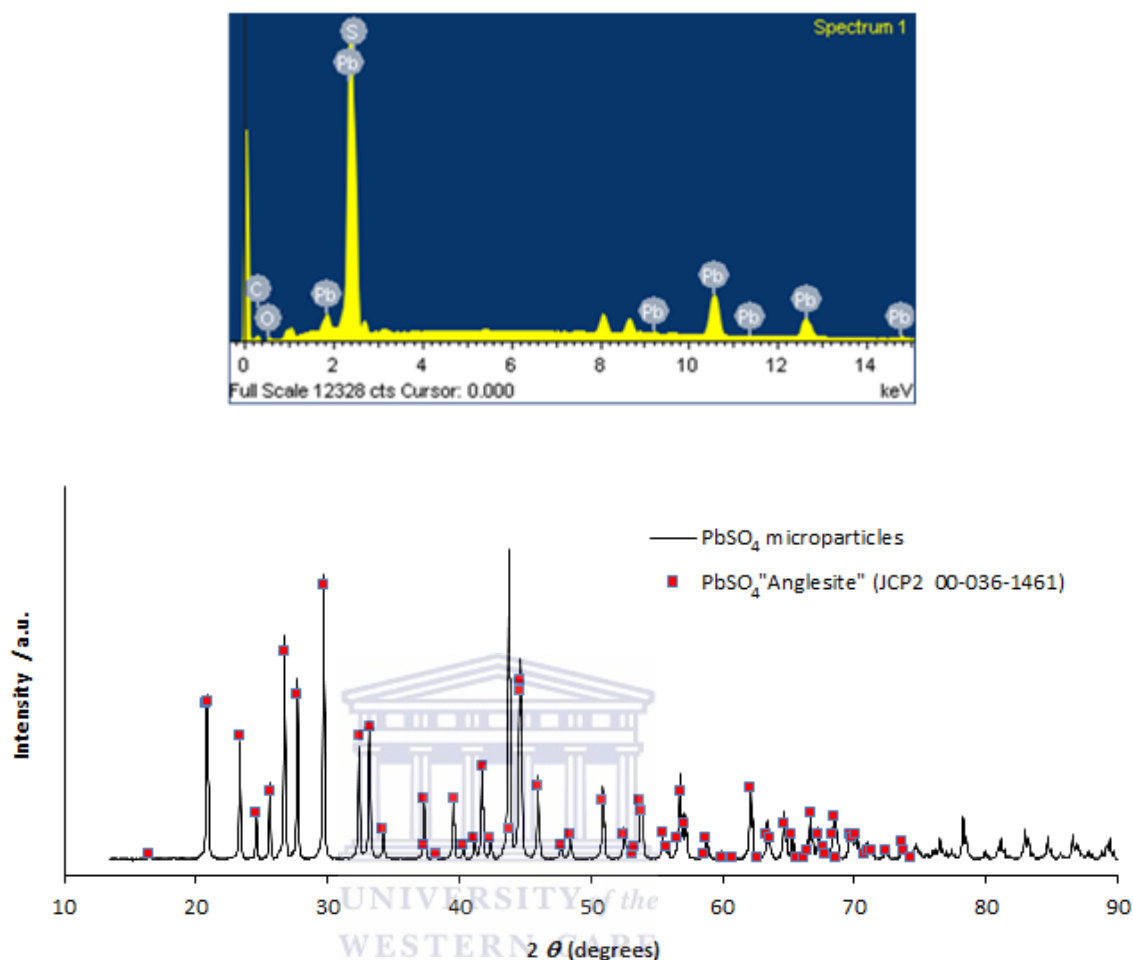


Fig 5.3 EDS spectrum (top) showing Pb, S and O element composition of PbSO₄ microparticles, and XRD pattern (below) of PbSO₄ micro-particles with ‘Anglesite’ crystal structure.

5.2.4 Conclusions

The method of PbSO₄ precipitation was simple, cost effective, and produced micro-particles of a 0.2–1.0 μm size range, with a substructure of tightly clustered polycrystalline nano-particles. The particle size met the goal of producing <10 μm PbSO₄ particles to avoid issues of poor conductivity affecting their possible performance as an anode material.

5.3 Electrochemical characterisation of PbSO₄ electrode film

To investigate the electrochemical and charge/discharge behaviour of the PbSO₄ microparticles, cyclic voltammetry and galvanic cycling were carried out respectively in 1 M Li₂SO₄ using thin-film electrodes (see below).

5.3.1 Experimental

5.3.1.1 PbSO₄ electrode preparation

PbSO₄ electrode film was prepared using an 85:10:5 mass ratio of PbSO₄ microparticles, SuperP-Li carbon black (Timcal), and PTFE (Dupont). The film was pressed into 80-mesh 304-Stainless steel (Alfa Aesar) current collectors at 12 MPa, at a loading density of 10 mg/cm² of current collector.

5.3.1.2 Cyclic voltammetry (CV) of PbSO₄ electrode film

For CV analysis, an open three-electrode cell was used and cycled using an 'Autolab electrochemical work station' (PGSTAT128N, Eco Chemie, The Netherlands). The three-electrode cell comprised: a working electrode of 10-mg PbSO₄ electrode film covering a 1 cm² area of 304 stainless steel mesh current collector in pH 6 (as prepared) 1 M Li₂SO₄ (aq) solution; an auxiliary electrode of 200 mg activated carbon electrode film covering ~4 cm² of current collector; and a saturated KCl 'calomel' (SCE) reference electrode.

5.3.1.3 Galvanic cycling of PbSO₄ electrode film

PbSO₄ electrodes (10-mg film) were cycled against 10-mg LMO counter electrodes in 1 M Li₂SO₄ (aq) electrolyte using a 'Neware (5 V, 10 mA)' battery cycler. SCE electrodes were used to monitor individual electrode potentials during cycling. Constant current densities and voltage ranges were determined according to CV analysis of redox peaks and on the basis of cell performance in initial cycle tests.

5.3.2 Results and discussion

5.3.2.1 Cyclic voltammetry on PbSO₄ thin film electrodes

Fig 5.4 shows the CV scan of a 10-mg PbSO₄ electrode film in 1 M Li₂SO₄ (aq) electrolyte at a 5 mV/second scan rate between -0.55 and +0.8 V vs SHE. The cathodic scan shows the characteristic current response between -0.325 and -0.5 V vs. SHE of Pb metal formation, and the anodic scan shows the reversibility of this reaction between -0.3 and 0 V vs. SHE, both of which occur over the same potential range in H₂SO₄ [52] and Na₂SO₄ (aq) [40]. The result suggests that neither the type of the counter cation present, (i.e. Li⁺, Na⁺ or H⁺) nor pH of the solution between ~pH 7 and pH 1 (i.e. Na⁺ and Li⁺ sulphates and H₂SO₄ respectively) has any significant effect on the reversibility of the Pb/PbSO₄ conversion reaction.

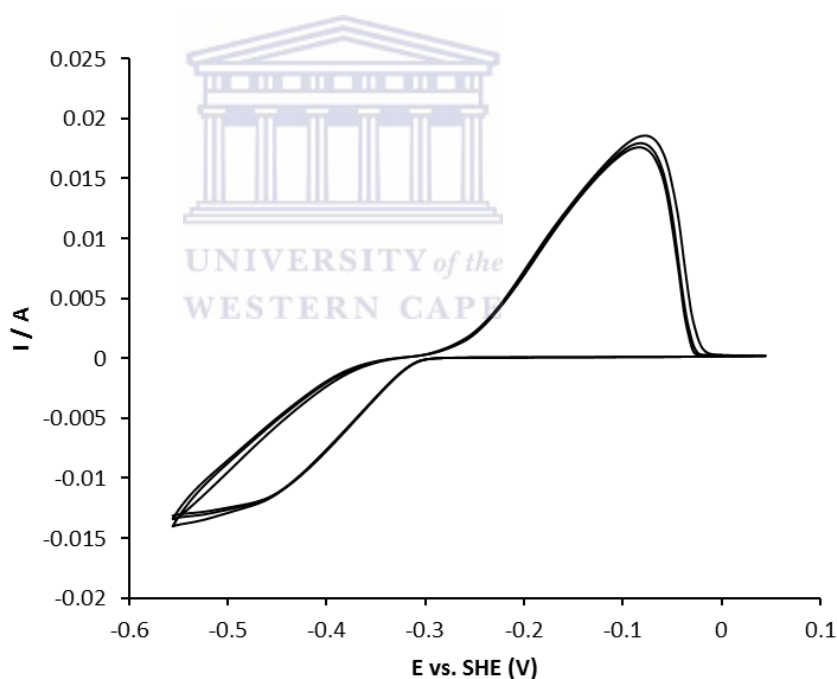


Fig 5.4 Cyclic voltammogram of Pb/PbSO₄ micro-particles in 1 M Li₂SO₄ (aq) at a scan rate of 5 mV/sec, showing reversible formation of Pb metal (anodic scan) and PbSO₄ (cathodic scan).

5.3.2.2 Galvanic cycling on PbSO₄ thin film electrodes

Galvanic cycling of the 10-mg PbSO₄ electrode film (containing 0.85 mg of PbSO₄ micro-particles) against a 10-mg LMO counter electrode was first carried out over a

programmed cycle range of 1.2 – 1.7 V at a current density of 0.05 A/g. Fig 5.5 shows the voltage/time cycling pattern of: PbSO₄ vs. SHE (top); LMO vs. SHE (middle) and

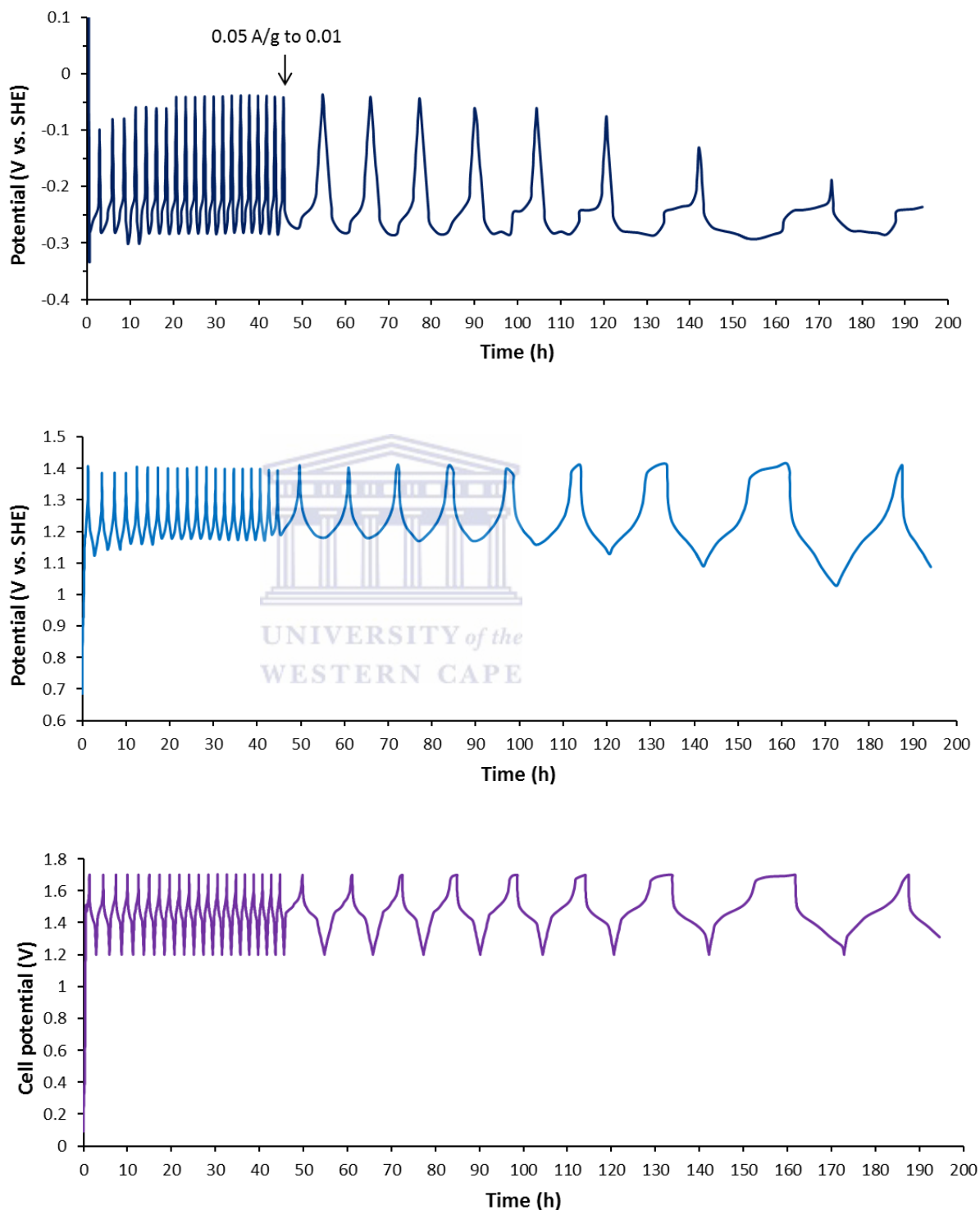


Fig 5.5 Galvanic cycling of a PbSO₄/LMO cell at 0.05 – 0.01 A/g (1.2-1.7 V), showing respective electrode voltages of: PbSO₄ anode (top), LMO cathode (middle) and cell (bottom).

PbSO₄/LMO cell (bottom). After ~45 h of cycling (20 cycles at ~ 1.1 C) the current density was reprogrammed from 0.05 to 0.01 A/g. The applied 5-fold drop in current density caused a gradual increase in the charge/discharge capacity from ~40 to 75 mAh/g accompanied by a gradual flattening of the average charge/discharge voltage slope of PbSO₄ to ~ -0.3 V and ~ -0.25 V vs. SHE respectively (Fig 5.5). The rise in PbSO₄ capacity resulted in a rapid decline in the cell's reversible capacity due to the onset of oxygen evolution on the LMO electrode (visible as a plateau between ~155 - 165 h on the voltage charge slope of LMO, see Fig 5.5 (middle). The apparent overcharging of the LMO electrode (in this case to ~1.4 V vs SHE) resulted in loss of coulombic efficiency in the cell Fig. 5.6 (below). This appears to have occurred due to irreversible electrode polarization of the PbSO₄ electrode at the higher current density, which effectively held the LMO electrode potential above 1.2 V vs. SHE. Interestingly, it was only later noticed that in the very last cycle of the series, the LMO charge/discharge curve changed shape indicating that the steady rise in PbSO₄ discharge capacity began to allow the LMO electrode to fully discharge. Overall, the above results revealed that: (1) the PbSO₄/LMO cell had worked in the predicted voltage range, and (2) that establishing both the correct current density and electrode mass balancing were clearly important factors for optimal cell performance.

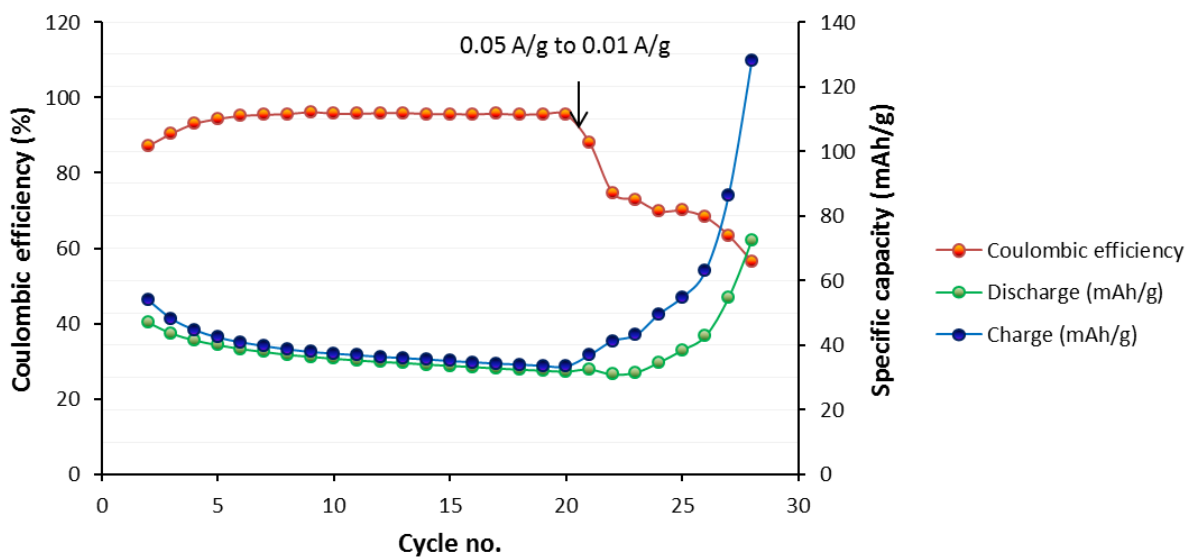


Fig 5.6 Effect of applied current density on the specific capacity and coulombic efficiency of PbSO₄/LMO.

5.3.2.3 Optimising electrode mass ratio

To optimise the performance of the PbSO_4/LMO cell, a range of cells with electrode mass ratios of 1:0.5, 1:0.8, 1:1 and 1:2 ($\text{PbSO}_4:\text{LMO}$) were cycling over a 1.2 to 1.7 V cell voltage range at charge/discharge rates between 0.2 - 0.1 C. Two important points to consider were: (1) for maximum energy gain, the potential of the LMO electrode during charging must reach its highest point (~ 1.2 V vs SHE) but also remain below the oxygen evolution potential, and (2) Pb/PbSO_4 should not discharge too far beyond the -0.2 V vs SHE plateau on the PbSO_4 electrode to prevent sulphation (i.e. large PbSO_4 crystal formation). Fig 5.7 shows the cycling profile of a 1:0.8 electrode mass ratio, where the peak charge potential of the LMO was optimal and the discharge of PbSO_4 controlled to the end point of the -0.2 V vs SHE plateau.

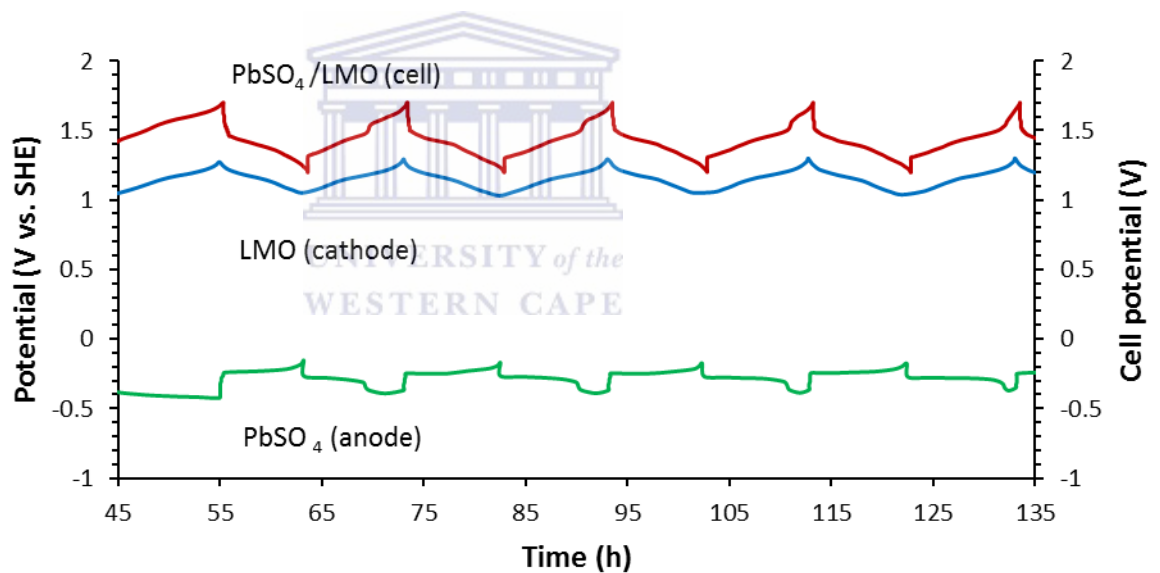


Fig 5.7 Cycling of PbSO_4/LMO at ~ 0.1 C with a 1:0.8 active material ratio

The above cell produced an average voltage of ~ 1.45 V and ~ 1.4 V on charge and discharge respectively. The specific discharge capacity of the cell's combined active materials was ~ 37 mAh/g with a specific energy of 52 Wh/kg. The specific discharge capacity of PbSO_4 was ~ 70 mAh/g and spanned a potential range -0.3 to -0.2 V vs SHE. Interestingly, the charging slope of the PbSO_4 electrode produced a secondary lower plateau at -0.4 V vs. SHE, comprising on average between 20 – 40% of the charge.

Considering the electrode's reversible capacity of >90% (discussed below), the lower charge plateau does not appear to amount to irreversible charge. No corresponding plateau appeared in the CV scan (Fig 5.4) and would thus appear to be a consequence of charge/discharge cycling. However, while the plateau appears to be reversible in terms of capacity, it creates a non-reversible higher cell voltage region on charging which reduces the energy efficiency of the cell to ~77%.

On long-term cycling the above cell for 40 days at 0.2 C, the specific capacity of PbSO₄ thin-film electrode dropped from ~70 mAh/g to ~60 mAh/g with no significant change in coulombic efficiency (Fig 5.8).

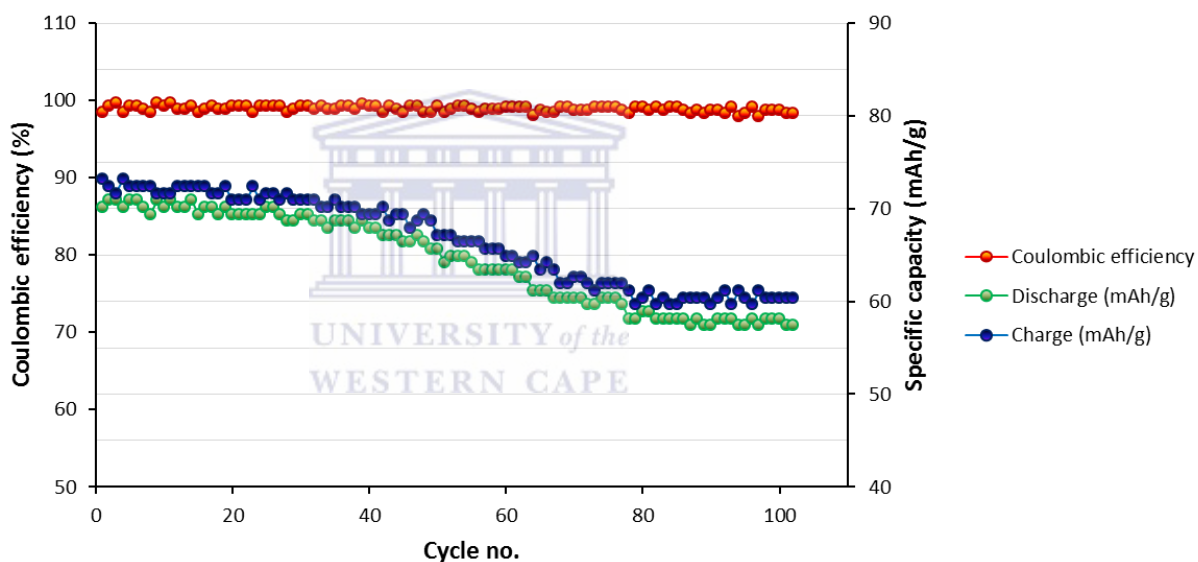


Fig 5.8 40-day cycling of 1:0.8 (PbSO₄/LMO) active material ratio at ~0.2 C. Specific capacity of PbSO₄ (right 'y' axis) and coulombic efficiency (left 'y' axis).

On inspection of the electrodes, a visible grey deposit had formed on the surface of the PbSO₄ film. Fig 5.9 'A – D' shows the SEM images of the surface, which comprised large (10 μm) plate-like crystalline growths. EDS analysis of the elemental composition of the growths (Fig 5.9) revealed a strong presence of Pb, but the angular morphology of the crystals are not characteristic of PbSO₄ sulphation [53] and could perhaps represent PbO or even elemental Pb growth. Regardless of the exact nature of the

crystals, their presence appeared to correlate with the specific capacity loss of the PbSO_4 electrode.

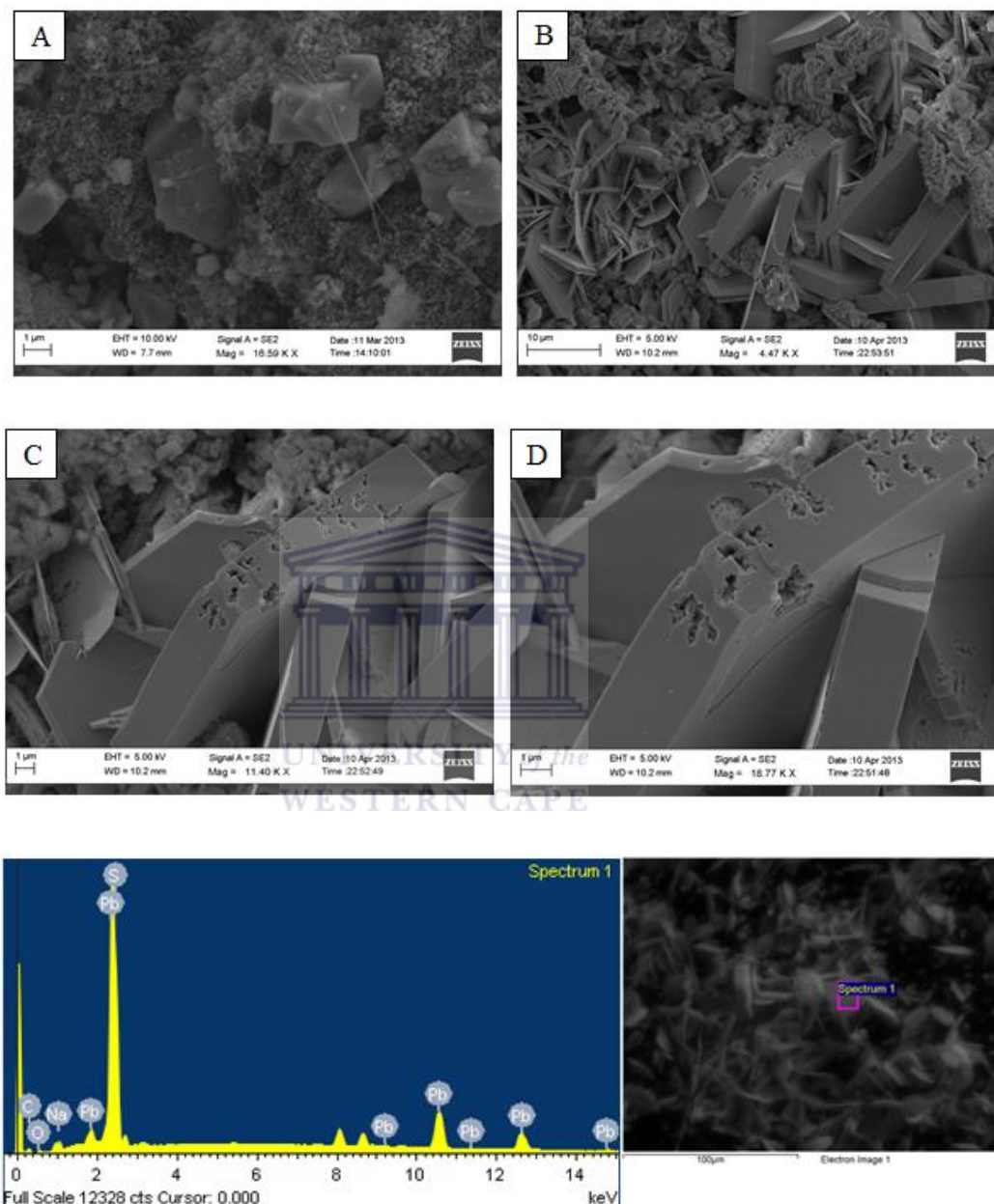


Fig 5.9 SEM images of PbSO_4 electrode films before and after 100 cycles at 0.2 C rate. 'A' pristine "un-cycled" electrode film, and "B-D" show a magnification series of the interesting crystal formations that developed after 100 cycles. Below: EDS spectrum the of surface showing strong presence of Pb.

5.2.3 Conclusions

The electrochemical behaviour of thin film PbSO_4 electrodes in 1 M Li_2SO_4 produced peaks for Pb/PbSO_4 formation over the same standard potential range of 0 to -0.4 V of that previously reported in Na_2SO_4 and H_2SO_4 electrolyte. Galvanic cycling of the PbSO_4 thin-film electrodes produced a 70 mAh/g specific discharge capacity at 0.2 C using an optimal mass loading ratio of 1:0.8 PbSO_4/LMO . The cell retained 80% of its initial capacity at high 98% coulombic efficiency over a two-week period comprising 100 cycles. Large Pb-containing crystalline growth deposits appeared on the surface of the PbSO_4 electrodes, suggesting the PbSO_4 microparticles lost their initial microparticle morphology during charge/discharge cycling, and that the loss of capacity is strongly associated with this process.

5.4 Carbon-coated PbSO_4 (ccPbSO_4)

The associated loss of specific capacity with the observed crystal growth on the PbSO_4 thin film electrodes suggested that the PbSO_4 microparticles quite rapidly lost their initial morphology during repeated charge/discharge cycles. In order to retain the microparticle morphology during cycling, the following study used a low cost carbon coating method to encapsulate the PbSO_4 particles. Furthermore, the carbon coating might also facilitate faster electron transfer and enable higher energy efficiency. The following work presents the synthesis, material characterization, and galvanic cycling performance of ccPbSO_4 .

5.4.1 Experimental

5.4.1.1 Preparation of Carbon coated PbSO_4 particles (ccPbSO_4)

3 g of PbSO_4 (as prepared in Section 5.2.2.1) was dispersed in distilled water and ethanol (1:3 v/v; 20 ml) to which a sucrose solution containing 0.5 g sucrose/10 ml distilled water was then added. The mixture was stirred for 10 min, concentrated to dryness at 80 °C and the dried powder fired at 600 °C in a tube furnace for different periods of time ranging from 1, 2, 5, 10 and 12 min in air. To observe the carbonization process, a separate sucrose/ PbSO_4 sample was concentrated to a slurry and evenly

spread on a stainless sheet that was then heated from below by a gas flame. Over a heating period of 1 min, colour changes from white to light-brown, to grey and back to white occurred suggesting that prolonged periods of heat completely oxidised the carbon to CO₂.

5.4.1.2 Material characterization, electrode preparation, and cycling of ccPbSO₄

SEM, TEM, XRD, electrode preparation and galvanic cycling were carried out as previously described (Section 5.2.2).

5.4.2 Results and discussion

5.4.2.1 Material characterization of ccPbSO₄

SEM images in Fig 5.10 show a clearly visible presence of carbon coating over clusters of the prepared PbSO₄ microparticles. The presence of the thick carbon layer was unique to samples that had a 5-min period of heating at 600°C, which were also light-brown as opposed to white, suggesting that longer periods of heating caused the samples to lose carbon through oxidation to CO₂ in air. The presence of the carbon layer was also visible by TEM (Fig 5.11) appearing as the lighter fringe area surrounding the particles. XRD analysis of ccPbSO₄ provided less compelling evidence of the carbon coating but under high magnification small variations in minor peaks are visible. The nature of these peak differences do not convincingly correspond to graphite card (JCP2 00-041-1487) and thus remain unidentified.

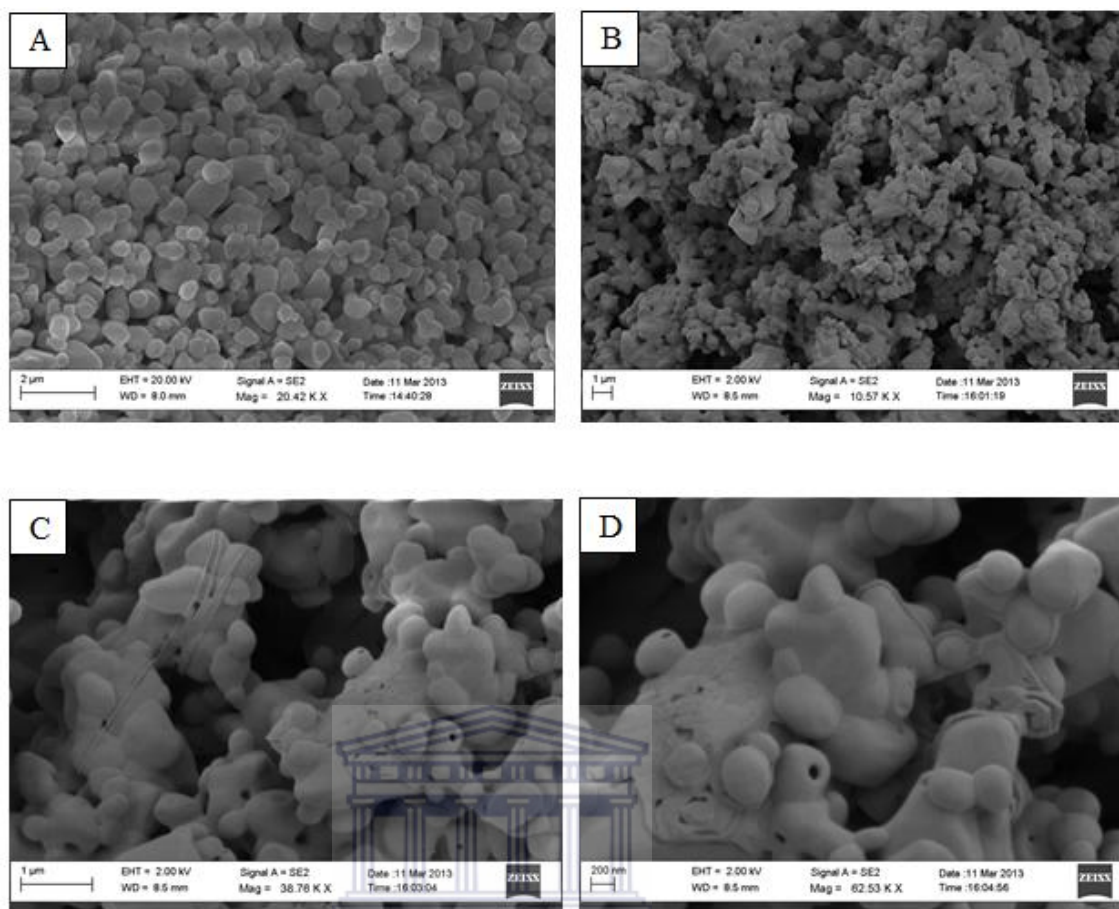


Fig 5.10 SEM images of ccPbSO₄ showing carbon coating. 'A' uncoated PbSO₄, 'B – D' 5-min heated cc PbSO₄ at increasing magnification.

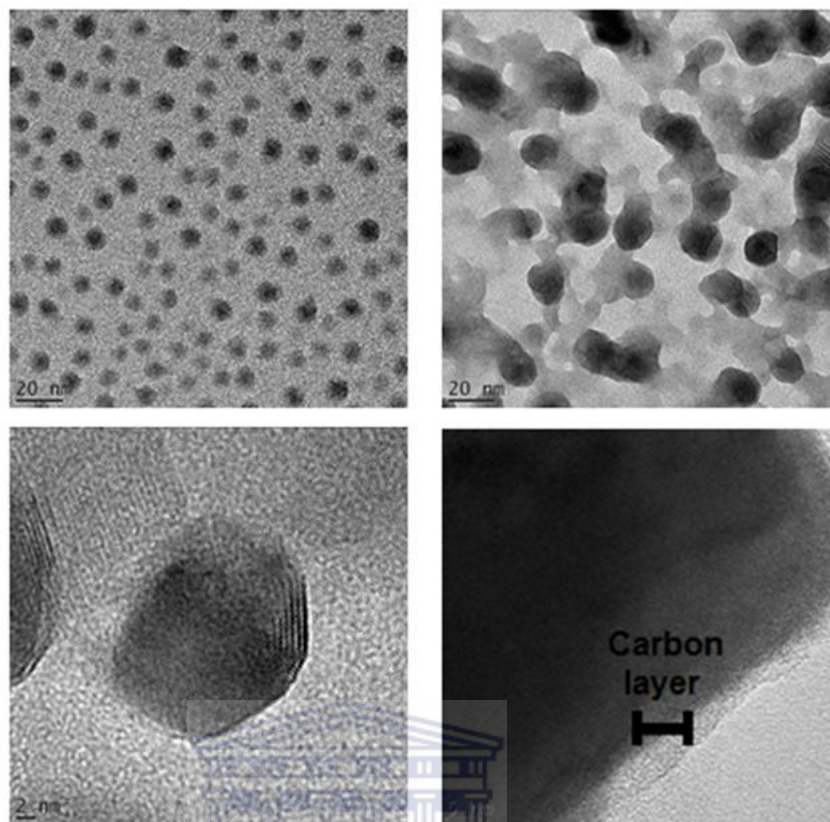


Fig 5.11 TEM images of ccPbSO₄ showing evidence of carbon coating (bottom right).

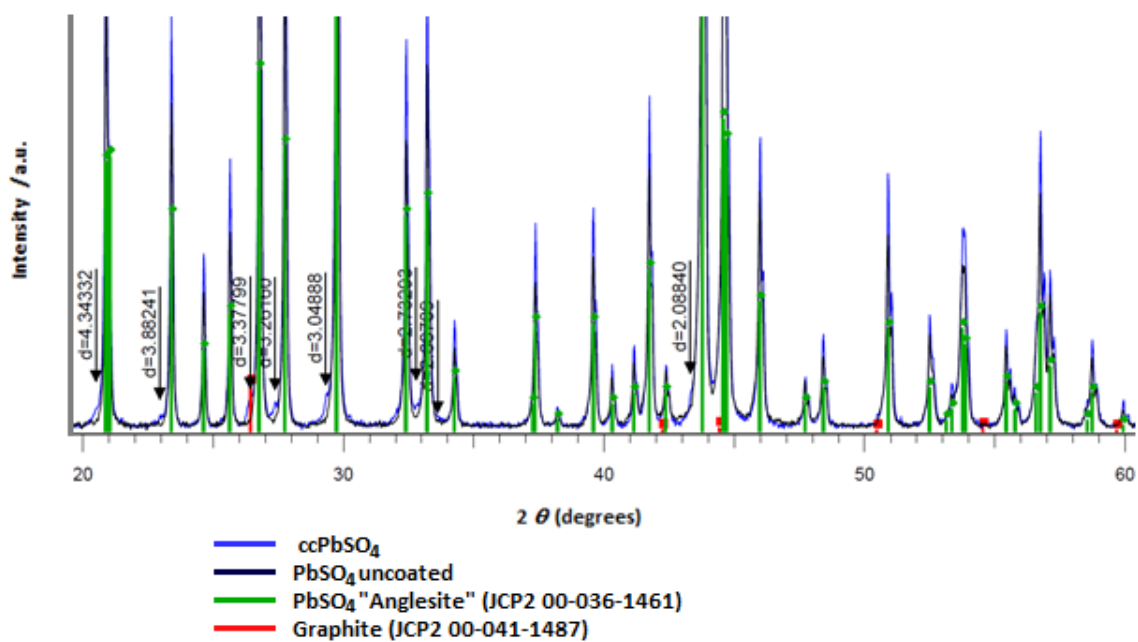


Fig 5.12 XRD plots of ccPbSO₄ and uncoated PbSO₄ showing differences in minor peaks and possible indication of graphitic carbon presence.

5.4.2.2 Galvanic cycling of ccPbSO₄

Thin (10-mg) film ccPbSO₄ electrodes were prepared and cycled between 1.2 and 1.6 V against LMO electrodes over a 0.1 to ~ 0.4 C rate cycle range. Fig 5.13 shows charge/discharge plot of the ccPbSO₄ electrode at 0.4 C, which produced a specific capacity of 60 mAh/g (Fig 5.14). Compared to uncoated PbSO₄ (Fig. 5.5, Section 5.3.2.2) which produced only 40 mAh/g at C rates higher than 0.2 C, this shows the carbon coating caused a vast improvement in the C-rate capability.

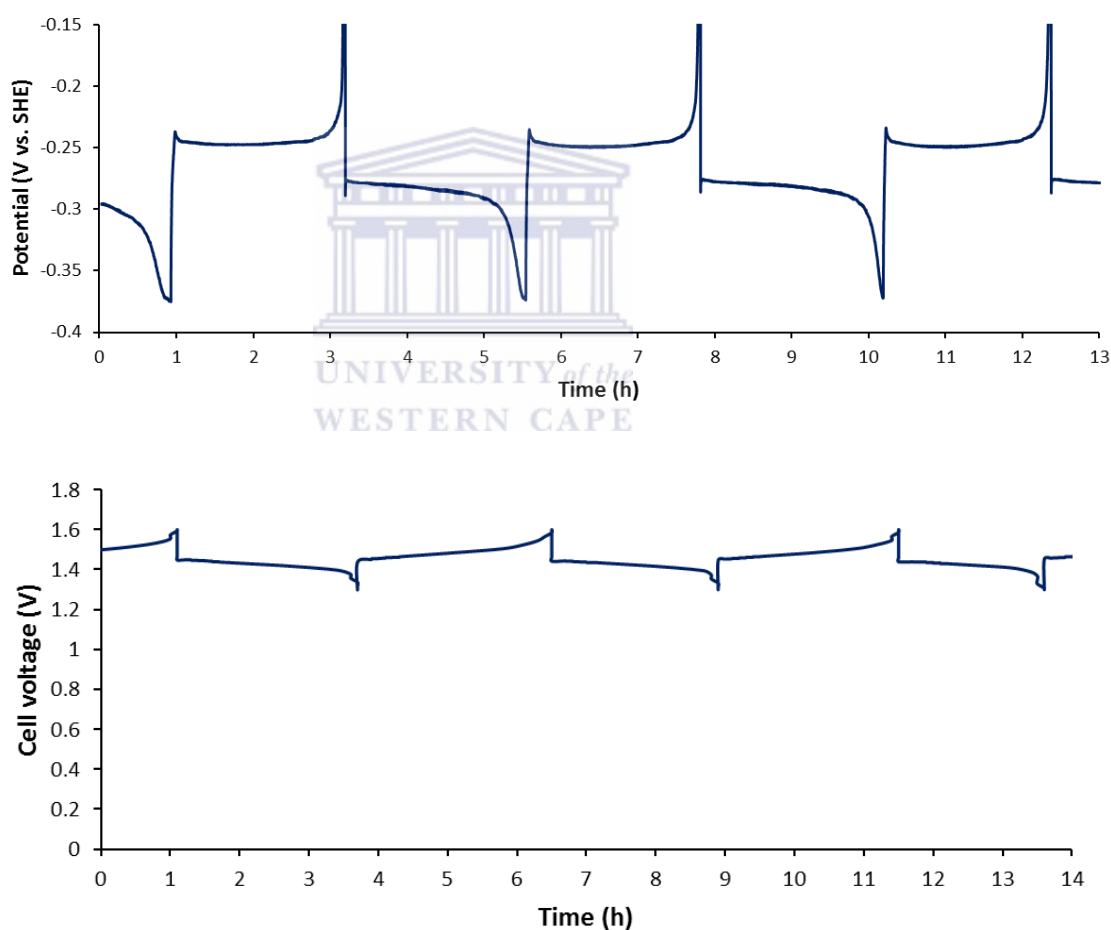


Fig 5.13 Galvanic cycling of ccPbSO₄ at 0.4 C showing stable charge/discharge. Lower plot shows PbSO₄/LMO cell voltage.

The cycling plot of the ccPbSO₄ electrode (Fig 5.13) also shows no appearance of the secondary charge plateau below -0.35 V vs. SHE observed previously with uncoated PbSO₄ (Fig 5.7). This is most likely because (1) the high C rate caused greater electrode polarization which effectively pushes the secondary plateau to a lower voltage and (2) a larger capacity was accessible from the PbSO₄ prior to reaching the plateau, possibly due to the improved conductivity gained through the carbon coating.

Fig 5.14 shows continued cycling of the above cell at 0.4 C for 200 cycles (~40 days). The cell cycled with high coulombic efficiency at ~95% and only lost <5% of its initial capacity, with an average 60 mAh/g specific capacity for ccPbSO₄. The specific energy of the cell's total active material was ~47 Wh/kg. This was slightly lower than the previous uncoated PbSO₄/LMO cell at ~53 Wh/kg, but the vastly improved capacity retention and higher C rate capability of ccPbSO₄ are clearly advantageous features.

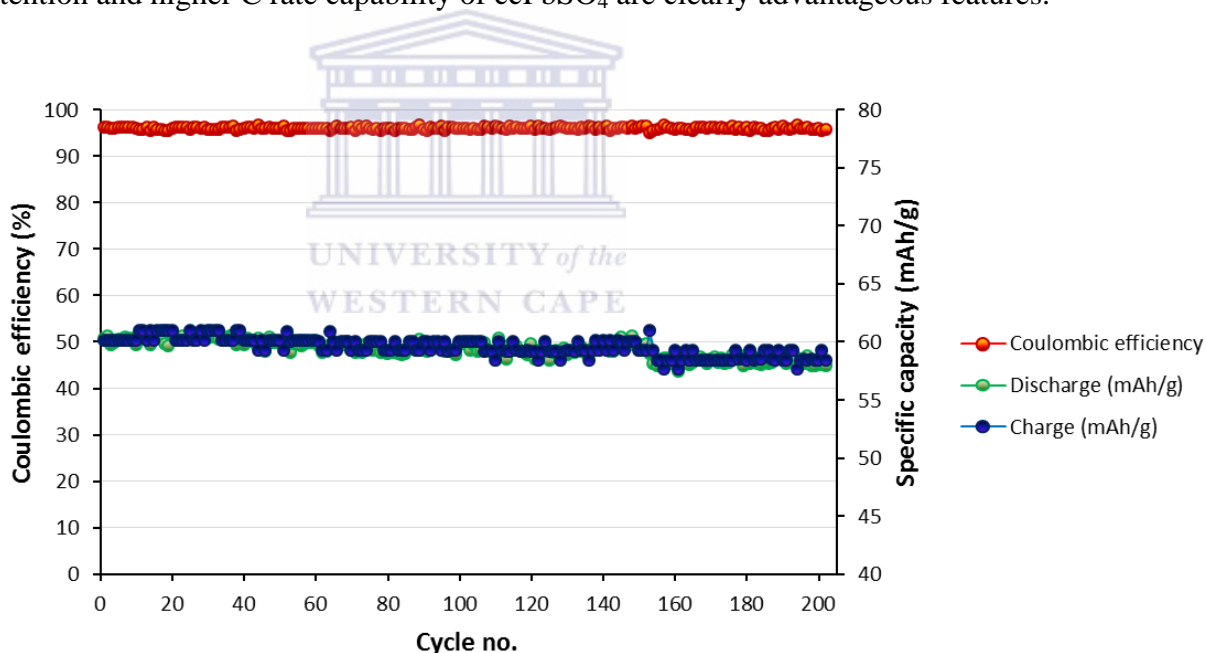


Fig 5.14 40-day galvanic cycling of ccPbSO₄ at 0.4 C showing stable charge/discharge at 95% coulombic efficiency, <5% loss of capacity. Specific capacity of PbSO₄ (right 'y' axis) and coulombic efficiency (left 'y' axis).

Fig 5.15 shows the cycle plot for the ccPbSO₄/LMO cell at 0.2 C for 100 cycles. The average discharge capacity of ccPbSO₄ stabilized at ~76 mAh/g at a coulombic efficiency of 93% after <5% loss in capacity. The specific energy of the combined active materials was 59.1 Wh/kg at 0.2 C, nearly 6 Wh/kg higher than the uncoated PbSO₄/LMO cell. Therefore, if a practical cell could be made at 65% of this value it would have a specific energy of 38.4 Wh/kg, which is 15 Wh/kg higher than the Aquion® cell at 23 Wh/kg but lower than Pb-acid batteries at ~25-50 Wh/kg.

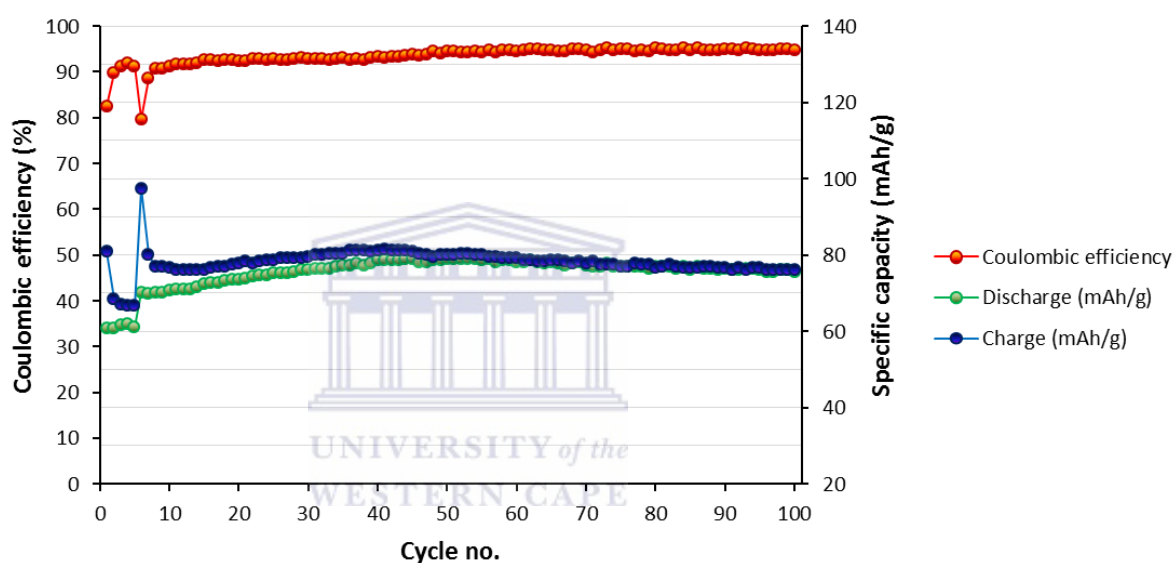


Fig 5.15 40-day galvanic cycling of ccPbSO₄ at 0.2 C showing stable charge/discharge at 93% coulombic efficiency, <5% loss of capacity. Specific capacity of PbSO₄ (right 'y' axis) and coulombic efficiency (left 'y' axis).

At the time of writing, the above cells were still cycling and therefore were not interrupted for SEM analysis of the ccPbSO₄ electrode surface. However, after 100 cycles the electrodes did not visually appear to have the same grey surface film as previously seen on uncoated PbSO₄ electrodes, which suggests along with the more stable cycling profile, that carbon coating had inhibited the crystal growth possibly through containment of the PbSO₄ microparticle morphology.

5.4.2.2 24-h self-discharge of ccPbSO₄/LMO and energy efficiency

To examine the rate of self-discharge in ccPbSO₄/LMO cells, a 24-h rest period at full charge was included into the cycling program. Fig 5.16 shows that at the beginning of the full charge holding period the voltage rises abruptly by ~0.025 V to the charge holding plateau. No significant drop in cell voltage or loss of charge occurred over the holding period, which amounted to <5 % capacity loss, which is comparable to both AC/LMO [4] and Pb-acid cells [63]. Importantly, this result shows that the Pb metal particles are sufficiently stable at pH 7 over 24 h to retain an efficient quantity of charge. Overall the difference in charge and discharge voltage is ~0.05 V, which coupled to ~90-95% coulombic efficiency and ~0.025 V voltage difference on LMO between charge/discharge provides an energy storage efficiency between 75-80%. This figure is not as high as the 90% efficiency achievable in Li-ion batteries, but it is comparable to Pb-acid batteries between 60-85% [2, 64].

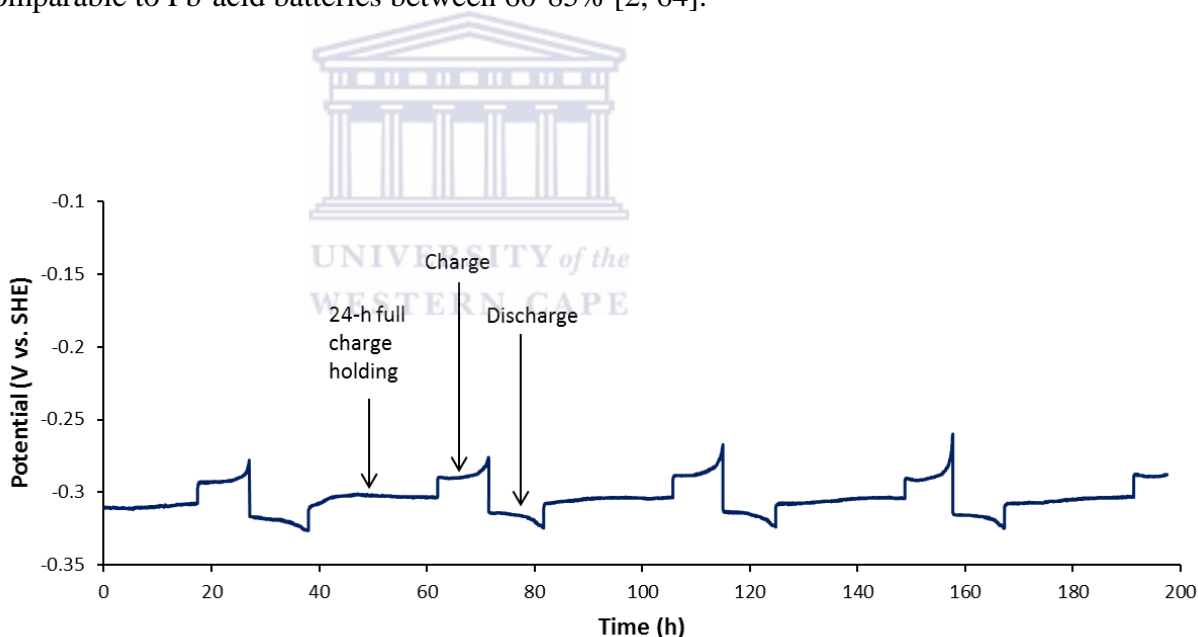


Fig 5.16 24-h full charge holding period of a ccPbSO₄/LMO cell cycled at 0.1 C showing insignificant loss of charge or voltage resulted from the holding period.

5.4.3 Conclusions

ccPbSO₄ was successfully synthesized using a low cost (sucrose-source) carbon coating method. Compared to uncoated PbSO₄, ccPbSO₄ proved to have far greater cycling

stability and produced a 10 mAh/g higher obtainable specific capacity than uncoated PbSO₄ when cycled at the same 0.2 C rate. The moderately high energy efficiency between 75 – 80% with a 24 h charge holding period with <5% capacity loss is comparable with other battery technologies. Overall, carbon coating proved an efficient and low cost solution to obtaining both higher stability and capacity from PbSO₄ microparticles.

5.5 PbSO₄-doped activated carbon (AC)

5.5.1 Introduction

Prior to the work presented work in Section 5.1 – 5.4, various trial experiments were carried out that led to the eventual use of PbSO₄ microparticles. These included a series of tests that examined Pb metal, PbO and even PbO₂, as potential starting material for Pb anode formation through charging. Both Pb metal sheet and Pb metal powder in thin film electrode format provided the same working voltage as was eventually found for PbSO₄ microparticles. Both could be successfully charged and discharged but only produced ~20 mAh/g specific capacity and required a < 0.1 C rate to fully access the capacity. PbO and PbO₂ powder were also incorporated into electrode films containing carbon black and PTFE, but both, particularly PbO₂, required Pb formation charging periods that exceeded the required capacity of LMO, which was clearly impractical as a means of Pb electrode formation. At this stage, commercially bought PbSO₄ was also tested as an electrode film but again produced very low capacity below 20 mAh/g. However, what led to the use of precipitated PbSO₄ microparticles in the present study was an initial experiment where PbSO₄ was doped into activated carbon (AC) via its *in situ* precipitation of microparticles into an AC film electrode. The details of the experiment and the effect of doped-PbSO₄ on AC specific capacity in an AC/LMO cell are presented below.

5.5.2 Experimental

5.5.2.1 *In situ preparation and cycling of a PbSO₄-doped AC electrode*

In order to determine if PbSO₄ doping could increase the specific capacity of AC, a 10 mg AC film electrode was first cycled at ~6 C as part of an AC/LMO cell of 1:1 mass ratio (~1:2 capacity ratio). After a set number of complete cycles the cycling program was stopped and the AC electrode removed. The electrode was then washed in distilled water and immersed into a saturated solution of Pb(NO₃)₂ for 1 h. The electrode was then removed from the solution and briefly blotted on paper towel to remove excess/non-absorbed Pb(NO₃)₂ and then immersed in saturated Na₂SO₄ for 1 h to precipitate PbSO₄ within the interstitial pores of electrode. Lastly, the electrode was again blotted on paper towel and rinsed in 1 M Li₂SO₄ electrolyte to remove residual unreacted Na₂SO₄. The electrode was then returned to the cell and cycling resumed.

5.5.3 Results and discussion

Fig 5.17 shows the cycling of an AC/LMO cell at 6 C that was interrupted after 10 cycles and its AC electrode doped with PbSO₄ and then returned to cell to resume cycling. The doping resulted in a doubling of the cell capacity which was a clear indication that precipitated PbSO₄ had significant capacity even at the resultant high 3 C rate of the hybrid cell. This result prompted the use of precipitated PbSO₄ in the previous Sections of this Chapter. However, the result in itself is also significant and suggests that AC-PbSO₄ doping can provide a means to increase the limited capacity of AC. This provides an interesting topic for further research and also raises the question of what effects doping the AC electrode at different states of charge might have on capacity and electrode performance. Furthermore, it will also be of interest to determine to what extent Pb²⁺ ions absorb into the electrode material, i.e. whether this occurs in the pores of the AC or just within the interstitial spaces between the particles. Finally, the concept of doping AC with Pb, is analogous to so-called Pb-C (“Lead carbon”) cells such as the Ultrabattery®, which constitute higher powered Pb-acid cells by having an AC electrode in parallel with a negative Pb electrode as a combined anode against a

PbO₂ cathode [65]. The use of this system in the above form with an LMO cathode in pH 7 electrolyte is thus another novel area of research that awaits further investigation.

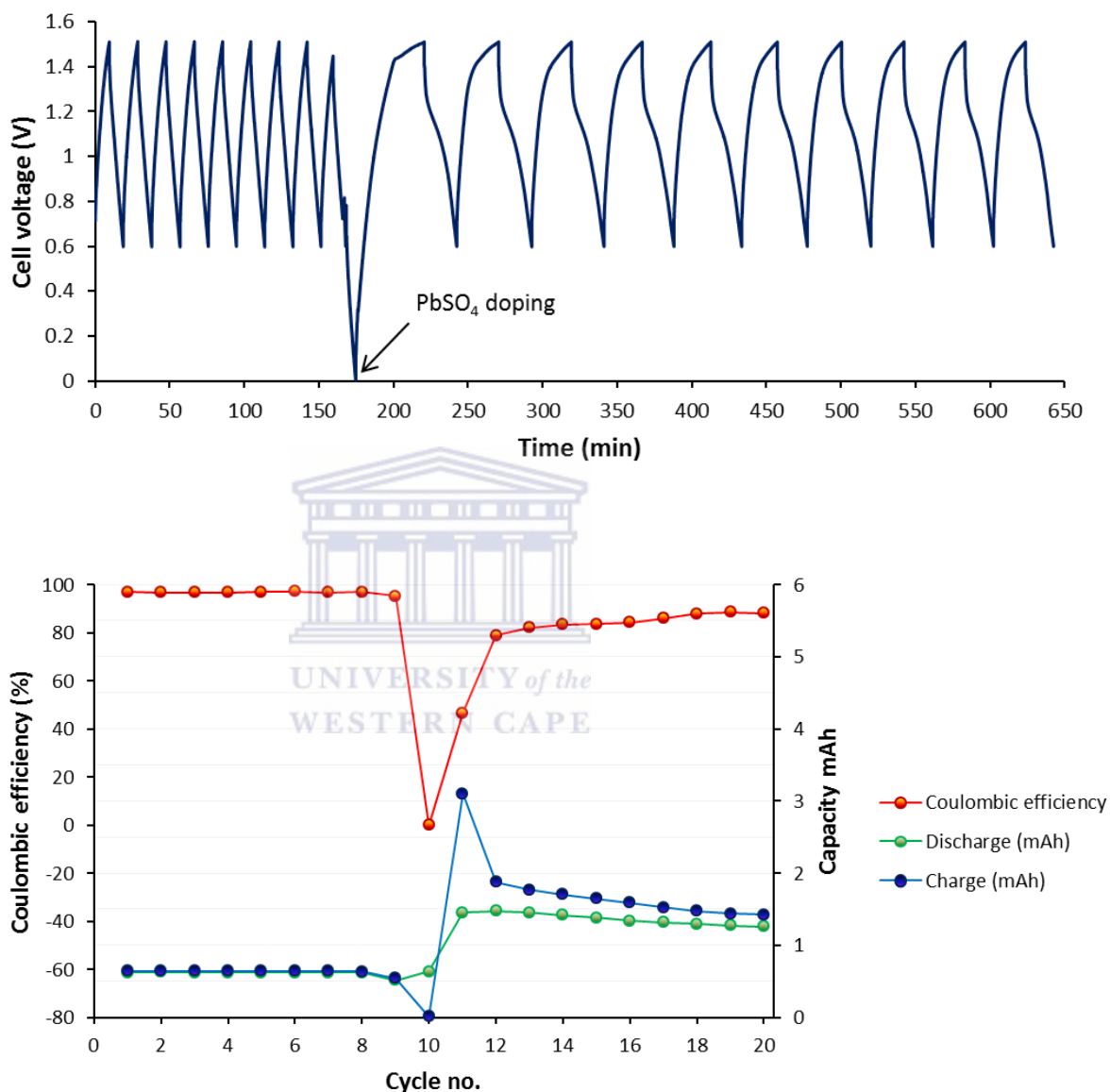


Fig 5.17 PbSO₄ *in situ* doping of AC in an AC/LMO cell. The cell was interrupted at the tenth cycle cell where the AC electrode was removed, doped, returned to the cell and cycling resumed. The cell capacity ('y' axis) was approximately doubled by the doping.

5.6 Predictions on cost/kWh and Pb usage

5.6.1 Cost/kWh of a PbSO₄/LMO practical cell

The figure of 59.1 Wh/kg active material specific energy obtained in the above study, at 65% for a practical cell would be 38.4 Wh/kg. This value is 84.4% of 45.5 Wh/kg: the theoretical 65% practical target value of a PbSO₄/LMO cell calculated in Section 2.6.3. Table 5.1 shows the cost/kWh calculations and percentage mass contributions of the cell developed in this study, which used a 1:0.8 PbSO₄/LMO mass ratio, assuming a 65% practical cell specific energy.

Material	Cost/kg	Cell mass (mg)	Mass %	\$/1kg cell	% cost	38.4 Wh/kg P/E 1:5 (\$/kWh)
LMO	10	295	36.1	3.61	64.8	93.96
PbSO ₄	2	236.1	28.9	0.58	10.4	15.06
Carbon black	5	62.5	7.6	0.38		
PTFE	5	30.9	3.8	0.19		
Li ₂ SO ₄	5	62.5 (aq)	7.6 (aq)			
		6.3 (s)	0.8 (s)	0.04		
Stainless steel	5	120	14.7	0.76		
Separator (cotton)	1	10	1.2	0.01		
Totals		817	100	5.57	100	145.05

Table 5.1 Cost/kWh prediction for a 65% active material mass PbSO₄/LMO cell at P/E 1:5 (i.e. at maximum specific energy)

$$0.773x = 0.65(130 + x) \quad (7)$$

Where 0.773 is the fraction of active materials in electrode film (Table 2.5(b)), 'x' is the total mass of electrode film, and 130 mg is the combined mass of two current collectors and one separator.

$$x = 687 \text{ mg electrode material}$$

$$0.773 x = 531.1 \text{ mg PbSO}_4 + \text{LMO}$$

Electrode film	Mass (mg)	Mass (%)
Active material	85	77.3
Carbon black	10	9.1
PTFE	5	4.5
Electrolyte	10	9.1
Total	110	100

Table 2.5(b) electrode mass contributions (from Section 2.5.2)

The calculated value of cost/kWh, assuming a practical cell of 38.4 Wh/kg, comes to \$145/kWh. The price is substantially lower than AC/LMO (>\$250/kWh) and on par with Pb-acid at \$150/kWh. In terms of Pb mass percentage the above cell is 19.7% Pb as opposed 60% in Pb acid batteries. This equates to using $2.3 \times$ less Pb/kWh and therefore represents a significant reduction in Pb usage for the same cost as Pb-acid/kWh. Lastly, in terms of material costs it should be noted that the cost of cell packaging, tabs, and the cost of sugar for carbon coating have not been included in the above calculations.



5.7 Conclusions

The work presented in this chapter both conceived and developed a novel cell chemistry. The PbSO₄/LMO cell uses aqueous pH 7 1 M Li₂SO₄ electrolyte, and forms an electrode coupling where PbSO₄ charge/discharge is analogous to that in Pb-acid batteries regarding its standard potential, and the LMO cathode intercalates/de-intercalates Li⁺ as in Li-ion batteries and ARLBs. The average discharge voltage of the cell is 1.4 V and forms a flat charge/discharge plateau. The use of a low cost carbon coating method to encapsulate PbSO₄ microparticles had a marked improvement on cell performance, and compared to uncoated PbSO₄ improved both rate capability and specific capacity of the material. The active materials of the ccPbSO₄/LMO cell produced a specific energy 51.1 Wh/kg, which, if a 65% yield is possible for a practical cell format, equals 38.4 Wh/kg, which is 15 Wh/kg higher than the Aquion® cell at 23 Wh/kg but lower than Pb-acid batteries at ~25-50 Wh/kg (reviewed in Chapter 2). Here, it of interest that the 100 mAh/g target specific capacity value for PbSO₄ as reached in Pb-acid cells fell short in being only 76 mAh/g. However, further

investigations to improve the conductivity of the material may be able to increase this figure. The cost of the cell, if a 65% value of the active material specific energy for a practical cell can be realized, is on par with Pb-acid battery technology and, importantly, uses $2.3 \times$ less Pb/kWh. The cycling stability achieved thus far is promising, but will require testing over comparable cycle life periods to commercial batteries, which could be anywhere between 5 – 15 years.



Chapter 6

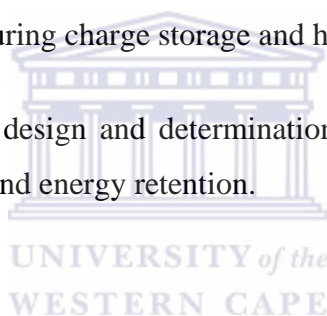
Conclusions & Future work

6.1 Conclusions on high power AC/LMO cells

The viability of AC/LMO cells to provide high specific power in practical cell format was investigated. A specific power to energy ratio of 50:1 (P/E) at 400 W/kg: 8 Wh/kg for a practical AC/LMO cell (i.e. considering total cell component mass contributions) had been previously proposed possible but not tested by Wang et al. [6]. This predicted P/E ratio, if obtainable, would be appropriate for high power battery functions in HFCV (hybrid fuel cell vehicles) [8]. To establish the above proof of concept required testing the power performance of thick electrode films. The study found that the above target figures could be reached with a 50 mg/cm^2 loading of active material using a charging voltage of 2.2 V and a active material mass ratio of 2:1 (anode vs. cathode). The requirement of high charging voltage related to the low specific capacity ($\sim 40 \text{ mAh/g}$) of the activated carbon (AC) anode. This was achieved by charging AC close to the onset of hydrogen evolution at high current density. The electrode material thickness was found to be directly proportional to the size of voltage drop on charge to discharge transition. Up-scaling of the cell format to a theoretical 3 Ah cell was also carried out. However, due to a suspected increased resistance of the multiple electrode contact points, the cell's tested capacity during high power cycling was less than 50% of the expected value. The issue of correct cell design for larger scale cells was concluded an important point for consideration in practical cell usage. A key technical achievement of the study was the development of an "electrode thickness test cell" system, which can on the basis of the results be concluded as an important tool for understanding the "real" or practical capabilities of battery materials. Overall the study concludes that the AC/LMO cell holds considerable promise for high specific power applications but requires the following further investigations (see below).

6.2 Future work on high power AC/LMO cells

- Reducing voltage drop of thick LMO films at high current density power remains an important objective to improve the energy efficiency of the cell at high power. Nano-particulate forms of LMO, and carbon coating techniques could be investigated to lower the resistance of the required thick-film electrodes.
- Lowering the mass contribution of current collectors through development of light-weight, thin, corrosion-resistant foils and meshes, and investigation of electrically conducting and corrosion resistant coatings such as SnO_2 , to further increase specific power and energy
- Long-term testing of AC/LMO cells to determine the effects of cathode current collector corrosion during charge storage and high power operation.
- Optimisation of cell design and determination of maximum cell capacity size for high specific power and energy retention.



6.3 Conclusions on PbSO_4 /LMO cells

To establish an affordable, high capacity, aqueous cell for large-scale bulk storage applications, a novel cell chemistry, PbSO_4 /LMO, was both conceived and tested. Firstly, the charge/discharge behaviour of the PbSO_4 anode material in pH 7 Li_2SO_4 (aq) electrolyte was shown to occur at the same voltage as in Pb-acid cells. Carbon coating of the PbSO_4 particles, to form cc PbSO_4 , notably improved their cycle stability beyond 100 cycles, and raised their specific capacity by more than 10%. The active materials of the cc PbSO_4 /LMO cell produced a specific energy 51.1 Wh/kg. Therefore, if a 65% yield could be achieved for a practical cell format (to be tested in future studies), this equals 38.4 Wh/kg, which is 15 Wh/kg higher than the Aquion® cell at 23 Wh/kg [4] (a current commercial contender for large-scale energy storage). The cost of the cell at the 65% yield value, is on par with Pb-acid battery technology and, importantly, uses $2.3 \times$ less Pb/kWh. The cycling stability achieved thus far is promising, but will require

testing over comparable cycle life periods to commercial batteries, which could be anywhere between 5 – 15 years.

6.4 Future work on PbSO₄/LMO cells

- Continued long-term galvanic cycling of ccPbSO₄ to establish the life-span of the cell chemistry.
- Construction and testing of thick-film ccPbSO₄ electrodes at 65% active material mass contribution to establish cell performance of the material in practical cell format.
- Determination of capacity difference in of PbSO₄ in H₂SO₄ and Li₂SO₄ (aq) electrolyte to further understand the electrode dynamics of the material at pH 7.
- PbSO₄ nanoparticle particle preparation and encapsulation to improve particle conductive and increase power performance.
- Testing of commercial negative Pb-electrode material used in Pb-acid cells against LMO electrodes, to establish compatibility with existing electrode manufacturing technology.
- Testing of PbSO₄ anodes in Na₂SO₄ electrolyte to further lower total cell costs.

References

1. David, H., *EV Everywhere grand challenge: Battery status and cost reduction prospects*. US DOE ppt presentation July 26. By Hybrid & Electric Systems Vehicle Technologies Program 2012.
2. Yang, Z., et al., *Electrochemical Energy Storage for Green Grid*. Chemical Reviews, 2011. **111**(5): p. 3577-3613.
3. Manjunatha, H., G. Suresh, and T. Venkatesha, *Electrode materials for aqueous rechargeable lithium batteries*. Journal of Solid State Electrochemistry, 2011. **15**(3): p. 431-445.
4. Whitacre, J., et al., *An aqueous electrolyte, sodium ion functional, large format energy storage device for stationary applications*. Journal of Power Sources, 2012. **213**: p. 255-264.
5. Wang, Y., J. Yi, and Y. Xia, *Recent Progress in Aqueous Lithium-Ion Batteries*. Advanced Energy Materials, 2012. **2**(7): p. 830-840.
6. Wang, Y.-g. and Y.-y. Xia, *A new concept hybrid electrochemical supercapacitor: Carbon/LiMn₂O₄ aqueous system*. Electrochemistry Communications, 2005. **7**(11): p. 1138-1142.
7. Wu, Y., et al., *Aqueous rechargeable lithium batteries as an energy storage system of superfast charging like filling gasoline*. Energy Environ. Sci., 2013.
8. Markel, T., et al. *Energy storage system requirements for hybrid fuel cell vehicles*. in *Advanced Automotive Battery Conference, Nice, France, June*. 2003.
9. Zheng, H., et al., *A comprehensive understanding of electrode thickness effects on the electrochemical performances of Li-ion battery cathodes*. Electrochimica Acta, 2012. **71**: p. 258-265.
10. Luo, J.-Y., et al., *Raising the cycling stability of aqueous lithium-ion batteries by eliminating oxygen in the electrolyte*. Nature Chemistry, 2010. **2**(9): p. 760-765.
11. Li, W., J.R. Dahn, and D.S. Wainwright, *Rechargeable Lithium Batteries with Aqueous Electrolytes*. Science, 1994. **264**(5162): p. 1115-1118.
12. Whittingham, M.S., *Lithium batteries and cathode materials*. Chemical Reviews, 2004. **104**(10): p. 4271-4302.
13. Abraham, K., *LITHIUM-AIR AND OTHER BATTERIES BEYOND LITHIUM-ION BATTERIES*. Lithium Batteries: Advanced Technologies and Applications, 2013. **58**: p. 161.
14. Jossen, A., *State of the Art and Perspectives of Progress in Photovoltaic Solar Energy Production of Hydrogen Energy Storage*. Final year report: Zentrum für Sonnenenergie- und Wasserstoff-Forschung Baden-Württemberg (ZSW), 2008.
15. Köhler, U., C. Antonius, and P. Bäuerlein, *Advances in alkaline batteries*. Journal of Power Sources, 2004. **127**(1): p. 45-52.
16. Ikuo Yonezu, *High Performance Nickel-Metal Hydride Battery Technologies for HEV*. AABC Las Vegas, Feb. 4-7 2002, 2002.
17. Bank, D., *Electric Cars: Plugged In; Batteries must be included*. FITT Research, 2008. **9**.
18. Banerjee, A., et al., *A 12 V Substrate-Integrated PbO₂-Activated Carbon Asymmetric Hybrid Ultracapacitor with Silica-Gel-Based Inorganic-Polymer Electrolyte*. ECS Transactions, 2012. **41**(13): p. 101-113.

19. Thackeray, M., et al., *Electrochemical extraction of lithium from LiMn_2O_4* . Materials Research Bulletin, 1984. **19**(2): p. 179-187.
20. Xia, Y., et al., *Correlating Capacity Fading and Structural Changes in $\text{Li}_{1+y}\text{Mn}_{2-y}\text{O}_{4-\delta}$ Spinel Cathode Materials: A Systematic Study on the Effects of Li/Mn Ratio and Oxygen Deficiency*. Journal of The Electrochemical Society, 2001. **148**(7): p. A723-A729.
21. Du Pasquier, A., et al., *Mechanism for Limited 55° C Storage Performance of $\text{Li}_{1.05}\text{Mn}_{1.95}\text{O}_4$ Electrodes*. Journal of The Electrochemical Society, 1999. **146**(2): p. 428-436.
22. Tang, W., et al., *LiMn_2O_4 nanorods as a super-fast cathode material for aqueous rechargeable lithium batteries*. Electrochemistry Communications, 2011. **13**(11): p. 1159-1162.
23. Tang, W., et al., *Nanochain LiMn_2O_4 as ultra-fast cathode material for aqueous rechargeable lithium batteries*. Electrochemistry Communications, 2011. **13**(2): p. 205-208.
24. Eftekhari, A., *Electrochemical behavior of thin-film LiMn_2O_4 electrode in aqueous media*. Electrochimica Acta, 2001. **47**(3): p. 495-499.
25. Zhang, H., X. Yu, and P.V. Braun, *Three-dimensional bicontinuous ultrafast-charge and-discharge bulk battery electrodes*. Nature Nanotechnology, 2011. **6**(5): p. 277-281.
26. Qu, Q., et al., *Porous LiMn_2O_4 as cathode material with high power and excellent cycling for aqueous rechargeable lithium batteries*. Energy Environ. Sci., 2011. **4**(10): p. 3985-3990.
27. Tang, W., et al., *An aqueous rechargeable lithium battery of excellent rate capability based on a nanocomposite of MoO_3 coated with PPy and LiMn_2O_4* . Energy & Environmental Science, 2012. **5**(5): p. 6909-6913.
28. Tang, W., et al., *A hybrid of V_2O_5 nanowires and MWCNTs coated with polypyrrole as an anode material for aqueous rechargeable lithium batteries with excellent cycling performance*. Journal of Materials Chemistry, 2012. **22**(38): p. 20143-20145.
29. Köhler, J., et al., *LiV_3O_8 : characterization as anode material for an aqueous rechargeable Li-ion battery system*. Electrochimica Acta, 2000. **46**(1): p. 59-65.
30. Wang, G., et al., *Characteristics of an aqueous rechargeable lithium battery (ARLB)*. Electrochimica Acta, 2007. **52**(15): p. 4911-4915.
31. Wang, H., et al., *Electrochemical properties of TiP_2O_7 and $\text{LiTi}_2(\text{PO}_4)_3$ as anode material for lithium ion battery with aqueous solution electrolyte*. Electrochimica Acta, 2007. **52**(9): p. 3280-3285.
32. Wang, G., et al., *An aqueous rechargeable lithium battery based on LiV_3O_8 and $\text{Li}[\text{Ni}_{1/3}\text{Co}_{1/3}\text{Mn}_{1/3}]\text{O}_2$* . Journal of Applied Electrochemistry, 2008. **38**(4): p. 579-581.
33. Liu, X.-H., et al., *Electrochemical properties of rechargeable aqueous lithium ion batteries with an olivine-type cathode and a Nasicon-type anode*. Journal of Power Sources, 2009. **189**(1): p. 706-710.
34. Levi, M., et al., *Ultrafast anode for high voltage aqueous Li-ion batteries*. Journal of Solid State Electrochemistry, 2012. **16**(11): p. 3443-3448.

35. Luo, J.Y. and Y.Y. Xia, *Aqueous Lithium-ion Battery LiTi₂ (PO₄)₃/LiMn₂O₄ with High Power and Energy Densities as well as Superior Cycling Stability***. *Advanced Functional Materials*, 2007. **17**(18): p. 3877-3884.
36. Li, W. and J. Dahn, *Lithium-Ion Cells with Aqueous Electrolytes*. *Journal of The Electrochemical Society*, 1995. **142**(6): p. 1742-1746.
37. Wessells, C., R.A. Huggins, and Y. Cui, *Recent results on aqueous electrolyte cells*. *Journal of Power Sources*, 2011. **196**(5): p. 2884-2888.
38. Yan, J., et al., *Rechargeable hybrid aqueous batteries*. *Journal of Power Sources*, 2012. **216**: p. 222-226.
39. Shu, Q., et al., *Proton-Induced Dysfunction Mechanism of Cathodes in an Aqueous Lithium Ion Battery*. *The Journal of Physical Chemistry C*, 2013. **117**(14): p. 6929-6932.
40. El-Sherbini, E.F. and S.S. Abd El Rehim, *Electrochemical behaviour of lead electrode in Na₂SO₄ solutions*. *Materials Chemistry and Physics*, 2004. **88**(1): p. 17-22.
41. Zhang, X.G., *Corrosion and electrochemistry of zinc* 1996: Springer.
42. Férey, G., et al., *Mixed-Valence Li/Fe-Based Metal–Organic Frameworks with Both Reversible Redox and Sorption Properties*. *Angewandte Chemie International Edition*, 2007. **46**(18): p. 3259-3263.
43. Shao, J., et al., *Core-shell sulfur@polypyrrole composites as high-capacity materials for aqueous rechargeable batteries*. *Nanoscale*, 2013. **5**(4): p. 1460-1464.
44. Chan, C., et al., *Current status and future trends of energy storage system for electric vehicles*. *Journal of Asian Electric Vehicles*, 2007. **5**(2): p. 1055-1060.
45. Yonggao, W., *Study of high specific energy electrochemical cells*. PhD thesis Fudan University 2007.
46. Dickinson, E., P. Westreich, and M.R. Romeo. *Axion PbC Batteries: A Lead-Carbon Asymmetric Solution to the Charge Acceptance Limitation of Lead-Acid Batteries*. in *Meeting Abstracts*. 2011. The Electrochemical Society.
47. Symposium, T.F.U.G.A.E., *JM Energy's Lithium Ion Capacitor: The Hybrid Energy Storage Advantage*. www.avsusergroups.org/tfug_pdfs/2009_2banas.pdf, 2009.
48. Omar, N., et al., *SuperLib Project: Advanced Dual-Cell Battery Concept for Battery Electric Vehicles*.
49. Qu, Q., et al., *A new cheap asymmetric aqueous supercapacitor: Activated carbon//NaMnO₂*. *Journal of Power Sources*, 2009. **194**(2): p. 1222-1225.
50. Tevar, A. and J. Whitacre, *Relating Synthesis Conditions and Electrochemical Performance for the Sodium Intercalation Compound Na₄Mn₉O₁₈ in Aqueous Electrolyte*. *Journal of The Electrochemical Society*, 2010. **157**(7): p. A870-A875.
51. Karden, E., et al., *Energy storage devices for future hybrid electric vehicles*. *Journal of Power Sources*, 2007. **168**(1): p. 2-11.
52. Visscher, W., *Cyclic voltammetry on lead electrodes in sulphuric acid solution*. *Journal of Power Sources*, 1977. **1**(3): p. 257-266.
53. Pavlov, D., *Lead-Acid Batteries: Science and Technology: Science and Technology* 2011: Elsevier.

54. Hutzenlaub, T., et al., *FIB/SEM-based calculation of tortuosity in a porous LiCoO₂ cathode for a Li-ion battery*. *Electrochemistry Communications*, 2013. **27**(0): p. 77-80.
55. Hess, K.C., J.F. Whitacre, and S. Litster, *In situ measurements of potential, current and charging current across an EDL capacitance anode for an aqueous sodium hybrid battery*. *Journal of The Electrochemical Society*, 2012. **159**(8): p. A1351-A1359.
56. Barboux, P., F.K. Shokoohi, and J.-M. Tarascon, *Method for preparation of LiMn. sub. 2 O. sub. 4 intercalation compounds and use thereof in secondary lithium batteries*, 1992, Google Patents.
57. Béguin, F., et al., *Effect of various porous nanotextures on the reversible electrochemical sorption of hydrogen in activated carbons*. *Electrochimica Acta*, 2006. **51**(11): p. 2161-2167.
58. Garche, J., *Advanced battery systems—the end of the lead–acid battery?* *Physical Chemistry Chemical Physics*, 2001. **3**(3): p. 356-367.
59. Bullock, K.R., *The electromotive force of the lead–acid cell and its half-cell potentials*. *Journal of Power Sources*, 1991. **35**(3): p. 197-223.
60. Pavlov, D., G. Petkova, and T. Rogachev, *Influence of H_2 SO₄ concentration on the performance of lead-acid battery negative plates*. *Journal of Power Sources*, 2008. **175**(1): p. 586-594.
61. Caballero, A., et al., *Thin electrodes based on rolled Pb–Sn–Ca grids for VRLA batteries*. *Journal of Power Sources*, 2004. **125**(2): p. 246-255.
62. Gagnon, E.G. and D.J. Lisi, *Method of preparing electrodes for lead-acid electrode battery*, 1996, Google Patents.
63. Bullock, K.R., *Lead Acid Battery Systems and Technology for Sustainable Energy*, in *Batteries for Sustainability* 2013, Springer. p. 117-134.
64. Dunn, B., H. Kamath, and J.-M. Tarascon, *Electrical energy storage for the grid: A battery of choices*. *Science*, 2011. **334**(6058): p. 928-935.
65. Cooper, A., et al., *The UltraBattery—A new battery design for a new beginning in hybrid electric vehicle energy storage*. *Journal of Power Sources*, 2009. **188**(2): p. 642-649.